Numerical Engineering of Adiabatic Quantum Operations

by

Seyed Sahand Tabatabaei

A thesis
presented to the University of Waterloo
in fulfillment of the
thesis requirement for the degree of
Master of Science
in
Physics

Waterloo, Ontario, Canada, 2020

Author's Declaration

I hereby declare that I am the sole author of this thesis. This is a true copy of the thesis, including any required final revisions, as accepted by my examiners.

I understand that my thesis may be made electronically available to the public.

Abstract

Adiabatic quantum operations are ubiquitous in fields such as quantum information processing, quantum control, and magnetic resonance, where their high fidelity and general robustness renders them an essential tool for various applications. This inherent robustness due to adiabaticity can, however, be impaired in cases where the experimental conditions strictly require very fast evolution times. In this thesis, we provide a gradient-based numerical optimization protocol for efficiently engineering adiabatic operations, allowing for the systematic inclusion of robustness criteria against various experimental non-idealities, including inhomogeneities and uncertainties in system parameters, as well as perturbations in the Hamiltonian such as spin-spin interactions.

The protocol is implemented in the context of adiabatic passages for magnetic resonance, and it is shown that in addition to conventional adiabatic pulses, it can also generate exceptionally fast operations that although slightly deviate from adiabaticity in limited instances, still lead to a high fidelity. The effectiveness of our method for addressing perturbations is also demonstrated by designing a fast adiabatic passage for dipolar-coupled electrons, and numerically comparing its performance with a pulse without such considerations.

Acknowledgements

First and foremost, I would like to express my deep appreciation to my supervisor Professor Raffi Budakian, whose guidance and invaluable insights have made this project possible. I would not have learned so much if it was not for his enthusiasm and continuous willingness to devote his time to his students.

The last two years in the Budakian group have truly been some of the most intellectually stimulating times of my life. This would not have been the case if it was not for my brilliant colleagues (and friends) Andrew Jordan, Pardis Sahafi, Ben Yager, Michèle Piscitelli, Bill Rose and Holger Haas. I would like to particularly thank Bill Rose for our fruitful discussions and Holger Haas, for being my collaborator on this project.

I would also like to greatly thank my parents, especially for lighting my interest in science and teaching me about its value from an early age.

Last but not least, I am eternally grateful to my wonderful fiance and best friend Bita. This would not have been possible without her ever-lasting support, patience, and encouragement.

Table of Contents

List of Figures

Chapter 1

Introduction and Background

The concept of adiabatic quantum evolution dates back to Born and Fock [1] at the very early stages of quantum theory, with further development by Kato [2] and Berry [3]. The main question addressed throughout this development was simply "how does a quantum system evolve under an infinitely slow excitation?". It was established that in this limit, eigenstates of the initial system Hamiltonian stay instantaneous eigenstates throughout the evolution. Over time, this simple concept has brought about a plethora of applications in various parts of physics, chemistry, and quantum information science.

One notable application can be found in magnetic resonance [4, 5], where adiabatic operations have become a well-established method for robust, high fidelity manipulation and control of both nuclear and electronic spins, such that they are now important tools in nuclear magnetic resonance (NMR) spectroscopy, magnetic resonance imaging (MRI) and NMR quantum information processing. Adiabatic operations have also found their way into ion traps [6, 7], superconducting circuits [8, 9] and experimental atomic and molecular physics in general [10, 11].

Another, more recent development, has been the field of adiabatic quantum computation (AQC) [12, 13], where the system is initialized in a specific eigenstate of the Hamiltonian (usually the ground state), and then the Hamiltonian is slowly evolved into a more complicated one, the ground state of which contains the solution to the computational problem at hand. It has been shown that AQC is universal, and mathematically equivalent to the standard circuit model of quantum computing, in the sense that one can simulate the other in polynomial overhead time [14]. Various quantum algorithms, such as factorization [15] and quantum optimization algorithms [16], have been experimentally implemented with AQC.

In this work, we present a novel numerical method for engineering fast adiabatic operations on two-level systems, utilizing a gradient-based optimization algorithm. The method allows for the explicit inclusion of various robustness criteria against different perturbations, such as spin-spin interactions, as it naturally fits into the Van Loan auxiliary matrix formalism developed in [17] to perturbatively account for experimental imperfections. It can also be extended in special cases to multi-level systems, such as designing adiabatic passages for spin $I > 1/2$ nuclei in NMR.

Moreover, we observe an interesting regime in which the protocol results in very fast pulses (with lengths as short as 2.5 Rabi cycles), that while slightly deviating from adiabaticity at limited times, still exhibit the high fidelity of conventional adiabatic operations. Even in cases where the inherent adiabatic robustness is compromised because of the control speed, the ability to directly tailor the system's Hilbert space trajectory to the existing perturbations renders our method a key candidate for applications that require short evolution times, along with the performance that comes from adiabaticity.

For the sake of concreteness, we will mostly focus our attention to adiabatic operations in the context of magnetic resonance. Our protocol is, however, not at all limited to this specific application[1].

1.1 Thesis Outline

The outline of this thesis is as follows:

- **Chapter 1**

  In the first chapter, we discuss the background required for developing our adiabatic control protocol. First, we review the fundamentals of time dependent perturbation theory, in a slightly more general setting than usual, where, unlike the time evolution of a (closed) quantum system, the generator of the dynamics is not necessarily anti-Hermitian. This will later be needed in the theoretical description of our control searches. Subsequently, we discuss the Van Loan auxiliary matrix formalism used for the efficient numerical calculation of the integral expressions frequently encountered in various parts of our control protocol, such as perturbation theory terms.

  We then turn to the adiabatic theorem, which is the basis for all adiabatic operations in physics. This is followed by an overview of adiabatic operations in the context of magnetic resonance, and the secant hyperbolic pulse as a standard pulse

[1] This project was done in collaboration with Holger Haas.

shape commonly utilized in an experimental setting. At the end of the chapter, we briefly review some of the previously established numerical protocols used for engineering adiabatic quantum operations.

- **Chapter 2**

  Chapter 2 is devoted to laying the theoretical foundations of the adiabatic control protocol for general two-level systems, including a discussion of the adiabatic control problem, the metrics used for quantifying control performance, and the efficient evaluation of these metrics along with their gradients with respect to the control parameters.

  Having established the basics of the protocol, we turn to the methods used in the optimization for the explicit inclusion of robustness criteria, such as robustness against inhomogeneities and perturbations in the Hamiltonian.

  We conclude the chapter by briefly presenting a generalization of the two-level problem to a special case of a multi-level system; engineering NMR adiabatic pulses for general spin $I > 1/2$ systems.

- **Chapter 3**

  Here we demonstrate the discussed control search method by presenting engineered adiabatic full passages for NMR applications, along with a pulse with built-in robustness against dipolar coupling, for magnetic resonance on interacting electrons. The performance of these pulses and the effectiveness of our perturbative treatment of the dipolar coupling are studied in multi-spin simulations. We also give a brief demonstration of an adiabatic operation connecting two arbitrary points on the Bloch sphere. The chapter ends with a study of the sensitivity of the pulses against stochastic noise, as a function of noise amplitude and characteristic fluctuation time.

- **Chapter 4**

  We summarize the results of the thesis, along with giving an outlook for future research directions.

1.2 Review of Time Dependent Perturbation Theory

Recall that the evolution of a closed quantum system with a Hamiltonian $H(t)$ and the initial (pure) state $|\psi_0\rangle$ is determined by the Schrodinger equation $i\hbar\frac{d}{dt}|\psi(t)\rangle = H(t)|\psi(t)\rangle$, together with the initial condition $|\psi(0)\rangle = |\psi_0\rangle$ [18]. This dynamics can equivalently be

described in terms of a unitary operator $U(t)$, called the time-evolution operator, which maps the initial state to the state at any time t by $U(t)|\psi_0\rangle = |\psi(t)\rangle$, where $U(t)$ is determined by the initial value problem (IVP)

$$\begin{cases} \dfrac{d}{dt}U(t) = -iH(t)U(t) \\ U(0) = \mathbb{1} \end{cases}, \tag{1.1}$$

with $\mathbb{1}$ being the identity operator. Eq.(1.1) is written in a unit system in which energies are measured in units of angular frequency, i.e. $\hbar = 1$. We will consistently use this unit system throughout this thesis.

The main problem in perturbation theory, first introduced by Dirac [19], discusses how the propagator changes when the Hamiltonian is varied by a small perturbation $\delta H(t)$, such that[1] $\|\delta H(t)\| \leq \|H(t)\|$ for all t. We here review the main results of perturbation theory in a slightly more general setting compared to most treatments, as this will prove useful in the control search algorithm. This review somewhat closely follows the first few sections of [17].

Let $G : [0, T] \to \mathcal{L}(\mathcal{H})$ be an operator-valued function on an interval $[0, T]$; with $\mathcal{L}(\mathcal{H})$ being the space of linear operators acting on a d-dimensional[2] complex Hilbert space $\mathcal{H}$. We will call G the *time-evolution generator* of the system. Now consider the following IVP:

$$\begin{cases} \dfrac{\partial}{\partial t}U_t[G] = G(t)U_t[G] \\ U_0[G] = \mathbb{1} \end{cases} \qquad t \in [0, T], \tag{1.2}$$

where $U_t[G]$, the solution to the IVP, is called the propagator of the system. In the case of a (closed) quantum system, $U_t[-iH]$ would be the time-evolution operator, with $H(t)$ being the Hamiltonian. Then, $G(t) = -iH(t)$ and $U_t[-iH]$ would be anti-Hermitian and unitary, respectively. We will not, however, impose any such constraints on the operators in this discussion.

The unique [20] solution of the above IVP is usually referred to as a time-ordered exponential, which we denote by

$$U_t[G] \equiv \mathrm{Texp}\Big[\int_0^t dt' G(t')\Big]. \tag{1.3}$$

[1] We use the Hilbert Schmidt inner product $\langle A, B\rangle \equiv \mathrm{Tr}(A^\dagger B)$, and its associated norm $\|A\| = \sqrt{\langle A, A\rangle}$ throughout this thesis, unless otherwise specified.

[2] We will always assume $d < \infty$ for simplicity.

In the case of a constant generator $G(t) \equiv G_0$, one can easily show by direct substitution that this reduces to the operator exponential $U_t[G_0] = \exp(tG_0)$. In the slightly more general case of a generator that commutes with itself at all times[1], the solution to the IVP becomes $U_t[G] = \exp[\int_0^t dt' G(t')]$, which can also be verified by directly checking that it satisfies Eq.(1.2).

As can be seen from Eq.(1.3), at any time t, $U_t[G]$ depends on the whole history of the generator before that time, i.e. the set $\{G(t')|\ 0 \leq t' \leq t\}$. In other words, U_t is a functional of the generator. To emphasize this functional relationship, we use the notation $U_t[G]$ instead of the more common $U(t)$ in this thesis; unless in cases where such emphasis is not needed.

Now consider the case where the solution $U_t[G]$ to Eq.(1.2) is known for a specific G, and we wish to calculate the solution $U_t[G + \delta G]$ for a perturbed generator $G + \delta G$. We discuss two different expansions for calculating the perturbed solution, the Dyson series [21] and the Magnus series [22].

The Dyson Series

To derive the Dyson series, first note that since $\frac{\partial}{\partial t}\Big[U_t^{-1}[G] \times U_t[G]\Big] = \frac{\partial}{\partial t}\mathbb{1} = 0$, one can easily use Eq.(1.2) to show that $U_t^{-1}[G]$ satisfies the following IVP:

$$\begin{cases} \dfrac{\partial}{\partial t} U_t^{-1}[G] = -U_t^{-1}[G]\ G(t) \\ U_0^{-1}[G] = \mathbb{1} \end{cases} \qquad t \in [0, T]. \tag{1.4}$$

Now to calculate the perturbed $U_t[G + \delta G]$, we look at the time derivative of the product $U_t^{-1}[G] \times U_t[G + \delta G]$,

$$\begin{aligned} \frac{\partial}{\partial t}\Big[U_t^{-1}[G] \times U_t[G + \delta G]\Big] &= \left(\frac{\partial}{\partial t} U_t^{-1}[G]\right) U_t[G + \delta G] + U_t^{-1}[G]\ \frac{\partial}{\partial t} U_t[G + \delta G] \\ &= -U_t^{-1}[G]\ G(t)\ U_t[G + \delta G] \\ &\qquad + U_t^{-1}[G]\ \Big(G(t) + \delta G(t)\Big)\ U_t[G + \delta G] \\ &= U_t^{-1}[G]\ \delta G(t)\ U_t[G + \delta G], \end{aligned} \tag{1.5}$$

[1] i.e. $[G(t_1), G(t_2)] = 0$ for all $t_1, t_2 \in [0, T]$.

where we used Eq.(1.2) and Eq.(1.4). Integrating Eq.(1.5) and applying $U_t[G]$ from the left gives

$$U_t[G+\delta G] = U_t[G] \int_0^t dt' \; U_{t'}^{-1}[G] \; \delta G(t') \; U_{t'}[G+\delta G]. \tag{1.6}$$

This is a linear Volterra integral equation of the second kind for $U_t[G+\delta G]$, which can be solved by iteration (i.e. a Neumann series) [23]. The result is the *Dyson series*,

$$U_t[G+\delta G] = U_t[G] \sum_{n=0}^{\infty} \int_0^t dt_1 ... \int_0^{t_{n-1}} dt_n \; \prod_{i=1}^{n} U_{t_i}^{-1}[G] \; \delta G(t_i) \; U_{t_i}[G]. \tag{1.7}$$

The order of the product in Eq.(1.7) is understood to be in increasing value of i, from left to right. Eq.(1.7) may also be written in its more conventional form by utilizing the interaction picture of G,

$$\tilde{U}_t[\delta\tilde{G}] = \sum_{n=0}^{\infty} \int_0^t dt_1 ... \int_0^{t_{n-1}} dt_n \; \prod_{i=1}^{n} \delta\tilde{G}(t_i), \tag{1.8}$$

with

$$\begin{cases} \delta\tilde{G}(t) \equiv U_t^{-1}[G] \; \delta G(t) \; U_t[G] \\ \tilde{U}_t[\delta\tilde{G}] \equiv U_t^{-1}[G] \; U_t[G+\delta G] \end{cases} \tag{1.9}$$

being the interaction picture operators.

Since the Dyson series of Eq.(1.7) involves reoccurring integrals of a particular form, we use the following shorthand notation for these *Dyson terms*:

$$\mathcal{D}_U(\mathbf{A};t) \equiv U_t[G] \int_0^t dt_1 ... \int_0^{t_{M-1}} dt_M \; \prod_{i=1}^{M} U_{t_i}^{-1}[G] \; A_i(t_i) \; U_{t_i}[G], \tag{1.10}$$

with $\mathbf{A} \equiv (A_1, ..., A_M)$. This notation allows us to write the Dyson series in a more condensed form

$$U_t[G+\delta G] = \sum_{n=0}^{\infty} \mathcal{D}_U(\underbrace{\delta G, ...\delta G}_{n \text{ times}}; t). \tag{1.11}$$

As a side note, these Dyson terms can also be related to directional derivatives of $U_t[G]$. For example, when G is varied in the direction of some operator-valued function A, the n^{th} order directional derivative is

$$\frac{\partial^n}{\partial \epsilon^n} U_t[G+\epsilon A]\bigg|_{\epsilon=0} = n! \; \mathcal{D}_U(\underbrace{A, ..., A}_{n \text{ times}}; t). \tag{1.12}$$

This can be easily verified by setting $\delta G = \epsilon A$ in Eq.(1.7) and taking the partial derivative $\partial^n/\partial\epsilon^n|_{\epsilon=0}$. Interestingly, a comparison of Eq.(1.12) and Eq.(1.11) shows that the Dyson series is nothing but the Taylor series of the propagator around the unperturbed generator G. It is worth noting that even though Eq.(1.7) is exact for any G and δG, an approximation using a truncation of the Dyson series requires that $\|\delta G(t)\| \ll \|G(t)\|$ for all $t \in [0, T]$; i.e. G is the "large" solvable generator and δG is the perturbation.

Note that in the special case of $G(t)$ being the anti-Hermitian generator of a quantum system's time evolution, approximating the perturbed propagator by truncating the Dyson series can generally result in a non-unitary operator. One way of alleviating this problem is by using the exponential of an infinite series instead to represent the propagator; a technique called the Magnus expansion.

The Magnus Expansion

The idea behind the Magnus expansion [22, 24] is to write the interaction picture IVP solution $\tilde{U}_t[\delta\tilde{G}]$ of Eq.(1.9) as the exponential of another operator. There are two advantages to this approach: 1- It allows for studying the system dynamics through an *average generator* at any specific time. 2- As we will see later, in contrast to the Dyson series, truncation of the resulting expansion still results in a unitary evolution when the generator is anti-Hermitian.

Consider the case where one is interested in the perturbed propagator $U_{t_0}[G + \delta G]$ at a specific time t_0. This can be, for example, the end of a control sequence. Recall that the operator exponential is surjective as a map from $\mathcal{L}(\mathcal{H})$ to the set of invertible operators on[1] $\mathcal{H}$ [25]. This implies that any invertible operator, such as the interaction picture propagator $\tilde{U}_{t_0}[\delta\tilde{G}]$, can be written as an exponential

$$\tilde{U}_{t_0}[\delta\tilde{G}] = e^{t_0\delta\tilde{\mathcal{G}}(t_0)}, \tag{1.13}$$

where the exponent is written as $t_0 \times \delta\tilde{\mathcal{G}}(t_0)$ without loss of generality. Note that the operator $\tilde{U}_{t_0}[\delta\tilde{G}]$ is indeed invertible since its inverse is the unique solution of an IVP analogous to Eq.(1.4). On the other hand, we know that the solution to the Eq.(1.2) IVP for a constant generator G_0 is simply $\exp(tG_0)$, which has the exact same form as Eq.(1.13) as long as we restrict ourselves to the specific, fixed time t_0. In other words, for any specific t_0, the time-independent generator $\delta\tilde{\mathcal{G}}(t_0)$, called the *average generator*, simulates the original system $\delta\tilde{G}(t)$ at $t = t_0$. Note, however, that the propagators of the

[1] i.e. the general linear group of $\mathcal{H}$.

two systems can in principle follow completely different trajectories in $\mathcal{L}(\mathcal{H})$; only needing to coincide at $t = t_0$.

In most cases, the time t_0 is taken to be the end of the applied controls (e.g. the pulse sequence) $t_0 = T$. In the case of unitary evolution, Eq.(1.13) allows for the definition of an average Hamiltonian $\tilde{\mathscr{H}}(t_0) := i\ \delta\tilde{\mathcal{G}}(t_0)$, which is the focus of average Hamiltonian theory [26, 27]; with various applications in the design and analysis of pulse sequences for magnetic resonance.

With that in mind, we turn to the actual calculation of the average generator $\delta\tilde{\mathcal{G}}(t_0)$. To this end, we make the transformation $\delta\tilde{G} \to \lambda\delta\tilde{G}$ with $\lambda \in \mathbb{R}$ being an auxiliary bookkeeping parameter that is set to 1 at the end. We then use the ansatz

$$\delta\tilde{\mathcal{G}}(t_0) \equiv \sum_{i=1}^{\infty} \lambda^i \delta\tilde{\mathcal{G}}_i(t_0), \tag{1.14}$$

and equate $\exp[t_0\delta\tilde{\mathcal{G}}(t_0)] = \exp[t_0 \sum_{i=0}^{\infty} \lambda^i \delta\tilde{\mathcal{G}}_i(t_0)] = \sum_{j=0}^{\infty} \frac{t_0^j}{j!} \big(\sum_{i=1}^{\infty} \lambda^i \delta\tilde{\mathcal{G}}_i(t_0)]\big)^j$ with the interaction picture Dyson series Eq.(1.8). Equating corresponding powers of λ and then setting $\lambda = 1$ at the end gives the Magnus expansion,

$$\tilde{U}_{t_0}[\delta\tilde{G}] = \exp\Big[t_0 \sum_{i=1}^{\infty} \delta\tilde{\mathcal{G}}_i(t_0)\Big], \tag{1.15}$$

with the first few terms being

$$\begin{cases} \delta\tilde{\mathcal{G}}_1(t_0) = \dfrac{1}{t_0}\displaystyle\int_0^{t_0} dt_1 \delta\tilde{G}(t_1) \\ \delta\tilde{\mathcal{G}}_2(t_0) = \dfrac{1}{2t_0}\displaystyle\int_0^{t_0} dt_1 \int_0^{t_1} dt_2 [\delta\tilde{G}(t_1), \delta\tilde{G}(t_2)] \\ \delta\tilde{\mathcal{G}}_3(t_0) = \dfrac{1}{6t_0}\displaystyle\int_0^{t_0} dt_1 \int_0^{t_1} dt_2 \int_0^{t_3} dt_3 \Big(\Big[\delta\tilde{G}(t_1), [\delta\tilde{G}(t_2), \delta\tilde{G}(t_3)]\Big] \\ \qquad\qquad + \Big[\delta\tilde{G}(t_3), [\delta\tilde{G}(t_2), \delta\tilde{G}(t_1)]\Big]\Big) \\ ... \end{cases} . \tag{1.16}$$

A general formula for the n^{th} term of the Magnus expansion is rather complicated, and involves the Bernoulli numbers and n nested commutators of $\delta\tilde{G}$ [24].

Note that even though we could have written Eq.(1.13) directly for $U_{t_0}[G + \delta G]$ instead of $\tilde{U}_{t_0}[\delta\tilde{G}]$, the advantage of using the interaction picture is that the expansion terms of Eq.(1.16) are "small", as $\|\delta\tilde{G}(t)\| = \|U_t^{-1}[G]\ \delta G(t)\ U_t[G]\| = \|\delta G(t)\| \ll \|G(t)\|$. Since the

n^{th} Magnus term is of order $\|\delta\tilde{G}\|^n$, this allows for an approximation of the average generator $\delta\tilde{\mathcal{G}}(t_0)$ by truncation of the infinite series in Eq.(1.15). We also make the observation that since the (Lie) algebra of anti-Hermitian operators is closed under commutation, in the case of an anti-Hermitian generator $\delta\tilde{G}$, each Magnus term $\delta\tilde{\mathcal{G}}_i$ is also anti-Hermitian, and truncation will always result in a unitary propagator.

In our review of perturbation theory, we have thus far encountered integral expressions such as the Dyson and Magnus terms Eq.(1.10,1.16), for which direct numerical integration can be time consuming; especially since the propagator would need to be calculated by numerically solving the IVP Eq.(1.2) beforehand. In the next section, we will discuss the block matrix methods that can substantially speed up the computations by calculating these reoccurring integral expressions alongside the propagator, through only a single IVP.

1.3 Calculating Dyson Terms Using Van Loan Relations

The efficient calculation of the propagator and its properties is a crucial component of any numerical control method. Many such properties are integrals of the form

$$U_t[G]\int_0^t dt_1 ... \int_0^{t_{n-1}} dt_n \; f(t_1,...,t_n)\prod_{m=1}^{n} U_{t_m}^{-1}[G]\; A_m(t_m)\; U_{t_m}[G], \tag{1.17}$$

for some scalar function $f:[0,T]^n \to \mathbb{C}$, and operator-valued functions $A_m:[0,T]\to\mathcal{L}(\mathcal{H})$, with $m\in\{1,...,n\}$. An important example of such expressions are the Dyson terms

$$\mathcal{D}_U(\mathbf{A};t) = U_t[G]\int_0^t dt_1 ... \int_0^{t_{n-1}} dt_n \; \prod_{m=1}^{n} U_{t_m}^{-1}[G]\; A_m(t_m)\; U_{t_m}[G], \tag{1.18}$$

that as established in Section 1.2, appear in perturbation theory, as well as the directional derivatives of the propagator. Note that Magnus terms can also be written in terms of the Dyson terms $\mathcal{D}_U(\mathbf{A};t)$ [24]. Another example of such integrals is expressions in stochastic Liouville theory [28] for evaluating the ensemble average of a quantum system subject to stochastic operators.

In this section, we will only focus on the method used to efficiently calculate integrals of the above form in the special case of $f(t_1,..,t_n)=1$, i.e. the Dyson terms Eq.(1.18), as the more general expression is not needed for our adiabatic control protocol [1]. The main idea

[1] A more general discussion for the $f(t_1,..,t_n)\neq 1$ case is given in [17, 29].

behind this method is that computations are significantly faster if instead of solving the IVP for the propagator $U_t[G]$ and then using it to evaluate the Dyson terms, one constructs a larger auxiliary matrix for which the IVP of Eq.(1.2) can give both the propagator and the Dyson terms simultaneously. This capability is especially vital in applications such as numerical control optimization, where hundreds, if not thousands of computations may be required in order to find the parameters satisfying the design criteria.

The backbone of this auxiliary matrix formalism is a relation first discovered by Van Loan [30] involving the time-ordered exponentials of block triangular matrices, which was then further generalized in [17, 31, 32]. In this thesis, we only need to use a special case of these *Van Loan relations*. In particular, for any square-matrix valued function G, and its associated propagator $U_t[G] \equiv \mathrm{Texp}\Big[\int_0^t dt' G(t')\Big]$, we have the identity

$$\mathrm{Texp}\left(\int_0^t dt' \begin{bmatrix} G(t') & A_1(t') & 0 & \dots & 0 & 0 \\ 0 & G(t') & A_2(t') & \dots & 0 & 0 \\ 0 & 0 & G(t') & \dots & 0 & 0 \\ \vdots & \vdots & \vdots & \ddots & \vdots & \vdots \\ 0 & 0 & 0 & \dots & G(t') & A_n(t') \\ 0 & 0 & 0 & \dots & 0 & G(t') \end{bmatrix}\right) =$$

$$\begin{bmatrix} U_t[G] & \mathcal{D}_U(A_1;t) & \mathcal{D}_U(A_1,A_2;t) & \dots & \mathcal{D}_U(A_1,...,A_{n-1};t) & \mathcal{D}_U(A_1,...,A_n;t) \\ 0 & U_t[G] & \mathcal{D}_U(A_2;t) & \dots & \mathcal{D}_U(A_2,...,A_{n-1};t) & \mathcal{D}_U(A_2,...,A_n;t) \\ 0 & 0 & U_t[G] & \dots & \mathcal{D}_U(A_3,...,A_{n-1};t) & \mathcal{D}_U(A_3,...,A_n;t) \\ \vdots & \vdots & \vdots & \ddots & \vdots & \vdots \\ 0 & 0 & 0 & \dots & U_t[G] & \mathcal{D}_U(A_n;t) \\ 0 & 0 & 0 & \dots & 0 & U_t[G] \end{bmatrix}, \quad (1.19)$$

the right-hand side of which contains both the propagator and the Dyson terms (see Appendix A for a proof). Eq.(1.19) can thus be used to construct an auxiliary matrix that when used as the generator of Eq.(1.2), facilitates the calculation of the propagator and Dyson terms.

This strategy has been previously utilized to engineer unitary operations robust to various perturbations and stochastic noise [17], calculate gradients and Hessians of the propagator for gradient-based optimization algorithms [33,34], and further develop numerical calculations in spin relaxation theories [32]. In this work, we will show that one can construct a metric for the adiabaticity of a quantum operation which can be written in the form of a Dyson term, and hence efficiently calculated through the Van Loan auxiliary matrix formalism.

This concludes our review of time dependent perturbation theory, and the Van Loan formalism for calculating the expressions therein. We will now move on to discuss the basics of adiabatic quantum evolution, and its applications, particularly in the field of magnetic resonance.

1.4 Adiabatic Quantum Evolution

In this section, we give a brief overview of the concept of adiabatic evolution in quantum mechanics, starting with the central result on which adiabatic operations stand; the adiabatic theorem. We then turn to adiabatic operations in the context of magnetic resonance, as that is the primary (although not the only) focus of the present work. We end our review by discussing the secant hyperbolic pulse as one of the commonly used adiabatic inversion pulses in magnetic resonance experiments. This standardized pulse shape is later utilized in Chapter 3 as a reference for benchmarking our numerically derived adiabatic pulses.

1.4.1 The Adiabatic Theorem

Consider a quantum system with a Hamiltonian $H(t)$ acting on a finite-dimensional Hilbert space $\mathcal{H}$. In accordance with the standard treatment of the adiabatic theorem, we will assume that the spectrum of $H(t)$ is non-degenerate at all times, such that we can unambiguously label each eigenstate and keep track of it throughout the evolution. We denote these instantaneous energy eigenstates in the relevant time interval $[0, T]$ by $|E_n(t)\rangle$. Generalizations to the case of degenerate [35–37] and continuous [38] spectra exist in the literature, and are outside the scope of this work.

Roughly speaking, the adiabatic theorem states that if the time variation of the Hamiltonian is much slower than the intrinsic dynamical time scale of the system, an energy eigenstate $|E_n(0)\rangle$ at some time $t = 0$ stays in the corresponding instantaneous eigenspace during the evolution. In other words, if the system starts from an energy eigenstate, it stays an instantaneous eigenstate under the dynamics.

More precisely, the adiabatic theorem states that provided the adiabatic condition

$$\underset{\substack{n,m\in\{1,..,d\}\\ t\in[0,T]}}{\text{Max}} \frac{|\langle E_m(t)|\frac{d}{dt}H(t)|E_n(t)\rangle|}{|E_n(t) - E_m(t)|^2} \ll 1, \tag{1.20}$$

is satisfied, initial eigenstates evolve as

$$U(t)|E_k(0)\rangle \simeq e^{i\phi_k(t)}|E_k(t)\rangle \qquad t \in [0,T], \tag{1.21}$$

with $U(t)$ being the propagator[1], and the phase ϕ_k being

$$\phi_k(t) \equiv \underbrace{-\int_0^t dt' E_k(t')}_{\text{dynamic phase}} + \underbrace{\int_0^t dt' i\langle E_k(t')|\frac{d}{dt'}|E_k(t')\rangle}_{\text{geometric phase}}. \tag{1.22}$$

The first term in Eq.(1.22) is the *dynamic phase*, which is the extension of the static-Hamiltonian e^{-iEt} oscillatory phase. The second term is called the *geometric*, or *Berry phase*, which leads to a wide range of interesting effects in various parts of modern physics [39–41].

Observe that the adiabatic condition Eq.(1.20) depends on two factors, the numerator measures the rate of the Hamiltonian's time variation, while the denominator is the squared inverse of the energy level spacing. Consequently, systems with larger energy gaps can evolve adiabatically even under faster Hamiltonians.

An essential property of adiabatic operations is their inherent robustness against both errors in the applied controls and decoherence [42]. Errors in the controls, such as imperfect pulse amplitudes, can be modeled using an error Hamiltonian $\delta H(t)$; with the actual Hamiltonian of the system now being $H(t) + \delta H(t)$. Interestingly, Eq.(1.20) implies that the error Hamiltonian $\delta H(t)$ need not be that much smaller than the ideal Hamiltonian $H(t)$. Provided $\delta H(t)$ varies sufficiently slowly, and its start and end values are small enough, the operation will still result in the same final state, even though the eigenstate trajectories may, in principle, be very different. Conversely, errors that vary much faster than the energy scale of $H(t)$ are also not detrimental to the performance, as the system response is not fast enough to be affected by them. Therefore, only control errors in the intermediate speed regime are able to harm the performance of adiabatic operations.

Regarding robustness against decoherence, environmental interactions that couple the eigenstates of the Hamiltonian may induce unwanted transitions and impair the performance of the operation. This, however, is not problematic, as long as the associated temperature is much smaller than the minimum energy gap of $H(t)$. And since the adiabatic condition Eq.(1.20) actually favors larger gaps, and hence less stringent temperature requirements, adiabatic operations are usually not very susceptible to decoherence at typical operating conditions [42–44].

[1]We use the simplified notation $U(t)$ instead of $U_t[G]$ for the propagator, since, in this section, there will be no need for emphasizing its functional relationship with the generator.

We here conclude our discussion of the adiabatic theorem. A more extensive review of the adiabatic theorem and its derivation is provided in Appendix B for completeness. In the following section, we will discuss how adiabatic operations can be implemented in the context of magnetic resonance experiments.

1.4.2 Adiabatic Operations in Magnetic Resonance

Here we first review the basic setting of a magnetic resonance experiment, and how frequency-modulated (FM) radio-frequency (RF) pulses can lead to a reliable method for the adiabatic manipulation of spins [45]. This is followed by a brief overview of the hyperbolic secant pulse as one of the standard waveforms utilized in many magnetic resonance experiments.

Frequency-Modulated RF Pulses as Adiabatic Operations

The simplified description of a typical magnetic resonance system is as follows [4, 5, 46]. A spin I particle, e.g. a nucleus or electron, is placed inside a static magnetic field $\mathbf{B}_0 \equiv B_0\hat{\mathbf{z}}$, with an inductive coil generating an orthogonal RF field $\mathbf{B}_1(t)$. The Hamiltonian of the system is simply given by the classical magnetic dipole interaction $-\boldsymbol{\mu}\cdot\mathbf{B}$, with the magnetic dipole moment $\boldsymbol{\mu}$ being proportional to the particle spin, i.e. $\boldsymbol{\mu} = \gamma\mathbf{I}$, and the proportionality constant γ being the gyromagnetic ratio of the particle. The Hamiltonian of the system then is

$$H(t) = -\gamma(B_0\hat{\mathbf{z}} + \mathbf{B}_1(t))\cdot\mathbf{I}. \tag{1.23}$$

Now consider the case where the RF field is linearly polarized, and both amplitude and frequency modulated, such that $\mathbf{B}_1(t) = 2[B_{1I}(t)\cos\varphi(t) + B_{1Q}(t)\sin\varphi(t)]\hat{\mathbf{x}}$, with $B_{1I}(t)$ and $B_{1Q}(t)$ being the in-phase and quadrature envelope functions, and the instantaneous (angular) frequency being $\dot{\varphi}(t) \equiv \frac{d}{dt}\varphi(t)$. With this in mind, Eq.(1.23) becomes

$$H(t) = -\omega_0 I_z - 2\big[\omega_{1I}(t)\cos\varphi(t) + \omega_{1Q}(t)\sin\varphi(t)\big]I_x, \tag{1.24}$$

where $\omega_0 \equiv \gamma B_0$ is the Larmor frequency, $\omega_{1I}(t) \equiv \gamma B_{1I}(t)$, and $\omega_{1Q}(t) \equiv \gamma B_{1Q}(t)$. To see how one can create adiabatic operations in this setting, it is convenient to change to a reference frame rotating around the static field axis at the instantaneous RF frequency $\dot{\varphi}(t)$. We will call this new reference frame, defined by the unitary transformation $\exp[-i\varphi(t)I_z]$, the *FM frame*.

Before we proceed with the reference frame transformation, we note that in most magnetic resonance experiments, the static field is on the order of a few Tesla, while the RF field is not higher than a few hundred Gauss at most. We therefore restrict our analysis to a regime in which $|\omega_{1I}(t)|, |\omega_{1Q}(t)| \ll \omega_0$. We also assume that the instantaneous frequency $\dot{\varphi}(t)$ is close to the Larmor frequency throughout the evolution, in the sense that the instantaneous resonance offset $\Delta\omega(t) \equiv \omega_0 - \dot{\varphi}(t)$ is much smaller than the Larmor frequency at all times.

We now rewrite Eq.(1.24) as

$$H(t) = \underbrace{-\dot{\varphi}(t) I_z}_{H_0(t)} \underbrace{-\Delta\omega(t) I_z - 2\big[\omega_{1I}(t)\cos(\varphi(t)) + \omega_{1Q}(t)\sin(\varphi(t))\big] I_x}_{\delta H(t)}, \tag{1.25}$$

with $\|\delta H(t)\| \ll \|H_0(t)\|$ because of the above assumptions. Realizing that the FM frame is nothing but the interaction frame of $H_0(t)$, the Magnus expansion can be used to calculate an effective FM-frame Hamiltonian. To do this, we partition the time interval $[0, T]$ into smaller windows of length δt, and then use the Magnus expansion to first order in order to derive an average Hamiltonian for each time frame. δt is chosen to be much longer than the Larmor period $2\pi/\omega_0$, and much smaller than the time scale for the variation of the envelope functions $\omega_{1I}(t), \omega_{1Q}(t)$, and also the resonance offset function $\Delta\omega(t)$.

The first order average Hamiltonian for the window $[t, t+\delta t]$ is

$$\begin{aligned}
\tilde{H}(t) &\simeq \frac{1}{\delta t}\int_t^{t+\delta t} dt'\; e^{-i\varphi(t')I_z}\delta H(t') e^{i\varphi(t')I_z} \\
&= \frac{1}{\delta t}\int_t^{t+\delta t} dt' \Bigg(-\Delta\omega(t')I_z - 2\big[\omega_{1I}(t')\cos\varphi(t') \\
&\qquad\qquad + \omega_{1Q}(t')\sin\varphi(t')\big]\big[I_x\cos\varphi(t') + I_y\sin\varphi(t')\big]\Bigg) \\
&= -\frac{1}{\delta t}\int_t^{t+\delta t} dt' \Bigg(\Delta\omega(t')I_z + \omega_{1I}(t')I_x + \omega_{1Q}(t')I_y \\
&\qquad + \big(\omega_{1I}(t')I_y + \omega_{1Q}(t')I_x\big)\sin(2\varphi(t')) \\
&\qquad - \big(\omega_{1I}(t')I_x - \omega_{1Q}(t')I_y\big)\cos(2\varphi(t'))\Bigg).
\end{aligned} \tag{1.26}$$

Now since δt is much larger than the Larmor period, the $\sin(2\varphi(t')), \cos(2\varphi(t'))$ average out, as they oscillate with a frequency $\dot{\varphi}(t) \sim \omega_0$. The remaining terms can be taken out

of the integral, since δt is much smaller than their variational time scale. This leads to the following effective Hamiltonian in the FM frame:

$$\tilde{H}(t) \simeq -\Delta\omega(t) I_z - \omega_{1I}(t) I_x - \omega_{1Q}(t) I_y, \tag{1.27}$$

or

$$\tilde{H}(t) \simeq -\mathbf{b}(t) \cdot \mathbf{I}, \tag{1.28}$$

with $\mathbf{b}(t) \equiv (\omega_{1I}(t), \omega_{1Q}(t), \Delta\omega(t))$ being the *effective field*. The coarse-graining approach used here to derive this effective Hamiltonian is usually referred to as the *rotating wave approximation* (RWA) [47], as it is equivalent to decomposing the linearly polarized $\mathbf{B}_1$ into two counter-rotating circularly polarized fields, and neglecting the one that rotates opposite to the spin's Larmor precession. In this thesis, we will always work in the FM frame, assuming that the conditions required for the RWA are satisfied.

The FM frame Hamiltonian Eq.(1.28) clearly shows that one can engineer a specific trajectory for the effective field, and hence the Hamiltonian, by varying the envelope functions and the resonance offset signal in the experiment. In particular, adiabatic evolution can be achieved provided this is done sufficiently slowly, in the sense that the adiabatic condition Eq.(1.20) is satisfied.

We now spend some time examining the eigenstate structure of Eq.(1.28), as it will be useful for later extending our adiabatic control protocol to the case of $I > 1/2$ spins. Denoting the eigenbasis of the I_z operator[1] by $\{|m\rangle\}_{m=-I}^{I}$, we can derive the eigenstates of $\tilde{H}(t)$ by rotating the coordinate frame into one in which the effective field coincides with the z axis. Writing the effective field $\mathbf{b}(t)$ in spherical coordinates according to Fig.(1.1), this coordinate transformation corresponds to a rotation around the y axis by the polar angle $\vartheta(t)$, followed by a rotation around the (old) z axis by the azimuthal angle $\psi(t)$. Indicating the associated rotation operator by $\mathcal{R}(t) \equiv e^{-i\psi(t)I_z} e^{-i\vartheta(t)I_y}$, we have the following transformation property for the Hamiltonian:

$$\mathcal{R}^\dagger(t) \tilde{H}(t) \mathcal{R}(t) = -|\mathbf{b}(t)| I_z, \tag{1.29}$$

or equivalently $\tilde{H}(t)\mathcal{R}(t) = -|\mathbf{b}(t)|\mathcal{R}(t) I_z$. Acting both sides on a Zeeman state $|m\rangle$ gives

$$\tilde{H}(t)\big(\mathcal{R}(t)|m\rangle\big) = -m|\mathbf{b}(t)|\big(\mathcal{R}(t)|m\rangle\big), \tag{1.30}$$

meaning that the eigenvectors of the FM frame Hamiltonian are $|E_m(t)\rangle \equiv \mathcal{R}(t)|m\rangle$, with the associated eigenvalues being $-m|\mathbf{b}(t)|$, for $m \in \{-I, ..., I\}$. Note that as required

[1] We will call this the *Zeeman basis* throughout this thesis.

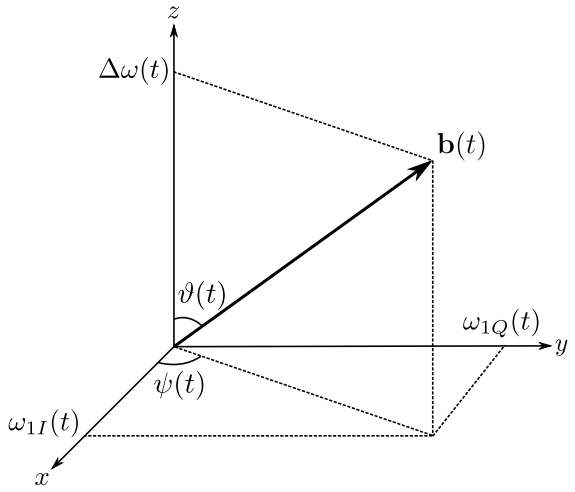

Figure 1.1: The effective field in the FM frame.

by the adiabatic theorem, the spectrum is always non-degenerate provided $\mathbf{b}(t) \neq 0$ at all times. The eigenstates can be explicitly written in the Zeeman basis using the Wigner small d-matrices [18] defined by $d^{(I)}_{m'm}(\vartheta) \equiv \langle m'|e^{-i\vartheta I_y}|m\rangle$, the values of which are summarized in Appendix C. This can be done by writing

$$\begin{aligned} |E_m(t)\rangle &= e^{-i\psi(t)I_z}e^{-i\vartheta(t)I_y}|m\rangle \\ &= e^{-i\psi(t)I_z}\sum_{m'=-I}^{I}|m'\rangle\langle m'|e^{-i\vartheta(t)I_y}|m\rangle, \end{aligned} \tag{1.31}$$

which gives

$$|E_m(t)\rangle = \sum_{m'=-I}^{I} e^{-im'\psi(t)}d^{(I)}_{m'm}(\vartheta(t))|m'\rangle. \tag{1.32}$$

Another important property of adiabatic evolution can be deduced by examining the dynamics of the total magnetization. Assuming that the system starts in the eigenstate $|\psi(0)\rangle = |E_m(0)\rangle$, and the evolution is adiabatic so that $|\psi(t)\rangle \simeq e^{i\phi_m(t)}|E_m(t)\rangle$, the magnetization evolves as

$$\begin{aligned} \mathbf{M}(t) &= \langle\psi(t)|\mathbf{I}|\psi(t)\rangle \\ &= \langle E_m(t)|\mathbf{I}|E_m(t)\rangle \\ &= \langle m|\mathcal{R}^\dagger(t)\mathbf{I}\mathcal{R}(t)|m\rangle. \end{aligned} \tag{1.33}$$

An explicit calculation of Eq.(1.33) using $\mathcal{R}(t) = e^{-i\psi(t)I_z}e^{-i\vartheta(t)I_y}$ results in

$$\begin{aligned}\mathbf{M}(t) &= m\big(\cos\psi(t)\sin\vartheta(t), \sin\psi(t)\sin\vartheta(t), \cos\vartheta(t)\big) \\ &= m\frac{\mathbf{b}(t)}{|\mathbf{b}(t)|},\end{aligned} \tag{1.34}$$

i.e. the magnetization follows the effective field direction during adiabatic evolution. Note that this also applies when the initial state is a statistical mixture of the eigenstates, such as the high temperature thermal state frequently encountered in magnetic resonance.

As a final remark, we briefly mention that the adiabatic condition Eq.(1.20) for the FM Hamiltonian of a spin I particle simplifies to (see Appendix D)

$$\frac{2I+1}{4}\max_{t\in[0,T]}\frac{\Omega(t)}{|\mathbf{b}(t)|} \ll 1, \tag{1.35}$$

with $\Omega(t)$ being the instantaneous angular velocity associated with the motion of the effective field direction $\mathbf{b}(t)/|\mathbf{b}(t)|$. This implies that in order for the evolution to be adiabatic, the direction of the effective field needs to vary slowly relative to the its magnitude, which is in turn determined by the magnitude of the Rabi field $\omega_{1I}(t), \omega_{1Q}(t)$, as well as the resonance offset $\Delta\omega(t)$.

We will now discuss one of the most common types of adiabatic operations, the adiabatic inversion pulse.

Adiabatic Inversion Pulses in Magnetic Resonance

The ability for high fidelity population inversion is an essential component of many techniques in magnetic resonance spectroscopy and imaging. Adiabatic inversion pulses [45, 48, 49], also known as adiabatic full passages (AFP), have become a reliable method for population inversion in the presence of static and RF field inhomogeneities, where normal resonant π pulses become problematic.

In an AFP, the spin starts out pointing in the $\hat{\mathbf{z}}$ direction in one of the Zeeman states $|m\rangle$ (or a mixture of them). With the resonance offset being set to its maximum value $\Delta\omega_{\max}$, and the Rabi strength being zero, the initial effective field $\mathbf{\Omega}(0) = \Delta\omega_{\max}\hat{\mathbf{z}}$ points in the same direction as the magnetization. As depicted in Fig.(1.2), by gradually increasing the Rabi strength and sweeping the frequency through resonance ($\Delta\omega = 0$), the effective field is rotated into the transverse plane and then into the $-\hat{\mathbf{z}}$ direction, with the Rabi strength and resonance offset going back to zero and $-\Delta\omega_{\max}$ at the very end, respectively. Provided the effective field varies sufficiently slowly, in the sense that it satisfies Eq.(1.35),

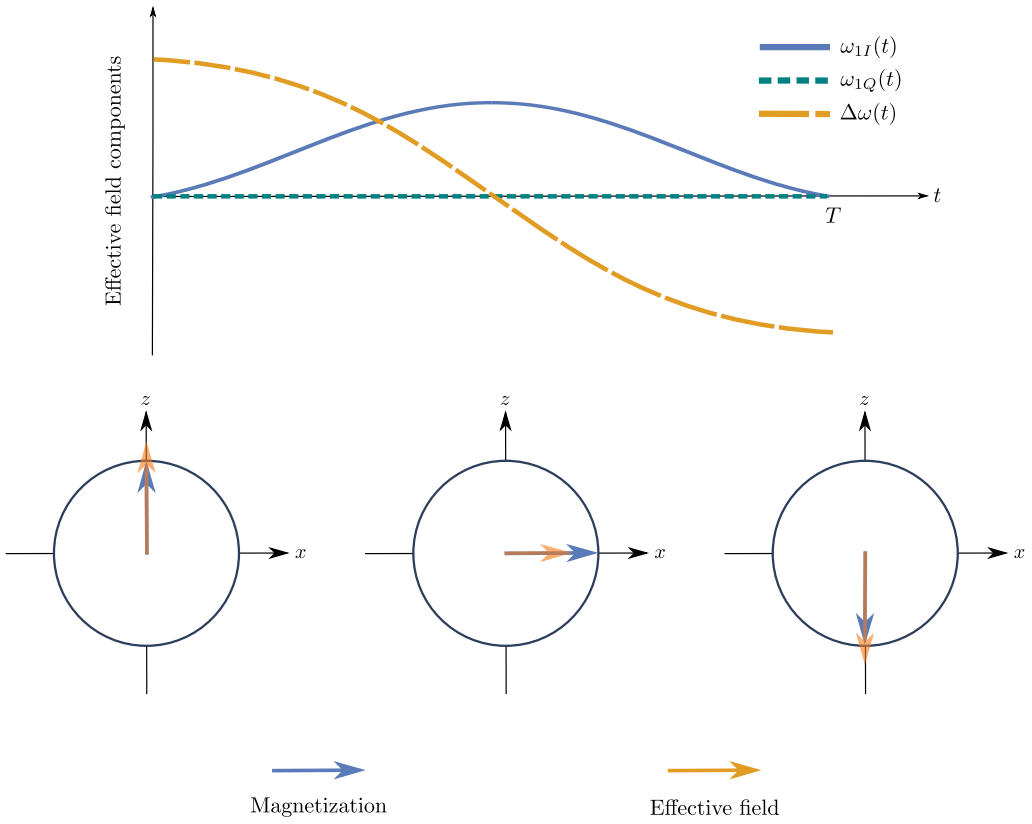

Figure 1.2: Typical adiabatic full passage pulse, along with its associated magnetization and effective field trajectories.

the magnetization will follow its trajectory and undergo an adiabatic inversion from $\hat{\mathbf{z}}$ to $-\hat{\mathbf{z}}$.

One of the established waveforms for the modulation functions $\omega_{1I}, \omega_{1Q}, \Delta\omega$ of an AFP is the hyperbolic secant pulse, which was first introduced in the field of coherent optics, and later utilized in magnetic resonance experiments [49, 50]. The hyperbolic secant pulse is defined with the modulation functions

$$\begin{cases} \omega_{1I}(t) = \omega_{1\max}\ \mathrm{sech}\left[(1-\dfrac{2t}{T})\ \mathrm{sech}^{-1}\kappa\right] \\ \omega_{1Q}(t) = 0 \\ \Delta\omega(t) = \Delta\omega_{\max}\ \tanh\left[(1-\dfrac{2t}{T})\ \mathrm{sech}^{-1}\kappa\right] \end{cases}, \tag{1.36}$$

where $\omega_{1\max}$ and $\Delta\omega_{\max}$ are the maximum Rabi field and resonance offset, respectively, and $\kappa = \omega_{1I}(T)/\omega_{1\max}$ is a truncation factor indicating the fractional amplitude of the RF

field at the end of the pulse. It is worth mentioning that other common standardized AFP pulse shapes, such as the tangent hyperbolic, Gaussian, and Lorentz waveforms also exist in the literature[1].

Although these pulses are adequate for less stringent practical conditions, optimization of the modulation functions is essential for adiabatic operations that are fast, high fidelity, and robust to the experimental imperfections of a specific setup. In the following section, we will provide a brief overview of some previously established methods for the numerical optimization of adiabatic operations.

1.5 Previous Work on Numerical Adiabatic Control

There have been various numerical techniques applied to the design of adiabatic quantum operations in the literature. In some works, the proposed method is formulated such that the adiabatic condition is enforced without direct knowledge of the Hamiltonian's spectrum, either indirectly, by penalizing fast control variations [51], or by using a temporally local probe for adiabaticity [52]. There has also been a time-optimal variational approach utilizing concepts from differential geometry [53]. More recently, progress has been made on the numerical design of so-called superadiabatic operations [54], where the controls are engineered such that the adiabatic condition can hold in a frame different from the original frame of reference [55]. In the context of NMR, the magnetization follows the effective field in this *superadiabatic frame*, instead of the original one.

A gradient-based optimization protocol, such as the one presented here, has also been devised for adiabatic control [56]; with the differing factor in our work being the use of the Van Loan auxiliary matrix formalism for facilitating the calculation of the adiabaticity metric, as well as allowing for the efficient inclusion of robustness against various perturbations directly in the optimization. This ability to directly account for perturbations, which is also absent from the other aforementioned schemes, renders our protocol a unique tool for engineering adiabatic operations in cases where the intrinsic robustness due to adiabaticity may be insufficient, e.g. because of stringent requirements on the control duration.

We have thus far reviewed the necessary background for this thesis, including an overview of time dependent perturbation theory, the adiabatic theorem, and its application to magnetic resonance. These will be utilized in the subsequent chapter to lay the theoretical foundations of our adiabatic control method.

[1] See table 1 in [45] for a list and comparison.

Chapter 2

Theoretical Description of the Control Search Protocol

In this chapter, we develop the theory behind the adiabatic control protocol for a general two-level system. First, we present the statement of the adiabatic control problem, followed by defining the metrics required to quantify the performance of an adiabatic operation. In particular, we describe an adiabaticity metric that naturally fits into the Van Loan formalism of Section 1.3, allowing for the efficient calculation of the metric and its gradient.

We then turn to the methods used for enforcing robustness criteria in the control searches, including robustness against inhomogeneities and uncertainties in system parameters, as well as perturbations in the Hamiltonian such as spin-spin interactions. Additionally, an extension of the protocol is briefly discussed for a special case of a multi-level system; the adiabatic control of a spin $I > 1/2$ particle in magnetic resonance.

The rest of the chapter is devoted to some of the tools for utilizing our protocol for adiabatic pulse design in magnetic resonance. In particular, we discuss different ways of parametrizing adiabatic pulse shapes, and how constraints such as amplitude and bandwidth limitations can be accounted for in the optimization.

2.1 Setup of the Adiabatic Control Problem

Let $\mathcal{G}(\mathbf{x}, t)$ be the time-evolution generator for a two-level system[1], which depends on a set of *control parameters* $\mathbf{x} = (x_1, ..., x_N) \in \mathbb{R}^N$, that indicate the experimenter's ability

[1]For consistency with our discussion in Section 1.2, we formulate the protocol using the (anti-Hermitian) time-evolution generator $\mathcal{G} = -iH$ instead of the Hamiltonian H.

to control the dynamics of the system. These can be a particular parametrization of an electromagnetic waveform, such as a set of its piecewise constant amplitudes, which can be experimentally implemented on an arbitrary waveform generator. Any such generator can be written in the orthogonal basis of Pauli matrices $\{\frac{1}{2}\mathbb{1}, \frac{1}{2}\sigma_x, \frac{1}{2}\sigma_y, \frac{1}{2}\sigma_z\}$ as

$$\mathcal{G}(\mathbf{x}, t) = \frac{i}{2}\Big(b_0(\mathbf{x}, t)\mathbb{1} + \mathbf{b}(\mathbf{x}, t) \cdot \boldsymbol{\sigma}\Big), \tag{2.1}$$

where $\boldsymbol{\sigma} \equiv (\sigma_x, \sigma_y, \sigma_z)$, and $b_0 : \mathbb{R}^N \times [0, T] \to \mathbb{R}$ and $\mathbf{b} : \mathbb{R}^N \times [0, T] \to \mathbb{R}^3$ are real (and real vector)-valued functions, since $\mathcal{G}(\mathbf{x}, t)$ is anti-Hermitian. The explicit functional form of b_0 and $\mathbf{b}$ in this expansion depends on the particular system in question. For example, in the case of adiabatic pulses in magnetic resonance, $b_0(\mathbf{x}, t) \equiv 0$ and $\mathbf{b}(\mathbf{x}, t)$ is the effective field in the FM frame Hamiltonian of Eq.(1.28). In that case, the control parameters $\mathbf{x}$ can be a particular parametrization of the frequency and amplitude modulation functions. We will assume in this section that the functional relationship between b_0, $\mathbf{b}$ and the parameters $\mathbf{x}$ is known. A concrete discussion of what these mappings are in the context of magnetic resonance will be given in Section 2.8. We will also assume that b_0, $\mathbf{b}$, and hence the generator $\mathcal{G}$ are differentiable functions of $\mathbf{x}$, as is necessary for a gradient-based optimization algorithm.

The propagator generated by $\mathcal{G}$ at time t is given by Eq.(1.3), in other words

$$\mathcal{U}(\mathbf{x}, t) = \mathrm{Texp}\Big[\int_0^t dt' \mathcal{G}(\mathbf{x}, t')\Big]. \tag{2.2}$$

Before stating the adiabatic control problem, it is beneficial to first examine the general form of Eq.(2.1) in more detail. We observe that the eigenvalues of $\mathcal{G}(\mathbf{x}, t)$ are given by

$$\Lambda_\pm(\mathbf{x}, t) = \frac{i}{2} b_0(\mathbf{x}, t) \pm \frac{i}{2}|\mathbf{b}(\mathbf{x}, t)|. \tag{2.3}$$

This implies that as long as $\mathbf{b}(\mathbf{x}, t) \neq 0$ for all $t \in [0, T]$, which we will assume from now on, the spectrum of $\mathcal{G}(\mathbf{x}, t)$ is non-degenerate, as required by the adiabatic theorem.

The adiabatic control problem is now stated as follows. Given some initial state $|\psi_0\rangle$ and target state $|\psi_T\rangle$, what is the set of controls $\mathbf{x}_{\text{opt}}$ (if it exists), that:

1. Evolves $|\psi_0\rangle$ to $|\psi_T\rangle$ at time $t = T$, up to a constant phase.
2. Produces a state $|\psi(\mathbf{x}, t)\rangle$ that follows a specific instantaneous eigenstate of $\mathcal{G}(\mathbf{x}, t)$, up to an arbitrary phase, as closely as possible.

Naturally, condition (2) also immediately implies that $\mathbf{b}(\mathbf{x}_{\text{opt}}, 0)$ and $\mathbf{b}(\mathbf{x}_{\text{opt}}, T)$ are constrained such that $|\psi_0\rangle$ and $|\psi_T\rangle$ are eigenvectors of $\mathcal{G}(\mathbf{x}_{\text{opt}}, 0)$ and $\mathcal{G}(\mathbf{x}_{\text{opt}}, T)$, respectively.

It is worth noting that the $b_0\mathbb{1}$ term in $\mathcal{G}$ of Eq.(2.1) has no effect on the above conditions. More precisely, if the conditions are satisfied for a specific set of controls, they are also satisfied for the system described by $G\big(\mathbf{b}(\mathbf{x},t)\big) \equiv i\mathbf{b}(\mathbf{x},t)\cdot\boldsymbol{\sigma}/2$, and vice-versa. This is simply because the propagators $U(\mathbf{x},t) \equiv \text{Texp}\Big[\int_0^t dt' G\big(\mathbf{b}(\mathbf{x},t')\big)\Big]$ and $\mathcal{U}(\mathbf{x},t)$ are related by a phase

$$\mathcal{U}(\mathbf{x},t) = e^{\frac{i}{2}\int_0^t dt' b_0(\mathbf{x},t')} U(\mathbf{x},t). \tag{2.4}$$

Therefore, the states of the two systems $\mathcal{G}$ and G at any time are also related by the same phase factor, implying that conditions (1), (2) are also satisfied for G. With this in mind, without loss of generality, we will restrict our attention to generators of the form $G(\mathbf{b}) = i\mathbf{b}\cdot\boldsymbol{\sigma}/2$ from now on. The eigenvalues of this generator are then simply $\lambda_\pm(\mathbf{b}) = \pm i|\mathbf{b}|/2$.

The eigenvectors of the $G(\mathbf{b})$ are a special case of the FM-frame magnetic resonance Hamiltonian examined in Section 1.4.2 for spin $I = 1/2$. Using Eq.(1.32), along with the Wigner d-matrix values from Appendix C, the eigenvectors are

$$\begin{cases} |E_+(\mathbf{b})\rangle = \cos\dfrac{\vartheta}{2}\,|\uparrow\rangle + e^{i\psi}\sin\dfrac{\vartheta}{2}\,|\downarrow\rangle \\ |E_-(\mathbf{b})\rangle = \sin\dfrac{\vartheta}{2}\,|\uparrow\rangle - e^{i\psi}\cos\dfrac{\vartheta}{2}\,|\downarrow\rangle \end{cases}, \tag{2.5}$$

with ϑ, ψ being the polar and azimuthal angles of $\mathbf{b}$, respectively. These also obtain a simple geometric interpretation: they point along the $\pm\mathbf{b}/|\mathbf{b}|$ directions in the Bloch sphere representation. Therefore, condition (2) can be reformulated geometrically, by requiring that the instantaneous state follows $\pm\mathbf{b}/|\mathbf{b}|$ on the Bloch sphere throughout its evolution; with the $\pm$ sign chosen according to the initial state. In light of this, following NMR terminology, we will call $\mathbf{b}(\mathbf{x},t)$ the *effective field* from now on.

2.2 Overview of the Control Protocol

A schematic of our proposed adiabatic control protocol is depicted in Fig.(2.1). Consider an ensemble of two-level systems, represented by the set Γ, each with its own effective field $\mathbf{b}^{(\lambda)}(\mathbf{x},t)$ and consequently generator $G\big(\mathbf{b}^{(\lambda)}(\mathbf{x},t)\big) = i\mathbf{b}^{(\lambda)}(\mathbf{x},t)\cdot\boldsymbol{\sigma}/2$. For the sake of concreteness and without loss of generality, we will refer to these two-level systems as spins from now on. The ensemble Γ can either be a representative subset of spins that

experience inhomogeneities in the system parameters, such as Larmor and Rabi dispersion, or an abstract ensemble constructed to account for any uncertainties in system characterization. The protocol starts with a seed $\mathbf{x}_0$ for the control parameters that is chosen from a random distribution, and is then used to calculate the time evolution generators of the ensemble $G\big(\mathbf{b}^{(\lambda)}(\mathbf{x}_0, t)\big)$. For every element in the ensemble $\lambda \in \Gamma$, the generator $G(\mathbf{b}^{(\lambda)})$ is used to define an auxiliary matrix $L(\mathbf{b}^{(\lambda)})$, called the *Van Loan generator*, based on the block matrix method of Section 1.3. A numerical differential equation solver, such as a Runge-Kutta algorithm [57], is then used to calculate the time-ordered exponential of the auxiliary matrix, called the *Van Loan propagator* $V_t[\mathbf{b}^{(\lambda)}]$, from which we calculate metrics quantifying the performance of the controls in three aspects: the final state condition, adiabaticity, and robustness to a perturbation (if applicable). These metrics are then combined to define a final target function $\Phi(\mathbf{x})$ that is fed to a gradient ascent optimizer which searches the control landscape for the optimum adiabatic operation.

On the other hand, as we will show in future sections, the functional derivative of the metrics with respect to the effective field can also be calculated using the Van Loan propagator. This allows for the efficient calculation of the target function gradient $\boldsymbol{\nabla}\Phi(\mathbf{x})$, which is also provided to the optimizer for increased optimization speed.

In the following sections, we will first describe the details of the control protocol for a single-spin ensemble, without any robustness considerations. We then discuss how this can be extended to an arbitrary ensemble, along with the inclusion of perturbation Hamiltonians.

2.3 Metrics for Control Performance

In order to gauge the performance of any set of controls, metrics are needed to quantify how much the conditions (1) and (2) are satisfied. For (1), we use the final state fidelity function

$$\Phi_0(\mathbf{x}) \equiv |\langle\psi_T|U(\mathbf{x}, T)|\psi_0\rangle|^2. \tag{2.6}$$

Clearly, $0 \leq \Phi_0(\mathbf{x}) \leq 1$, with $\Phi_0(\mathbf{x}) = 1$ occurring if and only if $|\psi(\mathbf{x}, T)\rangle = U(\mathbf{x}, T)|\psi_0\rangle$ equals $|\psi_T\rangle$ up to an arbitrary phase.

For the adiabaticity metric, satisfying condition (2) ideally requires that the overlap between the state $|\psi(\mathbf{x}, t)\rangle = U(\mathbf{x}, t)|\psi_0\rangle$ and the instantaneous eigenstate $|E_\pm(\mathbf{b}(\mathbf{x}, t))\rangle$ is

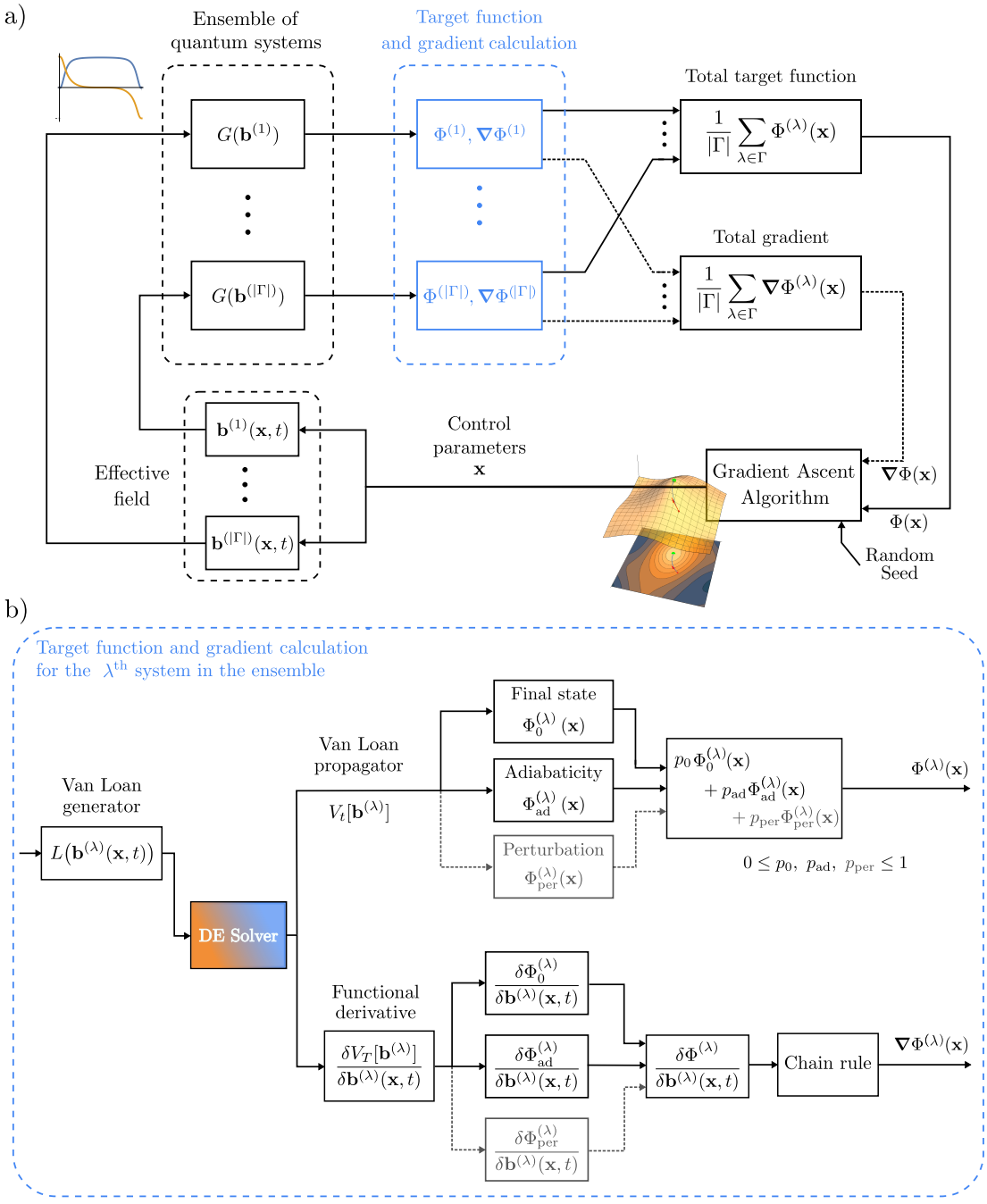

Figure 2.1: Schematic of the adiabatic control protocol. a) General overview of the optimization process. b) Target function value and gradient calculation using the Van Loan auxiliary matrix formalism.

one, for all $t \in [0, T]$. [1] We therefore define the adiabaticity metric as

$$\Phi_{\text{ad}}(\mathbf{x}) \equiv \frac{1}{T}\int_0^T dt \big|\big\langle E_{\pm}(\mathbf{b}(\mathbf{x},t))\big|U(\mathbf{x},t)\big|\psi_0\big\rangle\big|^2, \tag{2.7}$$

for which we have $0 \leq \Phi_{\text{ad}}(\mathbf{x}) \leq 1$, with $\Phi_{\text{ad}}(\mathbf{x}) = 1$ if and only if the state is equal to the instantaneous eigenstate throughout the evolution. The $\pm$ sign in Eq.(2.7) should be chosen such that the state at time t remains the same eigenstate that it was at $t = 0$.

To see how this metric fits into the Van Loan formalism, Eq.(2.7) can be rewritten as

$$\Phi_{\text{ad}}(\mathbf{x}) = \frac{1}{T}\langle\psi_0|\int_0^T dt\; U^{\dagger}(\mathbf{x},t)\;\big|E_{\pm}(\mathbf{b}(\mathbf{x},t))\big\rangle\big\langle E_{\pm}(\mathbf{b}(\mathbf{x},t))\big|\;U(\mathbf{x},t)\big|\psi_0\big\rangle, \tag{2.8}$$

or, using Eq.(1.10),

$$\Phi_{\text{ad}}(\mathbf{x}) = \frac{1}{T}\langle\psi_0|U^{\dagger}(\mathbf{x},T)\mathcal{D}_U(P;T)|\psi_0\rangle, \tag{2.9}$$

with $P_{\pm}(\mathbf{b}) \equiv |E_{\pm}(\mathbf{b})\rangle\langle E_{\pm}(\mathbf{b})|$ being the projectors onto the two eigenspaces of $G(\mathbf{b})$. The above Dyson term $\mathcal{D}_U(P;T)$ can clearly be evaluated using Eq.(1.19), rendering the Van Loan block matrix methods an efficient means of calculating $\Phi_{\text{ad}}(\mathbf{x})$. Furthermore, it can be shown that the above eigenprojector can be simplified to (see Appendix E)

$$P\big(\mathbf{b}(\mathbf{x},t)\big) = \frac{1}{2}\big(\mathbb{1} + \xi(\mathbf{x})\frac{\mathbf{b}(\mathbf{x},t)}{|\mathbf{b}(\mathbf{x},t)|}\cdot\boldsymbol{\sigma}\big), \tag{2.10}$$

with $\xi : \mathbb{R}^N \to \{-1, 1\}$ being a function that determines which eigenstate of $G(\mathbf{x},t)$ the system starts out on, i.e.

$$\xi(\mathbf{x}) \equiv \text{sgn}\Big[\text{Im}\big(\langle\psi_0|G(\mathbf{x},0)|\psi_0\rangle\big)\Big], \tag{2.11}$$

where sgn is the sign function defined as $\text{sgn}(x) = 1$ for $x \geq 0$ and $\text{sgn}(x) = -1$ for $x < 0$.

As an aside, it is worth mentioning that the presented adiabaticity metric can be shown to have a convenient geometric interpretation in terms of the angle $\alpha(\mathbf{x},t)$ between the effective field and the representation of the instantaneous state on the Bloch sphere, or equivalently, the magnetization in the context of NMR. This is (see Appendix F)

$$\Phi_{\text{ad}}(\mathbf{x}) = \frac{1}{2T}\int_0^T dt\big(1 + \cos\alpha(\mathbf{x},t)\big), \tag{2.12}$$

[1] Note that by the Cauchy-Schwarz inequality $0 \leq \big|\big\langle E_{\pm}\big(\mathbf{b}(\mathbf{x},t)\big)\big|\psi(\mathbf{x},t)\big\rangle\big| \leq 1$ for all $t \in [0, T]$.

i.e. the metric measures the normalized time-average of the cosine of the effective field-magnetization angle.

Combining both metrics of Eq.(2.6) and Eq.(2.9), the total target function for the adiabatic control problem is defined as

$$\Phi(\mathbf{x}) \equiv p\ \Phi_0(\mathbf{x}) + (1-p)\ \Phi_{\text{ad}}(\mathbf{x}), \tag{2.13}$$

with $0 \leq p \leq 1$ indicating the relative weight of the two targets in the optimization. We will address the choice of these weighting coefficients in the next chapter. The control problem thus boils down to finding the right set of controls $\mathbf{x}_{\text{opt}}$ that globally maximize the above target function.

Having discussed the appropriate metrics for evaluating control performance, we now turn to the problem of how to optimize Φ. Specifically, we will discuss the calculation of the target functions, as well as their derivatives, using the Van Loan auxiliary matrix formalism. These can then be used for the gradient ascent algorithm to find the optimum solution.

2.4 Evaluating Target Functions via Van Loan Relations

To efficiently calculate the integral in Eq.(2.9) for Φ_{ad}, we utilize the Van Loan formalism reviewed in Chapter 1. To this end, we define the *Van Loan generator* L as

$$L(\mathbf{b}) \equiv \begin{bmatrix} G(\mathbf{b}) & P(\mathbf{b}) \\ 0 & G(\mathbf{b}) \end{bmatrix}. \tag{2.14}$$

Utilizing the Van Loan relation Eq.(1.19), we have

$$\begin{aligned} V_t[\mathbf{b}] &\equiv \text{Texp}\Big[\int_0^t dt'\ L(\mathbf{b}(\mathbf{x},t'))\Big] \\ &= \begin{bmatrix} U(\mathbf{x},t) & \mathcal{D}_U(P;T) \\ 0 & U(\mathbf{x},t) \end{bmatrix}, \end{aligned} \tag{2.15}$$

with $V_t[\mathbf{b}]$ being the *Van Loan propagator*, which is a matrix-valued functional of the effective field $\mathbf{b}(\mathbf{x},t)$ for any specific set of controls $\mathbf{x}$. Comparing the upper right block

of Eq.(2.15) with the integral in Eq.(2.9), we can immediately write down the two target functions Φ_0 and Φ_{ad} as

$$\begin{cases} \Phi_0(\mathbf{x}) = |\langle\psi_T|V_T^{(11)}[\mathbf{b}]|\psi_0\rangle|^2 \\ \Phi_{\text{ad}}(\mathbf{x}) = \dfrac{1}{T}\langle\psi_0|V_T^{(11)}[\mathbf{b}]^\dagger\ V_T^{(12)}[\mathbf{b}]|\psi_0\rangle \end{cases}, \tag{2.16}$$

where $V_t^{(ij)}[\mathbf{b}]$ refers to block (i,j) in our block matrix representation of Eq.(2.15). The Van Loan generator can therefore be used to evaluate both target functions without the need to compute the complicated integral of Eq.(2.9) directly. To calculate $V_t[\mathbf{b}]$ from $L(\mathbf{b})$, by the definition of the time-ordered exponential, we need to solve the IVP

$$\begin{cases} \dfrac{\partial}{\partial t}V_t[\mathbf{b}] = L\big(\mathbf{b}(\mathbf{x},t)\big)V_t[\mathbf{b}] \\ V_0[\mathbf{b}] = \mathbb{1} \end{cases}. \tag{2.17}$$

This can either be done by dividing the interval $[0,T]$ into small sub-intervals, and multiplying the associated matrix exponentials, or by using a numerical differential equation solver; the latter of which is the method used in this work.

2.5 Target Function Gradient Calculation

Access to the derivatives of the target function with respect to the control parameters is essential for the computational efficiency of the optimization. The most non-trivial step in determining the target function gradient is computing the variation of the Van Loan propagator due to changes in the effective field; i.e. the functional derivative [58] of $V_T[\mathbf{b}]$ with respect to the three components of $\mathbf{b}(\mathbf{x},t_0)$ at some time t_0,

$$\frac{\delta V_T[\mathbf{b}]}{\delta b_i(\mathbf{x},t_0)} \equiv \frac{\partial}{\partial\epsilon}\Big|_{\epsilon=0} V_T\Big[\mathbf{b}(\mathbf{x},t) + \epsilon\delta(t-t_0)\hat{\mathbf{e}}_i\Big] \qquad i\in\{x,y,z\}, \tag{2.18}$$

where $\hat{\mathbf{e}}_i$ is the unit vector in the i^{th} direction.

Since the Van Loan generator and propagator are related by the IVP Eq.(2.17), we can use the results of Section 1.2 for the directional derivatives of a time-ordered exponential.

In particular, we can use Eq.(1.12) to write[1]

$$\begin{aligned}
\frac{\delta}{\delta b_i(\mathbf{x},t_0)}V_T[\mathbf{b}] &= \frac{\partial}{\partial\epsilon}\Big|_{\epsilon=0} V_T\Big[\mathbf{b}(\mathbf{x},t)+\epsilon\delta(t-t_0)\hat{\mathbf{e}}_i\Big] \\
&= \frac{\partial}{\partial\epsilon}\Big|_{\epsilon=0} \mathrm{Texp}\Big[\int_0^T dt\ L\Big(\mathbf{b}(\mathbf{x},t)+\epsilon\delta(t-t_0)\hat{\mathbf{e}}_i\Big)\Big] \\
&= \frac{\partial}{\partial\epsilon}\Big|_{\epsilon=0} \mathrm{Texp}\Big[\int_0^T dt\big[\ L\big(\mathbf{b}(\mathbf{x},t)\big)+\epsilon\delta(t-t_0)\frac{\partial L(\mathbf{b})}{\partial b_i}\hat{\mathbf{e}}_i+\mathrm{O}(\epsilon^2)\big]\Big] \\
&= V_T[\mathbf{b}]\int_0^T dt\ V_t^{-1}[\mathbf{b}]\ \delta(t-t_0)\frac{\partial L(\mathbf{b})}{\partial b_i}\ V_t[\mathbf{b}] \\
&= V_T[\mathbf{b}]\ V_{t_0}^{-1}[\mathbf{b}]\ \frac{\partial L(\mathbf{b})}{\partial b_i}\ V_{t_0}[\mathbf{b}],
\end{aligned} \tag{2.19}$$

or using the notation $\frac{\delta}{\delta\mathbf{b}} \equiv (\frac{\delta}{\delta b_x}, \frac{\delta}{\delta b_y}, \frac{\delta}{\delta b_z})$ and changing $t_0 \to t$ for simplicity,

$$\frac{\delta}{\delta\mathbf{b}(\mathbf{x},t)}V_T[\mathbf{b}] = V_T[\mathbf{b}]\ V_t^{-1}[\mathbf{b}]\ \boldsymbol{\nabla}_{\boldsymbol{b}}L(\mathbf{b})\ V_t[\mathbf{b}]. \tag{2.20}$$

The above expression requires the values of $V_t[\mathbf{b}]$, which have already been calculated from the IVP Eq.(2.17) to determine the control metrics. The components of the generator gradient $\boldsymbol{\nabla}_{\boldsymbol{b}}L(\mathbf{b})$ can be analytically calculated as

$$\begin{aligned}
\frac{\partial L(\mathbf{b})}{b_k} &= \begin{bmatrix} \dfrac{\partial G(\mathbf{b})}{b_k} & \dfrac{\partial P(\mathbf{b})}{b_k} \\ 0 & \dfrac{\partial G(\mathbf{b})}{b_k} \end{bmatrix} \\
&= \frac{1}{2}\begin{bmatrix} i\sigma_k & \dfrac{1}{|\mathbf{b}|}\sigma_k - \dfrac{b_k}{|\mathbf{b}|^3}\mathbf{b}\cdot\boldsymbol{\sigma} \\ 0 & i\sigma_k \end{bmatrix},
\end{aligned} \tag{2.21}$$

where $\partial P(\mathbf{b})/\partial b_k$ was calculated using Eq.(2.10). The only quantity left in Eq.(2.20) for calculating the functional derivative is the inverse of the Van Loan propagator $V_t^{-1}[\mathbf{b}]$, which can be analytically calculated due to its block triangular structure. The result is (see Appendix G)

$$V_t^{-1}[\mathbf{b}] = \begin{bmatrix} V_t^{(11)}[\mathbf{b}]^\dagger & -V_t^{(11)}[\mathbf{b}]^\dagger\ V_t^{(12)}[\mathbf{b}]\ V_t^{(11)}[\mathbf{b}]^\dagger \\ 0 & V_t^{(11)}[\mathbf{b}]^\dagger \end{bmatrix}. \tag{2.22}$$

[1]The following is a generalization of the propagator functional derivative derived in [59, 60].

Hence, $V_t^{-1}[\mathbf{b}]$ can be directly calculated from $V_t[\mathbf{b}]$ itself, without any need numerical matrix inversions.

Knowing how the Van Loan propagator varies with the effective field, the functional derivative of the two control metrics Φ_0, Φ_{ad} can now be calculated using Eq.(2.16) and the chain rule.

$$\begin{cases} \dfrac{\delta \Phi_0}{\delta \mathbf{b}(\mathbf{x},t)} = 2\ \mathrm{Re}\Big[\ \langle\psi_T|V_T^{(11)}[\mathbf{b}]|\psi_0\rangle\ \langle\psi_T|\dfrac{\delta V_T^{(11)}[\mathbf{b}]}{\delta \mathbf{b}(\mathbf{x},t)}|\psi_0\rangle\ \Big] \\ \dfrac{\delta \Phi_{\text{ad}}}{\delta \mathbf{b}(\mathbf{x},t)} = \dfrac{1}{T}\langle\psi_0|\Big[\Big(\dfrac{\delta V_T^{(11)}[\mathbf{b}]}{\delta \mathbf{b}(\mathbf{x},t)}\Big)^\dagger\ V_T^{(12)}[\mathbf{b}] + V_T^{(11)}[\mathbf{b}]^\dagger\ \Big(\dfrac{\delta V_T^{(12)}[\mathbf{b}]}{\delta \mathbf{b}(\mathbf{x},t)}\Big)\Big]|\psi_0\rangle \end{cases} . \tag{2.23}$$

The total target function derivative is then simply

$$\frac{\delta \Phi}{\delta \mathbf{b}(\mathbf{x},t)} = p\ \frac{\delta \Phi_0}{\delta \mathbf{b}(\mathbf{x},t)} + (1-p)\ \frac{\delta \Phi_{\text{ad}}}{\delta \mathbf{b}(\mathbf{x},t)}. \tag{2.24}$$

The gradient of the target function with respect to the control parameters $\mathbf{x}$ is now evaluated using the continuum analog of the chain rule

$$\boldsymbol{\nabla}\Phi(\mathbf{x}) = \int_0^T dt\ \frac{\delta \Phi}{\delta \mathbf{b}(\mathbf{x},t)} \cdot \frac{\partial \mathbf{b}(\mathbf{x},t)}{\partial \mathbf{x}}, \tag{2.25}$$

with $\partial \mathbf{b}(\mathbf{x},t)/\partial \mathbf{x}$ being the $3 \times N$ Jacobian matrix of the effective field, which depends on the particular set of control knobs available to the experimenter, as well as the way they couple into the system Hamiltonian. In the case of electromagnetic waveforms, such as in magnetic resonance, it also depends on the particular ansatz used to parametrize the pulse shapes.

For calculating the integral in Eq.(2.25), we note that for the effectiveness of the gradient-ascent optimization, numerical precision in the calculation of the gradient is not very crucial; just an estimate of the gradient's direction and value at each point $\mathbf{x}$ provides sufficient information to the optimizer about the behavior of Φ in the immediate neighborhood of $\mathbf{x}$ in the parameter space. With that in mind, the above integral can simply be approximated by a finite sum to speedup the computations.

Having developed the core procedure for the control searches, the next section will discuss how various robustness criteria can be perturbatively included in the optimization.

2.6 Including Robustness Criteria in the Optimization

The robustness of adiabatic operations is one of the key aspects that makes them such versatile tools in various fields of physics. As discussed in the previous chapter, adiabatic evolution can be susceptible to errors in the intermediate regime where the control fluctuations are neither too slow to respect adiabaticity, nor much faster than the system's characteristic response time. Additionally, in cases where very fast adiabatic operations are required, the inherent robustness due to adiabaticity may not be sufficient for some particular applications. It is in these situations that the ability to include explicit robustness requirements can be a valuable tool for adding flexibility to the design of adiabatic operations. In this section, we describe the method used in combination with our adiabatic control protocol in order to efficiently enforce such robustness in the optimization.

2.6.1 Against Inhomogeneities and Uncertainties

We now present how inhomogeneities in the parameters of the Hamiltonian can be addressed for an ensemble of spins. This also applies to cases where there are uncertainties in the characterization of the Hamiltonian, and the controls would need to be optimized for a range of parameters to ensure satisfactory performance. The idea is essentially doing the control searches for an ensemble of spins Γ, with the generator of the spin $\lambda \in \Gamma$ being

$$G\big(\mathbf{b}^{(\lambda)}(\mathbf{x},t)\big) = \frac{i}{2}\mathbf{b}^{(\lambda)}(\mathbf{x},t)\cdot\boldsymbol{\sigma}. \tag{2.26}$$

The ensemble Γ is a representative subset of the range of parameters needed to address the inhomogeneity, or it represents the uncertainty in the knowledge of the parameters in a single-spin Hamiltonian.

For any spin λ in the ensemble, all steps of sections 2.3 to 2.5 can be carried out to define and calculate the target functions $\Phi_0^{(\lambda)}(\mathbf{x})$, $\Phi_{\text{ad}}^{(\lambda)}(\mathbf{x})$ and their derivatives. We can then define a compound target function for the whole ensemble as

$$\Phi(\mathbf{x}) \equiv \frac{1}{|\Gamma|}\sum_{\lambda\in\Gamma}\Big[p^{(\lambda)}\Phi_0^{(\lambda)}(\mathbf{x}) + (1-p^{(\lambda)})\Phi_{\text{ad}}^{(\lambda)}(\mathbf{x})\Big], \tag{2.27}$$

with $|\Gamma|$ being the total number of spins in the ensemble. The optimization can now be carried out as before. The calculation for different members of the ensemble can be parallelized on a multi-core processor for a significant speedup in the computations.

2.6.2 Against Perturbations in the Hamiltonian

Consider the case where we wish to build robustness against some perturbation Hamiltonian (or equivalently generator) in the control searches. This could be a single-spin perturbation, or an unwanted many-body interaction between the spins in an ensemble. The idea behind our treatment of these perturbations is essentially the one developed in [17]; we construct an additional metric based on the the leading order perturbative correction to the final state, and combine it with our previous metrics to minimize the effect of the perturbation. Similar to the previous control metrics, the new perturbation metric will also be evaluated through defining an auxiliary matrix and utilizing a Van Loan relation.

We will restrict our discussion of the perturbative treatment to single and two-body perturbations. Generalization to arbitrary many-body perturbations is, however, straightforward.

Single-Body Perturbation

Let $\delta G(t) \in \mathcal{L}(\mathcal{H})$ be the unwanted perturbation we require robustness against. Assuming $\|\delta G(t)\| \ll \|G\big(\mathbf{b}(\mathbf{x},t)\big)\|$, the first order correction to the final propagator in the Dyson series of Eq.(1.11)[1] is given by

$$\mathcal{D}_U(\delta G;T) = U(\mathbf{x},T)\int_0^T dt\ U^\dagger(\mathbf{x},t)\delta G(t)U(\mathbf{x},t). \tag{2.28}$$

Therefore, the correction to the final state is $|\delta\psi(\mathbf{x},T)\rangle = \mathcal{D}_U(\delta G;T)|\psi_0\rangle$. We now define an additional metric based on the norm of $|\delta\psi(\mathbf{x},T)\rangle$, and combine it with the previous final state and adiabaticity metrics. In light of this, consider the norm

$$\big\||\delta\psi(\mathbf{x},T)\rangle\big\|^2 = \langle\psi_0|\mathcal{D}_U^\dagger(\delta G;T)\mathcal{D}_U(\delta G;T)|\psi_0\rangle, \tag{2.29}$$

which has an upper bound (see Appendix H)

$$\big\||\delta\psi(\mathbf{x},T)\rangle\big\|^2 \leq \Big(\int_0^T dt\ \big|\lambda_{\max}\big(\delta G(t)\big)\big|\Big)^2, \tag{2.30}$$

with $\lambda_{\max}(\delta G)$ being the largest (magnitude) eigenvalue of δG. A suitably normalized perturbation metric can therefore be constructed as

$$\Phi_{\text{per}}(\mathbf{x}) \equiv 1 - \frac{1}{\mathcal{N}}\langle\psi_0|\mathcal{D}_U^\dagger(\delta G;T)\mathcal{D}_U(\delta G;T)|\psi_0\rangle, \tag{2.31}$$

[1]This is equivalent to the zeroth-order average Hamiltonian due to δG [24].

with $\mathcal{N} = \big(\int_0^T dt\ \big|\lambda_{\max}\big(\delta G(t)\big)\big|\big)^2$ being the normalization integral, which, depending on the specific functional form of $\delta G(t)$, can either be analytically or numerically calculated before the optimization. In the special case of time-independent perturbations, such as the dipolar coupling discussed in Chapter 3, the normalization integral simply reduces to $\mathcal{N} = T^2|\lambda_{\max}(\delta G)|^2$. Note that $0 \leq \Phi_{\text{per}}(\mathbf{x}) \leq 1$ with $\Phi_{\text{per}}(\mathbf{x}) = 1$ if and only if $|\delta\psi(\mathbf{x}, T)\rangle = 0$, as expected. This can now be combined with the other metrics similar to Eq.(2.13), in other words

$$\Phi(\mathbf{x}) \equiv p_0\Phi_0(\mathbf{x}) + p_{\text{ad}}\Phi_{\text{ad}}(\mathbf{x}) + p_{\text{per}}\Phi_{\text{per}}(\mathbf{x}), \tag{2.32}$$

with the relative weights satisfying $p_0 + p_{\text{ad}} + p_{\text{per}} = 1$ and $p_0, p_{\text{ad}}, p_{\text{per}} \in [0, 1]$.

To calculate $\Phi_{\text{per}}(\mathbf{x})$, we can define the Van Loan generator

$$L(\mathbf{b}, t) \equiv \begin{bmatrix} G(\mathbf{b}) & P(\mathbf{b}) & 0 \\ 0 & G(\mathbf{b}) & \delta G(t) \\ 0 & 0 & G(\mathbf{b}) \end{bmatrix}, \tag{2.33}$$

with the corresponding Van Loan propagator $V_t[\mathbf{b}] \equiv \text{Texp}\big[\int_0^t dt' L\big(\mathbf{b}(\mathbf{x}, t'), t'\big)\big]$ being

$$V_t[\mathbf{b}] = \begin{bmatrix} U(\mathbf{x}, t) & \mathcal{D}_U(P; t) & \mathcal{D}_U\big(P, \delta G; t\big) \\ 0 & U(\mathbf{x}, t) & \mathcal{D}_U(\delta G; t) \\ 0 & 0 & U(\mathbf{x}, t) \end{bmatrix}. \tag{2.34}$$

Hence, the perturbation metric is

$$\Phi_{\text{per}}(\mathbf{x}) = 1 - \frac{1}{\mathcal{N}}\langle\psi_0|\ V_T^{(23)}[\mathbf{b}]^\dagger\ V_T^{(23)}[\mathbf{b}]\ |\psi_0\rangle, \tag{2.35}$$

while the other metrics still obey Eq.(2.16).

For the gradient calculation, the functional derivative of the Van Loan Propagator still obeys Eq.(2.20), with the matrix inverse $V_t^{-1}[\mathbf{b}]$ given by

$$V_t^{-1}[\mathbf{b}] = \begin{bmatrix} V_t^{(11)}[\mathbf{b}]^\dagger & -V_t^{(11)}[\mathbf{b}]^\dagger\ V_t^{(12)}[\mathbf{b}]\ V_t^{(11)}[\mathbf{b}]^\dagger & V_t^{(11)}[\mathbf{b}]^\dagger\ V_t^{(12)}[\mathbf{b}]\ V_t^{(11)}[\mathbf{b}]^\dagger\ V_t^{(23)}[\mathbf{b}]\ V_t^{(11)}[\mathbf{b}]^\dagger \\ 0 & V_t^{(11)}[\mathbf{b}]^\dagger & -V_t^{(11)}[\mathbf{b}]^\dagger\ V_t^{(23)}[\mathbf{b}]\ V_t^{(11)}[\mathbf{b}]^\dagger \\ 0 & 0 & V_t^{(11)}[\mathbf{b}]^\dagger \end{bmatrix}, \tag{2.36}$$

which was derived using the method outlined in Appendix G. The functional derivative of the perturbation metric is now evaluated using Eq.(2.35) and the chain rule,

$$\frac{\delta\Phi_{\text{per}}}{\delta\mathbf{b}(\mathbf{x},t)} = -\frac{1}{\mathcal{N}}\langle\psi_0|\Big[\Big(\frac{\delta V_T^{(23)}[\mathbf{b}]}{\delta\mathbf{b}(\mathbf{x},t)}\Big)^\dagger\ V_T^{(23)}[\mathbf{b}] + V_T^{(23)}[\mathbf{b}]^\dagger\ \Big(\frac{\delta V_T^{(23)}[\mathbf{b}]}{\delta\mathbf{b}(\mathbf{x},t)}\Big)\Big]|\psi_0\rangle. \tag{2.37}$$

This can then be combined with the gradient of the other metrics using Eq.(2.32) and the chain rule integral Eq.(2.25), to compute the gradient of the total target function.

Two-Body Perturbation

The same method can be utilized for a many-body perturbation such as spin-spin interactions. For example, robustness against a two-body perturbation $\delta G(t) \in \mathcal{L}(\mathcal{H}\otimes\mathcal{H})$ would require minimizing $\|\mathcal{D}_{U\otimes U}(\delta G;T)|\psi_0\rangle^{\otimes 2}\|$, which, similar to Eq.(2.31), can be done by maximizing the metric

$$\Phi_{\text{per}}(\mathbf{x}) \equiv 1 - \frac{1}{\mathcal{N}}\langle\psi_0|^{\otimes 2}\ \mathcal{D}^\dagger_{U\otimes U}(\delta G;T)\mathcal{D}_{U\otimes U}(\delta G;T)\ |\psi_0\rangle^{\otimes 2}, \tag{2.38}$$

which is calculated by constructing the following Van Loan generator using a direct sum.

$$L(\mathbf{b},t) \equiv \begin{bmatrix} G(\mathbf{b}) & P(\mathbf{b}) \\ 0 & G(\mathbf{b}) \end{bmatrix} \oplus \begin{bmatrix} G_2(\mathbf{b}) & \delta G(t) \\ 0 & G_2(\mathbf{b}) \end{bmatrix} \tag{2.39}$$

$$= \begin{bmatrix} G(\mathbf{b}) & P(\mathbf{b}) & 0 & 0 \\ 0 & G(\mathbf{b}) & 0 & 0 \\ 0 & 0 & G_2(\mathbf{b}) & \delta G(t) \\ 0 & 0 & 0 & G_2(\mathbf{b}) \end{bmatrix}, \tag{2.40}$$

where $G_2(\mathbf{b}) \equiv G(\mathbf{b})\otimes\mathbb{1} + \mathbb{1}\otimes G(\mathbf{b})$. The associated Van Loan propagator is

$$V_t[\mathbf{b}] = \begin{bmatrix} U(\mathbf{x},t) & \mathcal{D}_U(P;t) & 0 & 0 \\ 0 & U(\mathbf{x},t) & 0 & 0 \\ 0 & 0 & U^{\otimes 2}(\mathbf{x},t) & \mathcal{D}_{U\otimes U}(\delta G;t) \\ 0 & 0 & 0 & U^{\otimes 2}(\mathbf{x},t) \end{bmatrix}. \tag{2.41}$$

This is due to the fact that time-ordered exponentials respect the direct sum operation, in the sense that for any A and B,

$$\mathrm{Texp}\Big[\int_0^t dt' A(t') \oplus B(t')\Big] = \mathrm{Texp}\Big[\int_0^t dt' A(t')\Big] \oplus \mathrm{Texp}\Big[\int_0^t dt' B(t')\Big], \tag{2.42}$$

which can easily be derived by writing the defining IVP Eq.(1.2) for A and B, and showing that the direct sum of their solutions satisfies a similar IVP with $A(t) \oplus B(t)$ as the generator.

With that in mind, the perturbation metric Eq.(2.38) can be evaluated using the $(3,4)$ block of $V_T[\mathbf{b}]$, similar to Eq.(2.35). The gradient calculation also follows the exact same steps, with the exception of the inverse $V_t^{-1}[\mathbf{b}]$, which may be determined using the fact that the inverse of a direct sum is the direct sum of the inverses (see Appendix G).

Note that in the case of having more than one perturbation, several perturbation metrics can be similarly constructed and combined for the optimization, with a larger Van Loan generator facilitating their calculation. Our method can also be extended to general M-body perturbation terms by using the same direct sum treatment on an M-spin Hilbert space, as opposed to the 2-spin generator used in Eq.(2.39).

We here conclude our theoretical discussion of the adiabatic control protocol for two-level systems. The next section is devoted to a brief overview of how the protocol can be extended to some special multi-level systems, including the adiabatic control of spin $I > 1/2$ particles for magnetic resonance.

2.7 Generalization to Multi-Level Systems: An Example

Thus far we have described the theoretical underpinnings of the adiabatic control protocol for a two-level system. To extend this to a multi-level system, observe that our definition of the adiabaticity and final state metrics Eq.(2.6, 2.7), as well as the required Van Loan generator Eq.(2.14), are also applicable to a multi-level system, provided that the eigenprojection operators $P_m = |E_m\rangle\langle E_m|$ are exactly known as a function of time and the controls. In other words, a generalization to any multi-level system would require exact knowledge of the eigenstate structure of its Hamiltonian.

An important example of such a problem is the adiabatic control of a general spin I particle in a magnetic resonance setting, for which the energy eigenstates were derived in

Section 1.4.2. In this case, the system generator in the FM frame, as a function of the effective field $\mathbf{b}(\mathbf{x},t)$, is Eq.(1.28),

$$G\big(\mathbf{b}(\mathbf{x},t)\big) = i\mathbf{b}(\mathbf{x},t)\cdot\mathbf{I}. \tag{2.43}$$

We note that Eq.(2.43) is written with the assumption that the spin does not experience quadrupolar coupling due to an electric field gradient [46], which is possible in cases where it is suppressed due to the crystal symmetries of the sample. This treatment is also applicable to systems with a small quadrupolar coupling relative to the effective field, such that it can be incorporated using the perturbative method of Section 2.6.2.

The adiabaticity metric we construct in this case is essentially the same as before; it is the time-average of the overlap between the specific instantaneous eigenstate the system started in, and the evolved state. In other words,

$$\Phi_{\text{ad}}(\mathbf{x}) \equiv \frac{1}{T}\int_0^T dt\big|\big\langle E_m(\mathbf{b}(\mathbf{x},t))\big|U(\mathbf{x},t)\big|\psi_0\big\rangle\big|^2, \tag{2.44}$$

with$|\psi_0\rangle$ being the initial state, and m being chosen such that $|\psi_0\rangle \propto |E_m(\mathbf{b}(\mathbf{x},0))\rangle$. Similar to our treatment of the two-level system, this can be rewritten in terms of the eigenprojection operator $P_m(\mathbf{b}) \equiv |E_m(\mathbf{b})\rangle\langle E_m(\mathbf{b})|$ as

$$\Phi_{\text{ad}}(\mathbf{x}) = \frac{1}{T}\langle\psi_0|U^\dagger(\mathbf{x},T)\mathcal{D}_U(P_m;T)|\psi_0\rangle, \tag{2.45}$$

which can be calculated with a Van Loan generator of the exact same form as Eq.(2.14). Gradient calculations also follow the exact same method; calculating functional derivatives of the Van Loan propagator with Eq.(2.20), the functional derivatives of the metrics with Eq.(2.23), and finally, the gradient of the target function with the chain rule of Eq.(2.25).

The eigenprojector $P_m(\mathbf{b})$ itself can be calculated using the eigenstates of the FM frame Hamiltonian Eq.(1.32). The m^{th} eigenprojector is

$$\begin{aligned} P_m(\mathbf{b}) &= |E_m(\mathbf{b})\rangle\langle E_m(\mathbf{b})| &(2.46)\\ &= \sum_{m_1=-I}^{I}\sum_{m_2=-I}^{I} e^{-i(m_1-m_2)\psi}\, d^{(I)}_{m_1,m}(\vartheta)\Big(d^{(I)}_{m_2,m}(\vartheta)\Big)^*\, |m_1\rangle\langle m_2|, &(2.47)\end{aligned}$$

where the polar and azimuthal angles $\vartheta,\ \psi$ are

$$\begin{cases} \vartheta = \cos^{-1}\left(\dfrac{b_z}{|\mathbf{b}|}\right) \\ \psi = \cos^{-1}\left(\dfrac{b_x}{\sqrt{b_x^2+b_y^2}}\right) \end{cases}. \tag{2.48}$$

As can be seen from Eq.(2.20, 2.21), the functional derivative of the Van Loan propagator requires $\partial P_m(\mathbf{b})/\partial b_k$ for $k \in \{x, y, z\}$. This can simply be calculated using the chain rule

$$\begin{aligned}\frac{\partial P_m(\mathbf{b})}{\partial b_k} &= \frac{\partial \vartheta}{\partial b_k}\frac{\partial P_m(\mathbf{b})}{\partial \vartheta} + \frac{\partial \psi}{\partial b_k}\frac{\partial P_m(\mathbf{b})}{\partial \psi} \\ &= \begin{cases} \dfrac{b_x b_z}{|\mathbf{b}|^2\sqrt{b_x^2+b_y^2}}\ \dfrac{\partial P_m(\mathbf{b})}{\partial \vartheta} - \dfrac{b_y}{b_x^2+b_y^2}\ \dfrac{\partial P_m(\mathbf{b})}{\partial \psi} & k = x \\ \dfrac{b_y b_z}{|\mathbf{b}|^2\sqrt{b_x^2+b_y^2}}\ \dfrac{\partial P_m(\mathbf{b})}{\partial \vartheta} + \dfrac{b_x b_y}{|b_y|(b_x^2+b_y^2)}\ \dfrac{\partial P_m(\mathbf{b})}{\partial \psi} & k = y\ . \\ -\dfrac{\sqrt{b_x^2+b_y^2}}{|\mathbf{b}|^2}\ \dfrac{\partial P_m(\mathbf{b})}{\partial \vartheta} & k = z \end{cases} \end{aligned} \tag{2.49}$$

Eq.(2.47, 2.48) can be used to construct the Van Loan generator Eq.(2.14), and hence derive the metrics and their derivatives for the optimization. We have thus generalized the control protocol to a special case of a multi-level system. As previously mentioned, this generalization can be applied to any multi-level Hamiltonian for which the eigenstates are exactly known as a function of control parameters and time.

So far we have discussed the adiabatic control protocol assuming that the dependence of the effective field $\mathbf{b}(\mathbf{x}, t)$ to the control parameters is known. Although this functional relationship depends on the particular system in question, in some cases, such as the design of adiabatic pulses in magnetic resonance, there is a freedom in the definition of the control parameters $\mathbf{x}$. In particular, their is a choice in the way the continuous pulse shapes can be parametrized in terms of a finite set of numbers. For example, they could be taken as piecewise constant waveforms, with the finite set of amplitudes acting as the optimization parameters. In the next section, we focus on the problem of designing adiabatic pulses for magnetic resonance, and present suitable pulse parametrizations, as well as a method to account for experimental constraints without the need for constrained optimization algorithms.

2.8 Adiabatic Operations for Magnetic Resonance

As explained in our review of NMR adiabatic operations (Section 1.4.2), an AFP can be performed in the FM frame, using an amplitude- and frequency-modulated pulse with in-phase and quadrature envelope functions $\omega_{1I}(t)$, $\omega_{1Q}(t)$, and instantaneous resonance offset $\Delta\omega(t)$. Assuming a spin 1/2 particle, the time-evolution generator in this frame is

$G\big(\mathbf{b}(t)\big) = i\mathbf{b}(t)\cdot\boldsymbol{\sigma}/2$, with $\mathbf{b}(t) = \big(\omega_{1I}(t),\ \omega_{1Q}(t),\ \Delta\omega(t)\big)$ being the effective field. The adiabatic control problem in this case then corresponds to finding the optimal envelope and resonance offset waveforms that maximize the target function discussed in Section 2.3.

In order to formulate the protocol in terms of a finite set of optimization parameters $\mathbf{x} \in \mathbb{R}^N$, we need to parametrize the above three waveforms using an ansatz suitable for the desired kind of operation. An educated choice for this parametrization can allow for a smaller number of unknowns in the optimization, and hence faster pulse searches.

2.8.1 Parametrization of Adiabatic Pulse Shapes

We here suggest two parametrizations of the effective field waveforms, one specifically for AFPs, and the other for operations connecting arbitrary points on the Bloch sphere. Both of these ansatz choices are polynomial functions, for which the built-in smoothness facilitates adiabatic evolution. This is in contrast to some other common parametrization schemes, such as piecewise constant amplitudes [56], which are discontinuous by nature and hence may not be favorable in terms of adiabaticity.

We will assume that there are no pulse amplitude and bandwidth limitations in this discussion. The problem of adding these constraints to the adiabatic pulses will be addressed in the subsequent section.

Ansatz for AFPs

For the adiabatic inversion pulses, we define the following polynomial functions:

$$\begin{cases} \mathcal{A}_m(\mathbf{x},t) \equiv \displaystyle\sum_{n=1}^{m} X_n\Big[1-\big(2\frac{t}{T}-1\big)^{2n}\Big] \\ \mathcal{B}_m(\mathbf{x},t) \equiv \displaystyle\sum_{n=m+1}^{N} X_n\Big(1-2\frac{t}{T}\Big)^{2(n-m)-1} \end{cases}. \tag{2.50}$$

Observe that $\mathcal{A}_m$ and $\mathcal{B}_m$ have even and odd symmetry around the middle of the pulse $t = T/2$, respectively.

Our AFP ansatz for the effective field is (ansatz I)

$$\mathbf{a}^{(\mathrm{I})}(\mathbf{x},t) \equiv \big(\mathcal{A}_m(\mathbf{x},t),\ 0,\ \mathcal{B}_m(\mathbf{x},t)\big), \tag{2.51}$$

with m determining the number of optimization parameters in each individual waveform. It can be seen that for any $\mathbf{x} \in \mathbb{R}^N$, Eq.(2.50) forces the effective field to start from the $\pm\hat{\mathbf{z}}$ direction[1] , go through the $\hat{\mathbf{x}}$ direction at $t = T/2$, and point along $\mp\hat{\mathbf{z}}$ at the end of the pulse; rendering it an appropriate choice for the design of AFPs.

The derivatives of Eq.(2.50) will also be needed for calculating the target function gradient Eq.(2.25). These are

$$\begin{cases} \boldsymbol{\nabla}\mathcal{A}_m(\mathbf{x},t) \equiv \sum_{n=1}^{m} \hat{\mathbf{e}}_n \Big[1 - \big(2\frac{t}{T} - 1\big)^{2n}\Big] \\ \boldsymbol{\nabla}\mathcal{B}_m(\mathbf{x},t) \equiv \sum_{n=m+1}^{N} \hat{\mathbf{e}}_n \Big(1 - 2\frac{t}{T}\Big)^{2(n-m)-1} \end{cases}, \tag{2.52}$$

with $\hat{\mathbf{e}}_n$ being the unit vector in the n^{th} direction in $\mathbb{R}^N$. The Jacobian $\partial\mathbf{a}^{(\mathrm{I})}(\mathbf{x},t)/\partial\mathbf{x}$ then is

$$\frac{\partial}{\partial\mathbf{x}}\mathbf{a}^{(\mathrm{I})}(\mathbf{x},t) = \begin{bmatrix} \boldsymbol{\nabla}\mathcal{A}_m(\mathbf{x},t) \\ 0 \\ \boldsymbol{\nabla}\mathcal{B}_m(\mathbf{x},t) \end{bmatrix} \tag{2.53}$$

Ansatz for General Operations

With ansatz I being specifically tailored for AFPs, a more general parametrization is needed for operations connecting arbitrary states. To this end, we need a polynomial function that connects the arbitrary points $(0,a)$ and (T,a'). One solution is to use the line connecting these two points, and add it to the most general polynomial with roots at $t \in \{0,T\}$. Therefore, we define the function

$$f^{aa'}_{mm'}(\mathbf{x},t) \equiv \frac{t}{T}(1-\frac{t}{T}) \sum_{n=m+1}^{m'} X_n \big(1 - 2\frac{t}{T}\big)^{n-m-1} + \frac{t}{T}(a'-a) + a, \tag{2.54}$$

with $a = f^{aa'}_{mm'}(\mathbf{x},0)$ and $a' = f^{aa'}_{mm'}(\mathbf{x},T)$. Denoting the Bloch sphere representation of the initial and final states by (α,β,γ) and (α',β',γ') respectively[2], an ansatz for engineering

[1] with the sign depending on $\sum_{n=m+1}^{N} X_n$.

[2] As explained in Section 2.1, for adiabatic evolution, the initial and final effective field directions are required to coincide with the Bloch sphere representation of the state at the corresponding times.

arbitrary operations can be constructed with the above function (ansatz II).

$$\mathbf{a}^{(\mathrm{II})}(\mathbf{x},t) \equiv \big(f_{0,N_x}^{\alpha\alpha'}(\mathbf{x},t),\ f_{N_x,N_x+N_y}^{\beta\beta'}(\mathbf{x},t),\ f_{N_x+N_y,N}^{\gamma\gamma'}(\mathbf{x},t)\big), \tag{2.55}$$

where $N_x,\ N_y,\ N-N_x-N_y$ are the number of optimization parameters given to each waveform.

The derivatives of ansatz II depend on $\boldsymbol{\nabla} f_{mm'}^{aa'}(\mathbf{x},t)$, for which the calculation is straightforward.

$$\boldsymbol{\nabla} f_{mm'}^{aa'}(\mathbf{x},t) = \frac{t}{T}(1-\frac{t}{T}) \sum_{n=m+1}^{m'} \hat{\mathbf{e}}_n \big(1-2\frac{t}{T}\big)^{n-m-1}. \tag{2.56}$$

This results in the following Jacobian:

$$\frac{\partial}{\partial \mathbf{x}} \mathbf{a}^{(\mathrm{II})}(\mathbf{x},t) = \begin{bmatrix} \boldsymbol{\nabla} f_{0,N_x}^{\alpha\alpha'}(\mathbf{x},t) \\ \boldsymbol{\nabla} f_{N_x,N_x+N_y}^{\beta\beta'}(\mathbf{x},t) \\ \boldsymbol{\nabla} f_{N_x+N_y,N}^{\gamma\gamma'}(\mathbf{x},t) \end{bmatrix}, \tag{2.57}$$

which can be used in the target function gradient calculation.

So far we have always assumed that there are no constraints on either pulse amplitudes, or the bandwidth, even though enforcing such experimental limitations is crucial for a pulse design protocol to be applicable to a practical setting. We will discuss how this can be implemented in the next section.

2.8.2 Implementing Constraints with Optimization Transfer Functions

To take constraints into account, we utilize an *optimization transfer function* [17], a map $\boldsymbol{\Xi} : \mathbb{R}^3 \to \mathbb{R}^3$, for which the range $\mathscr{R}(\boldsymbol{\Xi}) \subseteq \mathbb{R}^3$ is the set of effective fields satisfying the limitations in question. In other words, the restrictions can be enforced without the need for constrained optimization algorithms by setting the effective field to $\mathbf{b} \equiv \boldsymbol{\Xi}(\mathbf{a}) \in \mathscr{R}(\boldsymbol{\Xi})$, with $\mathbf{a}$ being an unconstrained ansatz from the previous section.

In the case of our adiabatic passages, we define two different optimization transfer functions depending on the ansatz chosen from the previous section. For ansatz I, we use the function

$$\boldsymbol{\Xi}_{\mathrm{I}}(\mathbf{a}) \equiv \Big(\omega_{1\max}\tanh(a_x),\ 0,\ \Delta\omega_{\max}\tanh(a_z)\Big). \tag{2.58}$$

And for ansatz II we define

$$\boldsymbol{\Xi}_{\mathrm{II}}(\mathbf{a}) \equiv \Big(\frac{\omega_{1\max}}{\sqrt{2}}\tanh(a_x),\ \frac{\omega_{1\max}}{\sqrt{2}}\tanh(a_y),\ \Delta\omega_{\max}\tanh(a_z)\Big), \tag{2.59}$$

where $\omega_{1\max}$ and $\Delta\omega_{\max}$ are the maximum Rabi strength and resonance offset, respectively. Note that limiting the resonance offset waveform effectively restricts the bandwidth of the pulse, which is roughly estimated as $2\Delta\omega_{\max}$. The tangent hyperbolic function in Eq.(2.58, 2.59) essentially acts as a soft clipping function, keeping the effective field inside the square $\mathscr{R}(\boldsymbol{\Xi}_{\mathrm{I}}) = \big(-\omega_{1\max},\ \omega_{1\max}\big) \times \{0\} \times \big(-\Delta\omega_{\max}, \Delta\omega_{\max}\big)$ for ansatz I, and the cube $\mathscr{R}(\boldsymbol{\Xi}_{\mathrm{II}}) = \big(-\omega_{1\max}/\sqrt{2},\ \omega_{1\max}/\sqrt{2}\big)^2 \times \big(-\Delta\omega_{\max}, \Delta\omega_{\max}\big)$, ensuring that the constraints are satisfied.

Note that the start and end points of ansatz II now require special attention, since they need to be chosen with $\boldsymbol{\Xi}_{\mathrm{II}}(\mathbf{a})$ in mind. Instead of setting the start and end points of the polynomial functions to $\mathbf{b}(0)$ and $\mathbf{b}(T)$, they need to be chosen such that the output of the optimization transfer function results in the correct initial and final effective field, i.e. $\boldsymbol{\Xi}_{\mathrm{II}}\big(\mathbf{a}(0)\big) = \mathbf{b}(0)$ and $\boldsymbol{\Xi}_{\mathrm{II}}\big(\mathbf{a}(T)\big) = \mathbf{b}(T)$. In the case of amplitude and bandwidth constraints, since the transfer function of Eq.(2.59) is invertible, we can use $\mathbf{a}(0) = \boldsymbol{\Xi}_{\mathrm{II}}^{-1}\big(\mathbf{b}(0)\big)$ and $\mathbf{a}(T) = \boldsymbol{\Xi}_{\mathrm{II}}^{-1}\big(\mathbf{b}(T)\big)$ as the boundary points of the polynomials, with $\boldsymbol{\Xi}_{\mathrm{II}}^{-1}(\mathbf{b})$ being

$$\boldsymbol{\Xi}_{\mathrm{II}}^{-1}(\mathbf{b}) = \Big(\frac{\sqrt{2}}{\omega_{1\max}}\tanh^{-1}(b_x),\ \frac{\sqrt{2}}{\omega_{1\max}}\tanh^{-1}(b_y),\ \frac{1}{\Delta\omega_{\max}}\tanh^{-1}(b_z)\Big). \tag{2.60}$$

This guarantees that the initial and final effective fields are locked to the direction of the spin magnetization, in the presence of the optimization transfer function.

For the gradient calculations, since the Jacobian matrix of the effective field $\partial\mathbf{b}(\mathbf{x},t)/\partial\mathbf{x}$ is required in the target function gradient Eq.(2.25), we use the chain rule to link it to the Jacobian of the ansatz $\partial\mathbf{a}(\mathbf{x},t)/\partial\mathbf{x}$ chosen in the previous section:

$$\underbrace{\frac{\partial\mathbf{b}(\mathbf{x},t)}{\partial\mathbf{x}}}_{3\times N} = \underbrace{\frac{\partial\boldsymbol{\Xi}\big(\mathbf{a}(\mathbf{x},t)\big)}{\partial\mathbf{a}}}_{3\times 3} \cdot \underbrace{\frac{\partial\mathbf{a}(\mathbf{x},t)}{\partial\mathbf{x}}}_{3\times N}, \tag{2.61}$$

where $\partial\mathbf{a}(\mathbf{x},t)/\partial\mathbf{x}$ is evaluated as discussed in Section 2.8.1. For the optimization transfer function of Eq.(2.58), the Jacobian $\partial\boldsymbol{\Xi}_{\mathrm{I}}(\mathbf{a})/\partial\mathbf{a}$ is

$$\frac{\partial\boldsymbol{\Xi}_{\mathrm{I}}(\mathbf{a})}{\partial\mathbf{a}} = \begin{bmatrix} \omega_{1\max}\ \mathrm{sech}^2(a_x) & 0 & 0 \\ 0 & 0 & 0 \\ 0 & 0 & \Delta\omega_{\max}\ \mathrm{sech}^2(a_z) \end{bmatrix}. \tag{2.62}$$

Similarly, the Jacobian for for Eq.(2.59) is

$$\frac{\partial \boldsymbol{\Xi}_{\mathrm{II}}(\mathbf{a})}{\partial \mathbf{a}} = \begin{bmatrix} \frac{\omega_{1\max}}{\sqrt{2}} \operatorname{sech}^2(a_x) & 0 & 0 \\ 0 & \frac{\omega_{1\max}}{\sqrt{2}} \operatorname{sech}^2(a_y) & 0 \\ 0 & 0 & \Delta\omega_{\max} \operatorname{sech}^2(a_z) \end{bmatrix}. \tag{2.63}$$

We thus use this additional piece in the protocol to design adiabatic operations subject to the limitations of an actual experimental setup. As depicted in Fig.(2.2), in cases where the optimization is done over an ensemble, an optimization transfer function $\boldsymbol{\Xi}^{(\lambda)}$ can be assigned to each member to impose its associated constraints. For instance, in a setup that contains Rabi dispersion, i.e. RF field inhomogeneities, $\boldsymbol{\Xi}^{(\lambda)}$ is set to Eq.(2.59), with $\omega_{1\max}^{(\lambda)} = \gamma B_{1\max}(\mathbf{r}^{(\lambda)})$ depending on the location of the λ^{th} member $\mathbf{r}^{(\lambda)}$, and the RF field distribution. The same principle applies to Larmor dispersion, for which $\Delta\omega_{\max}^{(\lambda)}$ depends on the spatial distribution of the static field, and hence the resonance frequency.

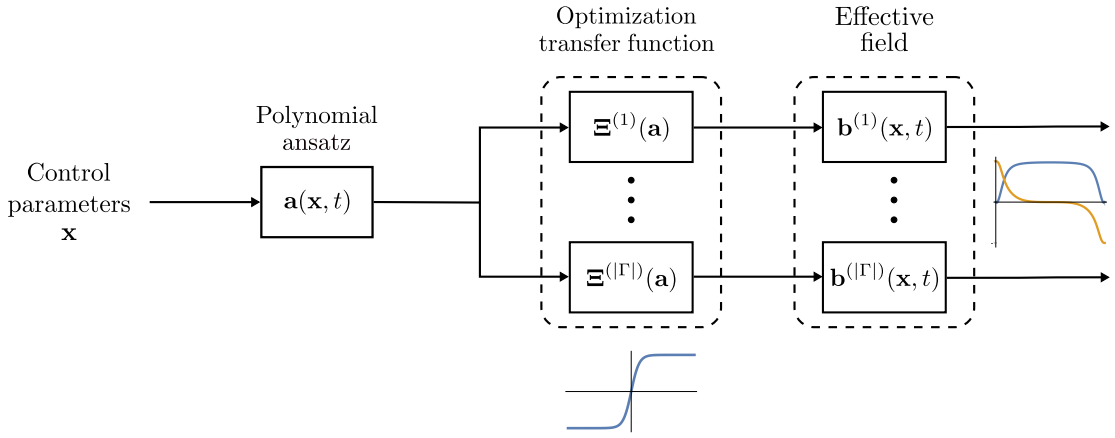

Figure 2.2: Block diagram of constraint implementation using optimization transfer functions. The control parameters are first used to determine the unconstrained waveforms $\mathbf{a}(\mathbf{x},t)$ using one of the ansatz choices of Section 2.8.1, which are then fed to a set of optimization transfer functions, enforcing the constraints for every ensemble member. The resulting effective fields are subsequently provided to the rest of the adiabatic control protocol.

We have thus completed the mathematical description of the adiabatic control protocol. In the following chapter, we present the results of implementing these methods for the design of fast adiabatic passages in an NMR setting.

Chapter 3

NMR Pulse Design and Validation

In the previous chapters, we have described the background and theoretical formulation of our adiabatic control protocol. We are now in a place where we can implement these methods to engineer frequency-modulated adiabatic pulses for magnetic resonance. First, we present some numerically engineered adiabatic full passages (AFP) and compare their performance with the standardized secant hyperbolic pulses discussed in Section 1.4.2. These AFPs are then validated in a multi-spin simulation in the context of our group's nano-MRI experiments on the phosphorus-31 nuclei in an indium phospide sample.

This is followed by a discussion of an AFP for highly interacting electrons, as an example of a pulse with built-in robustness against the dipolar coupling Hamiltonian. The effectiveness of the dipolar decoupling is then examined in a multi-spin simulation. The rest of the chapter is dedicated to a brief example of an adiabatic operation connecting arbitrary states, and tests on the sensitivity of an engineered AFP to noise, as a function of noise amplitude and characteristic correlation time.

3.1 Engineered NMR Adiabatic Full Passages

The first set of pulses are example AFPs designed for spins experiencing Rabi dispersion, such that the maximum available Rabi strength varies in the range $[\Omega_1, 2\Omega_1]$, for some Ω_1. We will normalize frequency and time variables by measuring them in units of the smallest Rabi frequency Ω_1, and its associated Rabi cycle $T_{\text{Rabi}}^{\text{max}} = 2\pi/\Omega_1$, respectively.

The optimization is done using Wolfram Mathematica's FindMaximum conjugate gradient ascent algorithm [61], over a $|\Gamma| = 7$ spin ensemble, utilizing the optimization transfer

function of Eq.(2.58) to enforce maximum amplitude and bandwidth constraints. The maximum Rabi strengths in the representative ensemble are chosen to be $\omega_{1\max}^{(\lambda)}/\Omega_1 \in \{1,\ 1.17,\ 1.33,\ 1.5,\ 1.67,\ 1.83,\ 2\}$, while the maximum resonance offset is restricted to $\Delta\omega_{\max}^{(\lambda)}/\Omega_1 = 10$ to impose bandwidth constraints. The final state and adiabaticity metric coefficients are set to $p_0 = 0.2$ and $p_{\text{ad}} = 0.8$, with no perturbation Hamiltonian in mind. This particular choice of weights is motivated by the fact that a fully adiabatic operation should result in a spin trajectory that exactly follows the effective field, and therefore also ensures that the final state of the system is indeed the target state. However, not including the final state metric altogether could result in the trivial solution $\mathbf{b} = 0$, which is undesirable. Therefore, a small but non-zero final state coefficient is chosen in the optimization.

To parametrize the pulse, we use ansatz I from Section 2.8.1 with 20 coefficients parametrizing each waveform. The IVP of Eq.(2.17) was solved using the explicit Runge-Kutta algorithm of Mathematica's ParametricNDSolve function on each iteration of the optimization loop. The chain rule integral of Eq.(2.25) was also approximated by a finite sum of 100 terms. Initialization of the optimizer was done by taking the seed from a uniform random distribution over the hypercube $[-1/2, 1/2]^{40}$, resetting the optimizer with a new seed if the target function value did not exceed 0.99 after 100 steps.

We conducted three pulse searches of different durations: $T/T_{\text{Rabi}}^{\max} \in \{2.5,\ 5,\ 15\}$. To benchmark the performance of these pulses, three secant hyperbolic AFPs were also designed with the same pulse lengths by optimizing the maximum resonance offset and truncation factor over the intervals $\Delta\omega/\Omega_1 \in [0, 10]$ and $\kappa \in [0, 0.1]$, respectively, using the exact same target function[1]. The resulting optimum secant hyperbolic pulse parameters are:

$T/T_{\text{Rabi}}^{\max}$	2.5	5	15
$\Delta\omega_{\max}^{\text{opt}}/\Omega_1$	0.93	1.09	1.31
κ^{opt}	0.073	0.031	0.009

The numerically derived AFPs along with these reference pulses are depicted in Fig.(3.1-a). The logarithmic infidelity of both the final state metric $\log_{10}(1 - \Phi_0)$ and the adiabaticity metric $\log_{10}(1 - \Phi_{\text{ad}})$ are shown in Fig.(3.1-b) as a function of the maximum Rabi strength, for both the optimal and secant hyperbolic pulses. It can be seen that the final state infidelity of the optimal pulses exceed the reference pulses by at least two orders of magnitude for all three pulse durations. The adiabatic infidelity is also consistently an

[1]The optimization of the secant hyperbolic AFPs was done using the (gradient-free) Nelder-Mead algorithm of Mathematica's NMaximize function.

order of magnitude better across the Rabi strength range for the three pulses. Additionally, observe that both metrics significantly increase when going to longer pulse lengths, as expected from an adiabatic pulse.

As a more intuitive measure of adiabaticity, consider the instantaneous angle between the effective field and the magnetization:

$$\alpha(t) = \cos^{-1}\left(\frac{\mathbf{b}(\mathbf{x}^{\text{opt}},t)\cdot\mathbf{M}(\mathbf{x}^{\text{opt}},t)}{\left|\mathbf{b}(\mathbf{x}^{\text{opt}},t)\right|\left|\mathbf{M}(\mathbf{x}^{\text{opt}},t)\right|}\right), \tag{3.1}$$

with $\mathbf{x}^{\text{opt}}$ being the optimal control parameters, and

$$\mathbf{M}(\mathbf{x}^{\text{opt}},t) = \langle\uparrow| U^{\dagger}(\mathbf{x}^{\text{opt}},t)\boldsymbol{\sigma}U(\mathbf{x}^{\text{opt}},t)\,|\uparrow\rangle \tag{3.2}$$

being the magnetization. The maximum angle $\alpha_{\max} = \text{Max}_{t\in[0,T]}\,\alpha(t)$ for all pulses has been plotted in Fig.(3.2-a) as a function of Rabi strength, indicating a substantial improvement to the adiabaticity for the numerically derived waveforms compared to the reference ones. For instance, in the case of the shortest AFPs, the instantaneous angle is smaller than 8.5° throughout the relevant Rabi frequency range $\omega_{1\max}/\Omega_1 \in [1,2]$, while the corresponding secant hyperbolic pulse reaches a 30° angle. A 2D color plot of the angle as a function of the evolution time and Rabi strength is also provided in Fig.(3.2-b) for the short $T/T_{\text{Rabi}}^{\max} = 2.5$ AFP. It can be seen that in the relevant Rabi range, the maximum angle throughout the evolution mostly occurs in the middle of the pulse, where the spin has reached the transverse plane on the Bloch sphere. Although the shortest pulse exhibits evolution that may not be considered completely adiabatic in these instances, note that the AFP still has a high fidelity, as can be seen in Fig.(3.1-b).

To further validate the numerically designed AFPs, a 7-spin simulation was conducted on the three pulses for the phosphorus-31 (^{31}P) nuclei in an indium phosphide (InP) sample with a Wurtzite structure, which is to be used in a nano-MRI experiment in our research group. The Rabi field in this setup is generated by passing current through a narrow metallic constriction that results in very large, non-uniform fields, roughly in the range $2B_1 \in [480, 1060]$ G, corresponding to $\omega_1/2\pi \in [0.414, 0.913]$ MHz, in the effective sample volume. The static field in this experiment is $B_0 \sim 2.9$ T corresponding to a ^{31}P Larmor frequency of $\sim$ 50 MHz; far greater than the mentioned Rabi range, meaning that the rotating wave approximation is valid. The simulation is therefore done in the FM frame, which is computationally more efficient, since there is no need to resolve the rapid Larmor oscillations of the spins.

We utilize our numerically designed AFPs for the maximum Rabi field range $B_{1\max} \in [250, 500]$ G, which with the gyromagnetic ratio $\gamma_P/2\pi = 17.235$ MHz/T translates to a

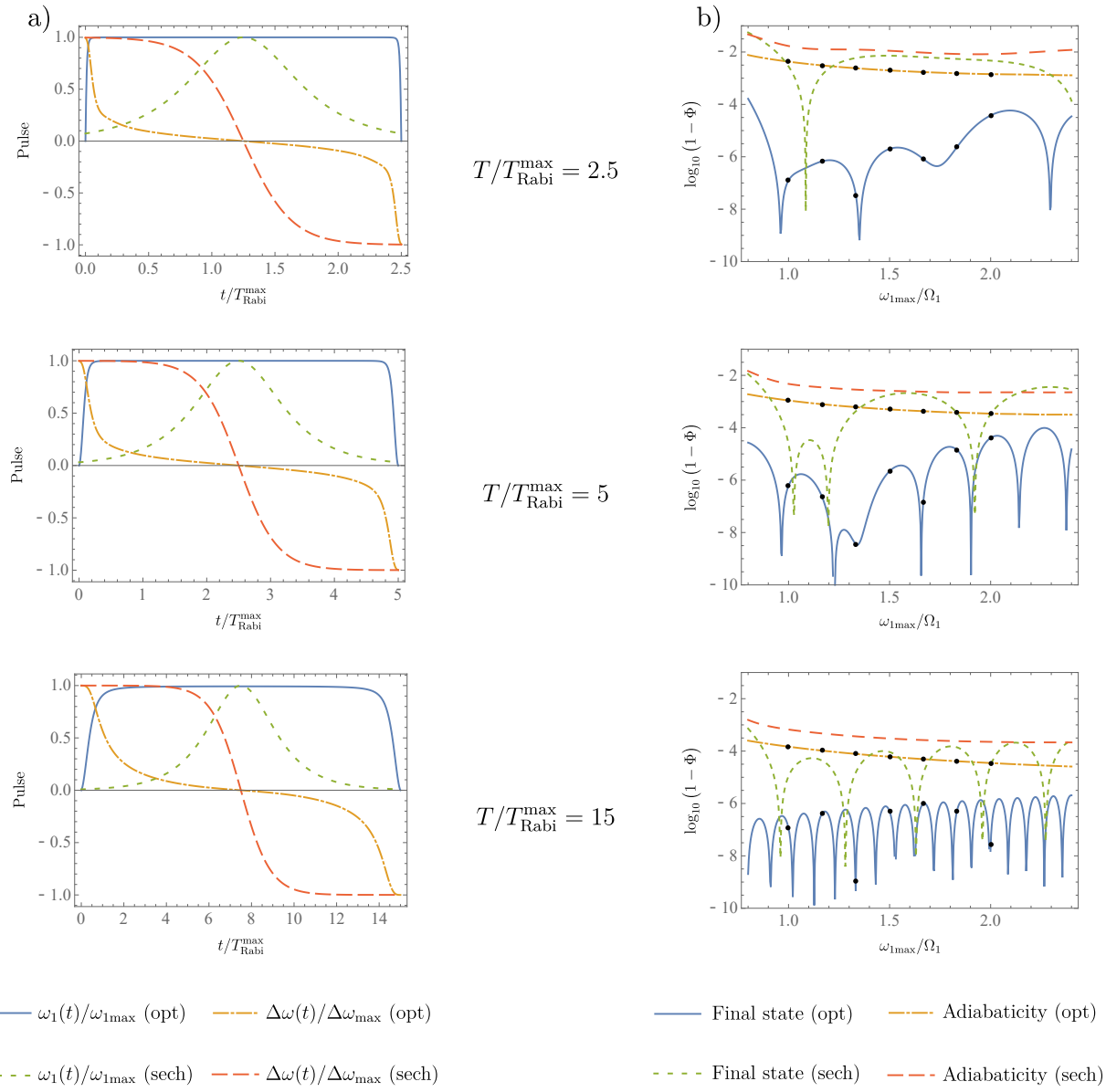

Figure 3.1: a) Numerically designed adiabatic full passages and the reference pulses used for benchmarking. b) Logarithmic infidelities of the final state and adiabaticity metrics for the numerical and secant hyperbolic pulses. The dots indicate the 7 spins in the optimization ensemble, and $\Omega_1 = \underset{\lambda\in\Gamma}{\text{Min}}\ \omega_{1\max}^{(\lambda)}$ is the smallest Rabi strength between the spins.

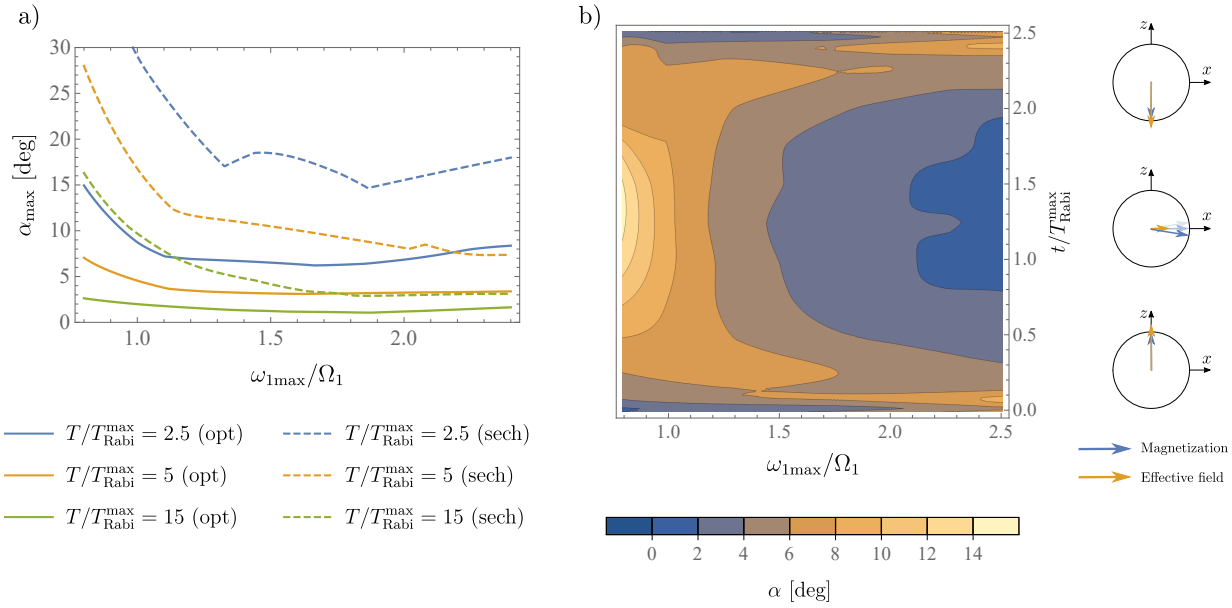

Figure 3.2: a) The maximum effective field-magnetization angle throughout the evolution, as a function of Rabi frequency, for the designed adiabatic full passages. b) 2D plot of the angle as a function of time and Rabi strength for the $T/T_{\text{Rabi}}^{\max} = 2.5$ AFP, with a schematic of the associated magnetization trajectory on the Bloch sphere.

Rabi range of $\omega_{1\max} \in [\Omega_1, 2\Omega_1]$ with $\Omega_1/2\pi = 0.431$ MHz. The maximum resonance offset of the pulse is then accordingly $\Delta\omega_{\max}/2\pi = 10\ \Omega_1/2\pi = 4.309$ MHz.

The spatial distribution of the 7 spins, depicted in Fig.(3.3-d) is taken from part of the Wurtzite structure unit cell, with the B_1 distribution chosen to effectively represent the Rabi inhomogeneity of the setup. The spins experience homonuclear dipole-dipole interaction, which, under the secular approximation, is described by the Hamiltonian [4]

$$H_D = \sum_{j \neq k} D_{jk}\big(3I_j^z I_k^z - \mathbf{I}_j \cdot \mathbf{I}_k\big), \tag{3.3}$$

where

$$D_{jk} = \frac{\mu_0 \hbar \gamma^2}{4\pi} \frac{1 - 3\cos^2\theta_{jk}}{|\mathbf{r}_j - \mathbf{r}_k|^3}, \tag{3.4}$$

are the dipolar coefficients, $\mu_0 = 4\pi \times 10^{-7}$ m.kg.s^{-2}.A^{-2} is the vacuum permeability, $\mathbf{r}_j$ is the position of the j^{th} spin, θ_{jk} is the angle between the static field and the line connecting the spins j and k, and $I_j^\alpha = \mathbb{1}^{\otimes(j-1)} \otimes \sigma_\alpha/2 \otimes \mathbb{1}^{\otimes(7-j)}$ is the $\alpha \in \{x, y, z\}$ component of the

spin in the 7-particle Hilbert space. Note that the secular dipolar Hamiltonian is the same in both the lab frame and the FM frame, as it commutes with the z component of the total spin, and hence the reference frame transformation. This interaction Hamiltonian is calculated using Eq.(3.3, 3.4) according to the spin distribution. The resulting coefficients are all on the order of a few hundred hertz, with the largest one being 479 Hz, corresponding to the closest spins distanced 3.4Å apart. Adding H_D to the FM-frame RF Hamiltonian $H_{\mathrm{RF}} = -\sum_{j=1}^{7} \mathbf{b}_j(t) \cdot \mathbf{I}_j$ gives the total Hamiltonian of the system $H(t) = H_D + H_{\mathrm{RF}}(t)$, with $\mathbf{b}_j(t)$ being the effective field of the j^{th} spin. This total Hamiltonian is then given to the Runge-Kutta algorithm to calculate the propagator of the system according to the IVP $\dot{U}(t) = -iH(t)U(t)$ and $U(0) = \mathbb{1}$.

The final reduced density matrix for the j^{th} spin $\rho_j(T)$ is then calculated by taking the partial trace of the total system's density matrix $\rho(T) = U(T) \left|\uparrow\right\rangle^{\otimes 7} \left\langle\uparrow\right|^{\otimes 7} U^{\dagger}(T)$ over the subspace of the remaining 6 spins. The fidelity of the operation for this spin can then be calculated as:

$$\Phi_j = \mathrm{Tr}\big[\rho_j(T) \left|\downarrow\right\rangle \left\langle\downarrow\right| \big]. \tag{3.5}$$

Eq.(3.5) is used for the optimized AFPs, the result of which is shown in Fig.(3.3-a-c) alongside the single-spin fidelities derived before. All three pulses essentially exhibit the same favorable performance observed in the single-spin case.

3.2 Dipolar-Decoupled Adiabatic Passages for Electrons

We have thus far used the basic form of the adiabatic control protocol to engineer fast adiabatic inversion pulses that far out-perform the standardized secant hyperbolic pulse shape commonly used in many experiments. In the case of the phosphorus spins, the dipolar coupling was not nearly large enough to deteriorate the fidelity of the AFPs. We now discuss the design of inversion pulses for electrons, which can experience much larger dipolar interactions due to their much higher gyromagnetic ratio [1]. We engineer two adiabatic passages, one of which has built-in robustness against dipolar couplings using the perturbative method of Section 2.6.2. The performance of the two pulses are then compared in a multi-spin simulation of highly coupled electrons to investigate the effectiveness of the perturbation metric.

[1] As can be seen in Eq.(3.4), the dipolar coefficients are proportional to γ^2.

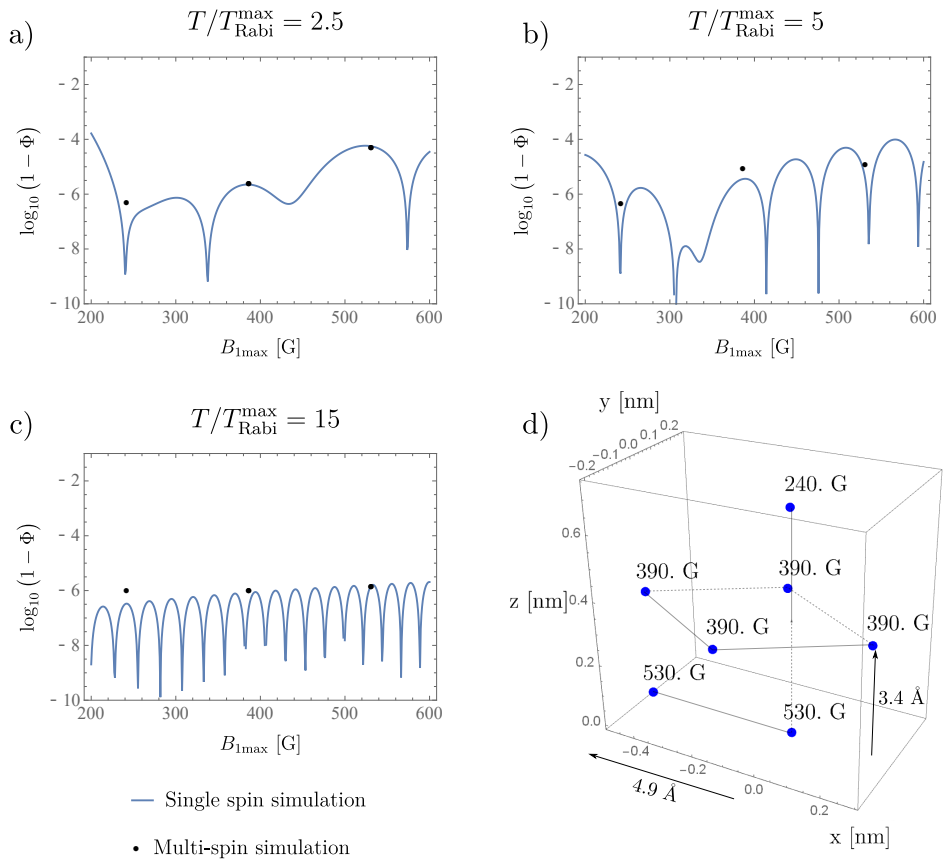

Figure 3.3: Seven-spin simulation of the engineered adiabatic full passages, with the single-spin (line) and 7 spin (dots) final state infidelities of the a) $T/T_{\text{Rabi}}^{\max} = 2.5$, b) $T/T_{\text{Rabi}}^{\max} = 5$ and c) $T/T_{\text{Rabi}}^{\max} = 15$ pulses. c) The spatial distribution of the spins along with the maximum Rabi distribution.

The pulse optimizations are again done on an ensemble of 7 electron spins with gyromagnetic ratios $\gamma_e/2\pi = 28.024$ GHz/T, in the maximum Rabi field range $B_{1\max}^{(\lambda)} \in \{2.7,\ 3.,\ 3.2,\ 3.5,\ 3.8,\ 4.,\ 4.3\}$ G, corresponding to the Rabi frequencies $\omega_{1\max}^{(\lambda)}/2\pi \in \{7.57,\ 8.41\ ,\ 8.97,\ 9.81,\ 10.65,\ 11.21,\ 12.05\}$ MHz. The maximum resonance offset of the pulses is set to $\Delta\omega_{\max}^{(\lambda)}/2\pi = 50$ MHz, and the duration is chosen as $T = 1\ \mu$s, which correspond to $\Delta\omega_{\max}^{(\lambda)}/\text{Min}_{\lambda\in\Gamma}\ \omega_{1\max}^{(\lambda)} = 6.6$ and $T/T_{\text{Rabi}}^{\max} = 7.57$, as measured in units of the longest Rabi cycle.

Similar to the previous section, both pulses were parametrized using ansatz I with 20 optimization parameters per waveform. For one of the pulses, which we will call the

reference pulse, we only use final state and adiabaticity metrics with relative weights $p_0 = 0.2$ and $p_{\text{ad}} = 0.8$. For the other pulse, we use the methods of Section 2.6.2 to construct and calculate a perturbation metric for the two-spin (normalized) dipolar Hamiltonian $H_d = 2\sigma_z \otimes \sigma_z - \sigma_x \otimes \sigma_x - \sigma_y \otimes \sigma_y$. The weights for the three metrics are chosen as $p_0 = 0.2$, $p_{\text{ad}} = 0.5$ and $p_{\text{per}} = 0.3$, and the rest of the optimization is exactly conducted in the same way as before.

The resulting pulses, the control metrics, and the maximum magnetization-effective field angle are shown in Fig.(3.4), indicating a better fidelity for the reference pulse for isolated spins in the relevant Rabi range. Fig.(3.4-c) also seems to favor the reference pulse over the dipolar one, as it exhibits a lower $\alpha(t) \leq 6.5^\circ$ angle throughout the optimized $B_1 \in [2.7,\ 4.3]$ G range, relative to the $\alpha(t) \leq 8^\circ$ angle of the dipolar pulse. Interestingly, it can be seen in Fig.(3.4-d) that including the dipolar interactions seems to suppress the $\alpha(t)$ angle in the middle of the pulse, where the spin is in the transverse plane, and most susceptible to dephasing.

So far we have seen that in general, the reference pulse shows better performance for isolated spins. The pulses are now simulated for 7 interacting electrons, distributed in space according to Fig.(3.5-b). The distribution was chosen by arranging the spins on the faces of a 4 nm-sided cube (and one on the center), and then perturbing the order by adding a random vector to each spin's position from a uniform distribution on the set $[-0.5, 0.5]^3$ nm. The corresponding dipolar Hamiltonian H_D was then calculated from Eq.(3.3, 3.4), the largest coefficient of which was 6.5 MHz. Considering that the magnitude of the effective field, and hence the RF Hamiltonian $H_{\text{RF}}(t)$, is roughly of order $\sqrt{\omega_{1\text{max}}^2 + \Delta\omega^2}/2\pi \sim 50$ MHz, $\|H_D\|$ is approximately an order of magnitude smaller than $\|H_{\text{RF}}(t)\|$, meaning that our perturbative treatment of the interactions is valid.

The calculation of the propagator and the fidelities are done exactly in the same manner as the previous section. The result, depicted in Fig.(3.5-a), clearly shows that despite the better performance of the reference AFP for single spins, the infidelity of the dipolar AFP is approximately two orders of magnitude smaller in the multi-spin case; indicating that our treatment of perturbations in the adiabatic control protocol can be an essential tool for engineering fast and robust adiabatic operations.

3.3 Adiabatic Operation for Arbitrary Points on the Bloch Sphere

Having addressed the problem of engineering adiabatic inversion pulses, we now give a brief example of an operation that evolves an arbitrary point on the Bloch sphere to another

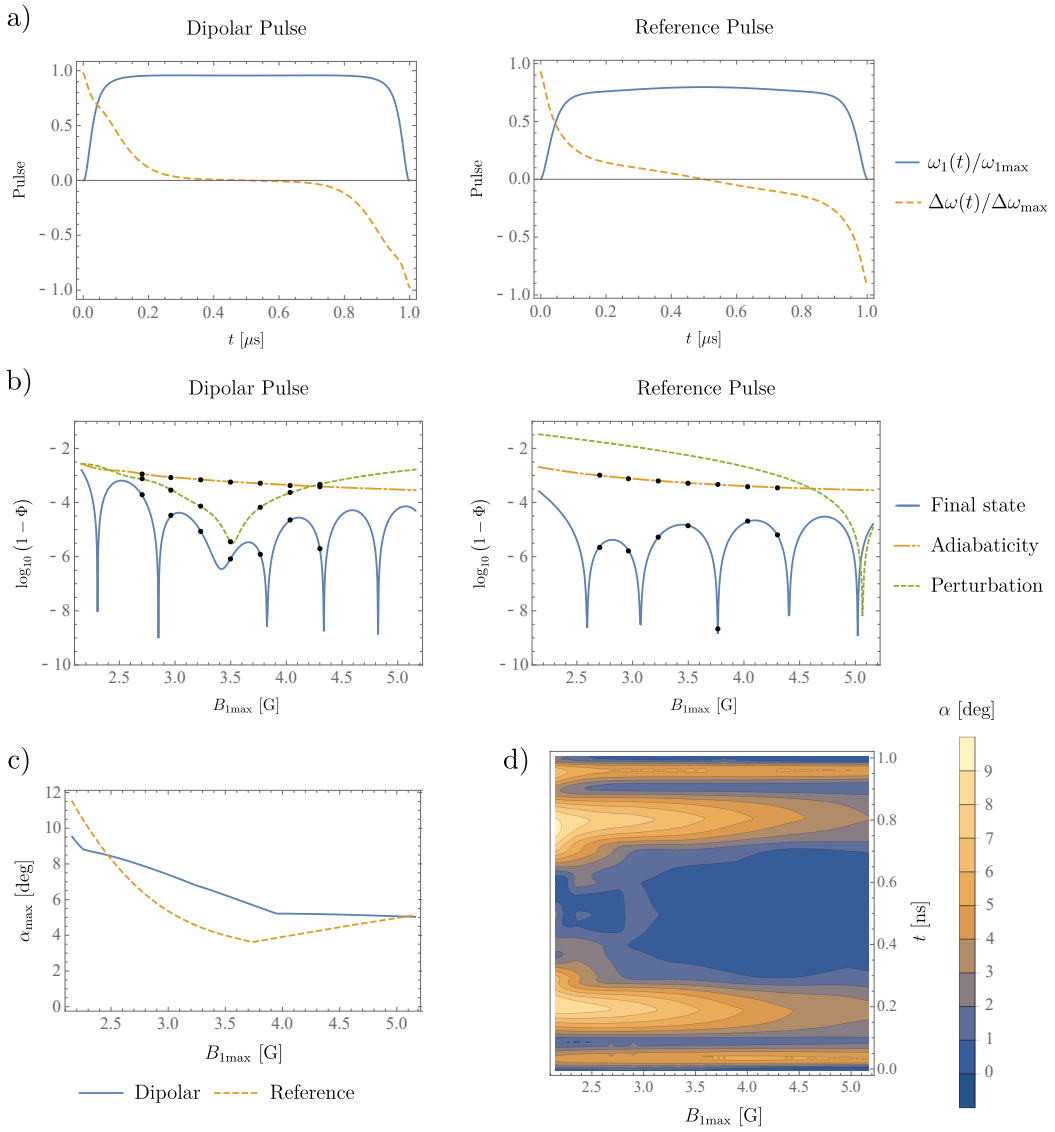

Figure 3.4: Adiabatic full passage designed with the explicit inclusion of dipolar interactions. a) The dipolar and non-dipolar reference pulse. b) Logarithmic infidelities of the control metrics for the dipolar and reference pulses. The dipolar metric plotted for the reference pulse was not accounted for in its optimization. The dots indicate the optimization ensemble. c) The maximum effective field-magnetization angle throughout the evolution as a function of Rabi frequency, and d) 2D plot of the angle as a function of time and maximum Rabi field.

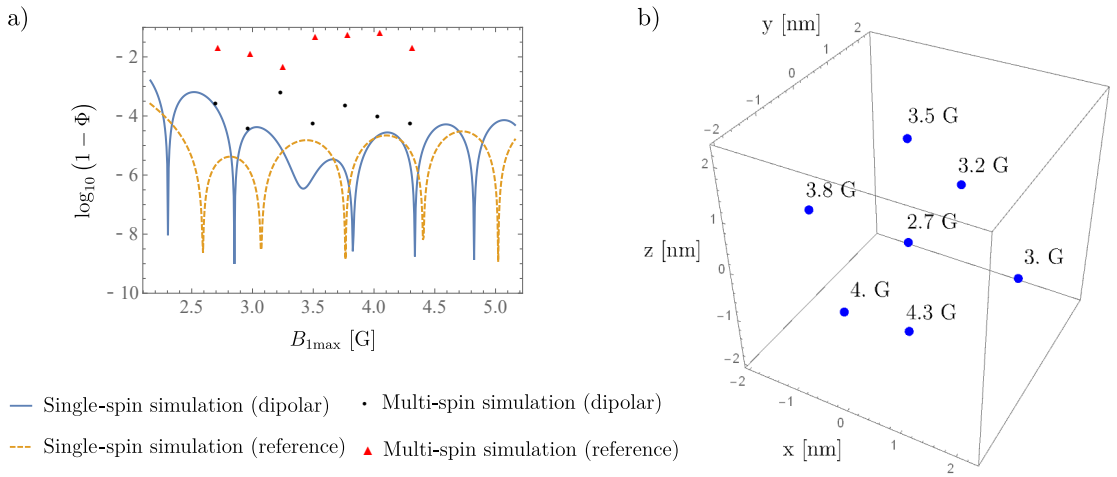

Figure 3.5: Seven-spin simulation of the dipolar adiabatic full passage. a) Multi-spin and single-spin fidelity of the dipolar and reference inversion pulses, indicating a significantly higher robustness to dipolar couplings in the dipolar pulse. b) The 7 spins used in the simulation and the associated Rabi field distribution.

state. For this we design a $T = 13$ μs pulse for ^{31}P spins, using ansatz II from Section 2.8.1 with 10 coefficients per waveform as the control parameters. The optimization transfer function of Eq.(2.59) is used to enforce the bandwidth and amplitude constraints on a single-spin ensemble, which are chosen as $\Delta\omega_{\max}/2\pi = 7.4$ MHz and $B_{1\max} = 260$ G (or $\omega_{1\max}/2\pi = 0.466$ MHz for ^{31}P spins), respectively. The utilized target function coefficients are $p_0 = 0.2$ and $p_{\text{ad}} = 0.8$. The initial and final states for the pulse design are set to $(\theta_i, \varphi_i) = (\pi/3, 0)$ and $(\theta_f, \varphi_f) = (2\pi/3, \pi/2)$, respectively, in spherical coordinates, from which the state vectors $|\psi_0\rangle$ and $|\psi_T\rangle$ are calculated using $|\psi\rangle = \cos\frac{\theta}{2}|\uparrow\rangle + e^{i\varphi}\sin\frac{\theta}{2}|\downarrow\rangle$.

The resulting pulse, along with its associated performance metrics, effective field-magnetization angle $\alpha(t)$, and calculated Bloch sphere trajectory are presented in Fig.(3.6). The results show that the spin follows the effective field with an angle $\alpha(t) \leq 5°$, and reach the final state with a fidelity higher than 0.99999. Observe that the engineered pulse works on a narrower B_1 range than before, since the effective field changes direction when the Rabi strength is varied, meaning that for a fixed resonance offset, it is impossible to have the effective fields for different Rabi strengths point along the same initial magnetization.

The implementation of the adiabatic control protocol has thus far been demonstrated in this chapter by presenting several numerically engineered adiabatic pulses in various settings. We conclude this chapter by studying the robustness of a pulse designed with our protocol against stochastic noise, and investigating the effect of noise amplitude and

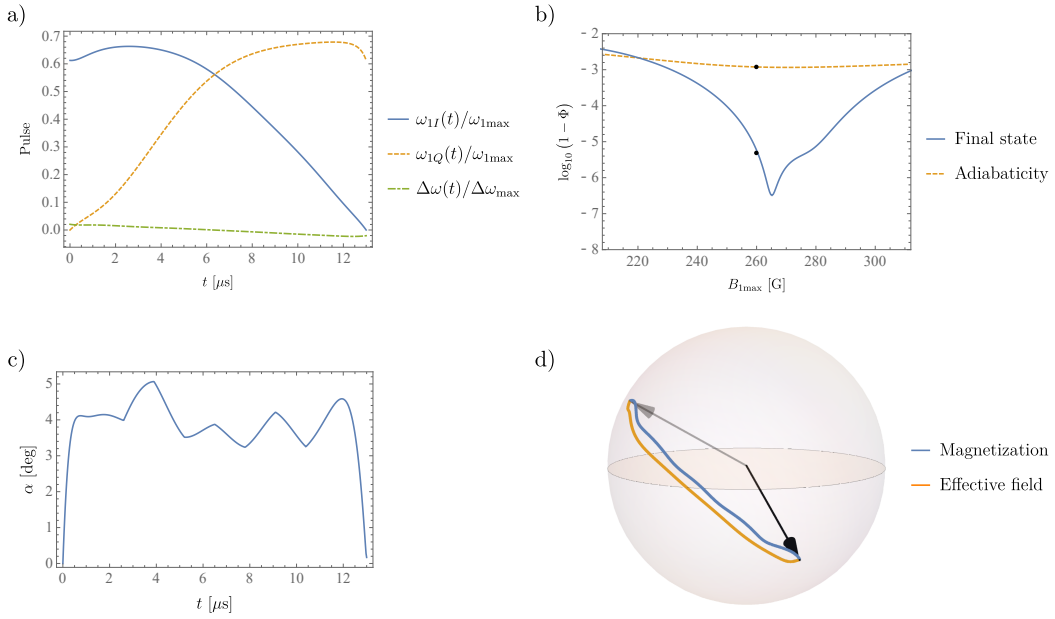

Figure 3.6: a) Adiabatic pulse designed for evolving the $(\theta_i, \varphi_i) = (\pi/3, 0)$ point to $(\theta_f, \varphi_f) = (2\pi/3, \pi/2)$ on the Bloch sphere, b) the associated final state and adiabaticity metrics as a function of Rabi strength, c) the magnetization-effective field angle for $B_{1\max} = 260$ G throughout the evolution, and d) the corresponding Bloch sphere trajectory of the magnetization and effective field.

perhaps more interestingly, its fluctuation time scale, on the fidelity.

3.4 Sensitivity Against Stochastic Noise

To examine the sensitivity of our adiabatic operations, we choose the shortest pulse presented in this work, namely the $T/T_{\text{Rabi}}^{\max} = 2.5$ inversion pulse of Section 3.1. This is because in principle, shorter operations are less robust to imperfections due to their inferior adiabaticity. Our study is done by disturbing the spin with a noise signal $W(t)$, which is a zero-mean wide-sense stationary (WSS) Gaussian random process [62] that couples to the Hamiltonian via one of the Pauli operators σ_i, for $i \in \{x, y, z\}$. In other words, the total Hamiltonian is taken to be

$$H(t) = -\mathbf{b}(t) \cdot \frac{\boldsymbol{\sigma}}{2} + W(t)\frac{\sigma_i}{2}, \tag{3.6}$$

with $\mathbf{b}(t)$ being the effective field of the pulse. Since W is a Gaussian process, is it fully characterized by its mean, which is zero, and its autocorrelation function $R_W(\tau) = \mathbb{E}\big[W(t)W(t+\tau)\big]$ (or equivalently the power spectral density)[1]. Evaluating the effect of the fluctuation time scale on the pulse performance requires an appropriate functional form for $R_W(\tau)$ that allows for the tuning of the characteristic correlation time of the process. One such function is the Gaussian autocorrelation

$$R_W(\tau) = A^2 e^{-(\tau/\tau_c)^2}, \tag{3.7}$$

or equivalently, the power spectral densty

$$S_W(f) \equiv \int_{-\infty}^{\infty} d\tau \; R_W(\tau) e^{-i2\pi f\tau} = \tau_c \sqrt{\pi} e^{-\pi^2 \tau_c^2 f^2}, \tag{3.8}$$

with A and τ_c being the standard deviation and correlation time of the process, respectively. Note that in the limits $\tau_c \to 0$ and $\tau_c \to \infty$, the above process corresponds to white noise and a constant random shift, respectively. We can thus vary A and τ_c to change the noise amplitude and fluctuation rate, and compute the ensemble-averaged fidelity $\Phi_0 \equiv \mathbb{E}\big[|\langle\downarrow| U(t) |\uparrow\rangle|^2\big]$ at every point (A, τ_c) to quantify the effect of the noise.

In order to generate realizations for the random process W, we utilize the fact that the output of a linear time-invariant system with frequency response $H(f)$ to a WSS Gaussian process is also a Gaussian process characterized with the power spectral density $|H(f)|^2 S_W(f)$ [62]. We therefore first generate a white process $\tilde{W}$ in which all time samples are uncorrelated, i.e. $R_{\tilde{W}}(\tau) = A^2\delta(\tau)$, and filter it with the frequency response $H(f) = \tau_c\sqrt{\pi}\exp(-\pi^2\tau_c^2 f^2)$ to create the desired noise.

To simulate the white process $\tilde{W}$, we partition the time interval[2] $[0, 2T]$ into $m = 1000$ time samples of length $\Delta t = 2T/(m-1)$, and generate a set of independent identically-distributed (IID) Gaussian random variables $\{\tilde{W}(n\Delta t)\}_{n=1}^m$ with zero mean and variance $A^2/\Delta t$. As is shown in Appendix I, the continuum limit $m \to \infty$ of such a sequence is a continuous Gaussian process $\tilde{W}$ with constant power spectral density $S_{\tilde{W}}(f) = A^2$, as required. The discrete Fourier transform of this IID process is then calculated, multiplied by $|H(f)|^2$, transformed back into the time domain, and interpolated between the samples to generate the desired noise W with the Gaussian autocorrelation function $R_W(\tau)$.

To validate the noise generation process, we measure the autocorrelation function by averaging the product $W(0)W(\tau)$ over 5000 noise realizations, for each $\tau/T \in [-1, 1]$. Examples of this are depicted in Fig.(3.7), showing excellent agreement with the desired Gaussian autocorrelation.

[1] We use $\mathbb{E}[X]$ to denote the ensemble average of the random variable X.

[2] The noise generation window was picked longer than T in order to prevent boundary effects.

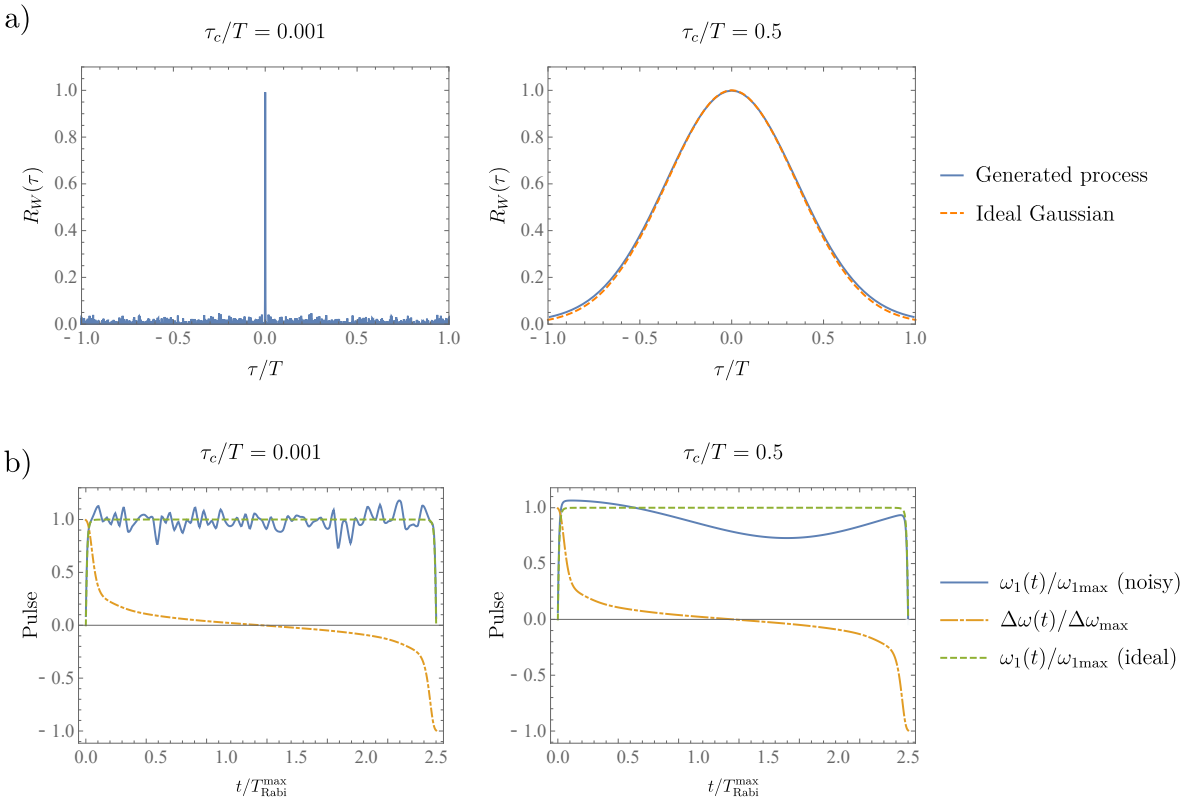

Figure 3.7: a) Measured autocorrelation function of the generated noise for the minimum and maximum correlation time in the sweep. b) Example σ_x noise realizations with the above correlation times added to the pulse.

Our AFP pulse is now simulated on a single spin for different noise parameters $\tau_c/T \in [0.001, 0.5]$ and $A/\omega_{1\text{max}} \in [0, 0.25]$, with 100 points allocated for each sweep direction. The final state fidelity at each (A, τ_c) point is then measured and averaged over 100 noise realizations to estimate Φ_0 in three cases where the noise couples to the Hamiltonian through the σ_x, σ_y and σ_z operators. Examples of the noisy pulse shapes are given in Fig.(3.7) for both short and long correlation times.

The resulting fidelity plots are depicted in Fig.(3.8), indicating that the sensitivity of the pulse is roughly the same for noise in the three Pauli operators. It can be seen that the pulse is most robust for very long and very short correlation times, even tolerating noise amplitudes as big as 15% of the maximum Rabi strength. This is in contrast with the intermediate time scale $\tau_c/T \sim 0.1$ or equivalently $\tau_c/T_{\text{Rabi}}^{\text{max}} \sim 0.25$, for which the performance is more susceptible to deterioration for noise amplitudes of order $A/\omega_{1\text{max}} \gtrsim$

3%. Note that this behavior on fluctuation time scales was expected from our previous discussion about the robustness of adiabatic operations in Section 1.4.1.

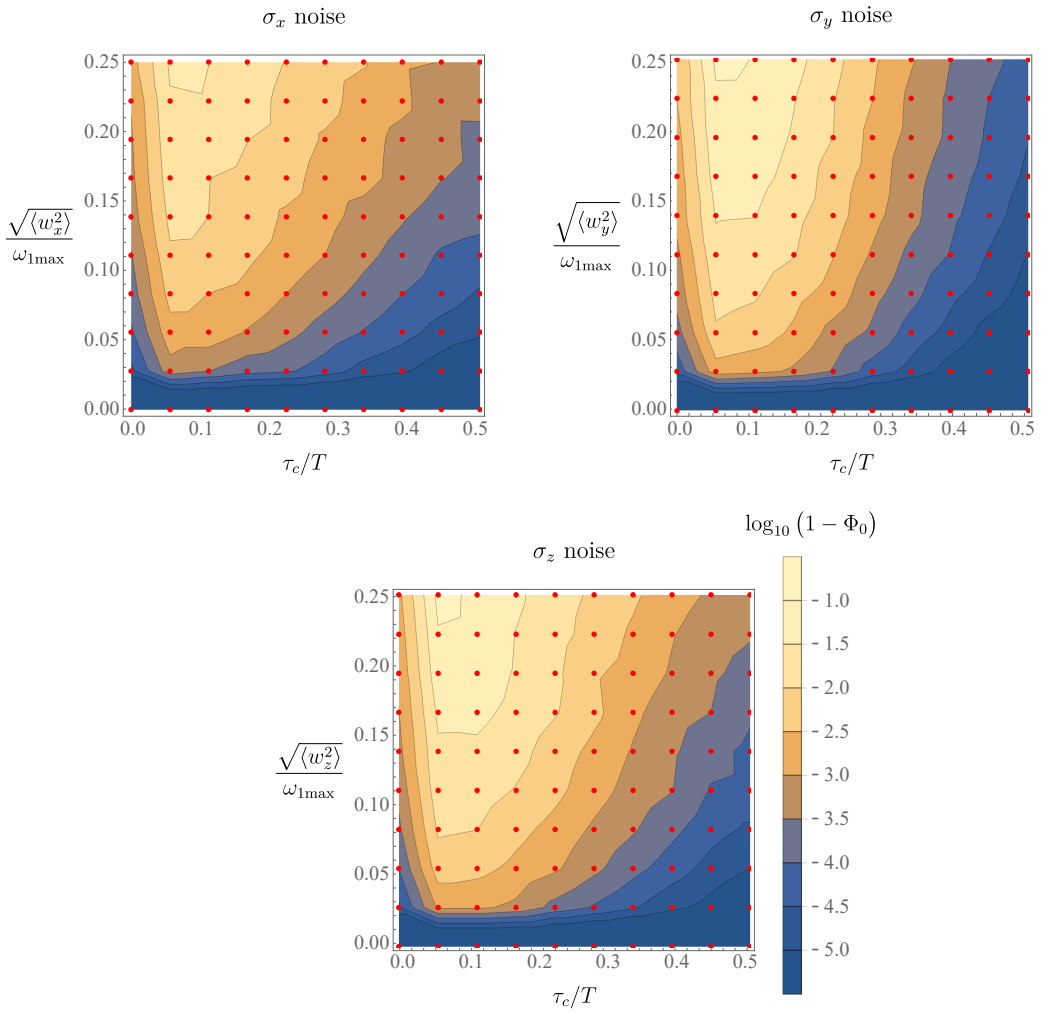

Figure 3.8: Final state infidelities as a function of noise standard deviation and correlation time. The red dots indicate the simulated parameters while all other points are interpolated.

Chapter 4

Conclusion and Outlook

In this thesis, we have developed an efficient numerical adiabatic control protocol which uses gradient-based optimization to engineer fast adiabatic operations on a general two-level system, as well as special cases of multi-level systems such as the important example of NMR adiabatic operations on spin $I > 1/2$ systems. It was demonstrated that a diverse set of imperfections, such as inhomogeneities and unwanted interactions, can be directly and efficiently accounted for in the control searches by including metrics that quantify the robustness of the operation, and fit into the Van Loan block matrix formalism. Since the Hilbert space trajectory of the system is then tailored to the specific perturbations at hand, this added capability can lead to much higher flexibility in adiabatic control, as it lessens the need to compromise the speed of the operation for its robustness.

The control protocol was then utilized to design adiabatic inversion pulses in the context of magnetic resonance, where we showed that it can be used to engineer exceptionally fast pulses, as short as 2.5 Rabi cycles. It was shown that although these pulses deviate from adiabaticity by an angle $\alpha \lesssim 8^\circ$ in limited instances, they still exhibit the high fidelities expected from adiabatic evolution. These designed AFPs were compared with common standardized NMR AFPs of the same duration, and were shown to greatly out-perform them in terms of both the final state fidelity, as well as adiabaticity. We then presented an AFP designed with built-in dipolar decoupling capabilities, and showed the effectiveness of this perturbative treatment by comparing the performance with a non-dipolar reference pulse in a multi-spin simulation of interacting electrons. A brief example was also provided for a pulse connecting arbitrary points on the Bloch sphere, and a numerical study of the sensitivity of the pulses to stochastic fluctuations with different amplitudes and correlation times.

The flexibility of our method in terms of addressing practical imperfections and con-

straints can render it an important tool for a wide variety of applications. For future research, it would be interesting to examine pulses that exhibit deliberate selective behavior to uncertainties and inhomogeneities in system parameters. In particular, the large Rabi dispersion in settings like nano-MRI experiments may be exploited to engineer spatially selective operations such as slice selection pulses, for which the usual techniques are generally inaccessible. In the case of uncertainties, selectivity in the performance of the pulses may provide a method for experimentally probing a quantum system's parameters.

Furthermore, an experimental demonstration of the numerically engineered pulses would be invaluable. Work on this has already started in our research group, and is anticipated to reach a conclusion in the coming months.

References

[1] M. Born and V. Fock. Beweis des adiabatensatzes. *Zeitschrift für Physik*, 51(3):165–180, Mar 1928.

[2] Tosio Kato. On the adiabatic theorem of quantum mechanics. *Journal of the Physical Society of Japan*, 5(6):435–439, 1950.

[3] Michael V. Berry. Quantal phase factors accompanying adiabatic changes. *Proc. Roy. Soc. Lond.*, A392:45–57, 1984.

[4] C.P. Slichter. *Principles of Magnetic Resonance*. Springer Series in Solid-State Sciences. Springer Berlin Heidelberg, 1996.

[5] A. Abragam. *The principles of nuclear magnetism*. International series of monographs on physics. Clarendon Press, 1983.

[6] M. Amniat-Talab, M. Saadati-Niari, and S. Guérin. Quantum state engineering in ion-traps via adiabatic passage. *The European Physical Journal D*, 66(8):216, Aug 2012.

[7] J. I. Cirac, R. Blatt, and P. Zoller. Nonclassical states of motion in a three-dimensional ion trap by adiabatic passage. *Phys. Rev. A*, 49:R3174–R3177, May 1994.

[8] E. Paspalakis and N. J. Kylstra. Coherent manipulation of superconducting quantum interference devices with adiabatic passage. *Journal of Modern Optics*, 51(11):1679–1689, 2004.

[9] K. S. Kumar, A. Vepsäläinen, S. Danilin, and G. S. Paraoanu. Stimulated raman adiabatic passage in a three-level superconducting circuit. *Nature Communications*, 7(1):10628, 2016.

[10] Nikolay V Vitanov, Thomas Halfmann, Bruce W Shore, and Klaas Bergmann. Laser-induced population transfer by adiabatic passage techniques. *Annual Review of Physical Chemistry*, 52(1):763–809, 2001. PMID: 11326080.

[11] K. Bergmann, H. Theuer, and B. W. Shore. Coherent population transfer among quantum states of atoms and molecules. *Rev. Mod. Phys.*, 70:1003–1025, Jul 1998.

[12] Tameem Albash and Daniel A. Lidar. Adiabatic quantum computation. *Rev. Mod. Phys.*, 90:015002, Jan 2018.

[13] Edward Farhi, Jeffrey Goldstone, Sam Gutmann, and Michael Sipser. Quantum computation by adiabatic evolution, 2000.

[14] Dorit. Aharonov, Wim. van Dam, Julia. Kempe, Zeph. Landau, Seth. Lloyd, and Oded. Regev. Adiabatic quantum computation is equivalent to standard quantum computation. *SIAM Journal on Computing*, 37(1):166–194, 2007.

[15] Xinhua Peng, Zeyang Liao, Nanyang Xu, Gan Qin, Xianyi Zhou, Dieter Suter, and Jiangfeng Du. Quantum adiabatic algorithm for factorization and its experimental implementation. *Phys. Rev. Lett.*, 101:220405, Nov 2008.

[16] Matthias Steffen, Wim van Dam, Tad Hogg, Greg Breyta, and Isaac Chuang. Experimental implementation of an adiabatic quantum optimization algorithm. *Phys. Rev. Lett.*, 90:067903, Feb 2003.

[17] Holger Haas, Daniel Puzzuoli, Feihao Zhang, and David G Cory. Engineering effective hamiltonians. *New Journal of Physics*, 21(10):103011, oct 2019.

[18] J. J. Sakurai and Jim Napolitano. *Modern Quantum Mechanics*. Cambridge University Press, 2 edition, 2017.

[19] Paul Adrien Maurice Dirac and Ralph Howard Fowler. On the theory of quantum mechanics. *Proceedings of the Royal Society of London. Series A, Containing Papers of a Mathematical and Physical Character*, 112(762):661–677, 1926.

[20] J.K. Hale. *Ordinary Differential Equations*. Dover Books on Mathematics Series. Dover Publications, 2009.

[21] F. J. Dyson. The radiation theories of tomonaga, schwinger, and feynman. *Phys. Rev.*, 75:486–502, Feb 1949.

[22] Wilhelm Magnus. On the exponential solution of differential equations for a linear operator. *Communications on Pure and Applied Mathematics*, 7(4):649–673, 1954.

[23] G.B. Arfken, H.J. Weber, and F.E. Harris. *Mathematical Methods for Physicists: A Comprehensive Guide*. Elsevier Science, 2011.

[24] S. Blanes, F. Casas, J.A. Oteo, and J. Ros. The Magnus expansion and some of its applications. *Physics Reports*, 470(5):151 – 238, 2009.

[25] Peter Szekeres. *A Course in Modern Mathematical Physics: Groups, Hilbert Space and Differential Geometry*. Cambridge University Press, 2004.

[26] U. Haeberlen and J. S. Waugh. Coherent averaging effects in magnetic resonance. *Phys. Rev.*, 175:453–467, Nov 1968.

[27] Ulrich. Haeberlen. *High resolution NMR in solids : selective averaging*. Academic Press New York, 1976.

[28] Ryogo Kubo. Stochastic liouville equations. *Journal of Mathematical Physics*, 4(2):174–183, 1963.

[29] Haas, Holger. *Engineering Effective Hamiltonians for Magnetic Resonance*. PhD dissertation, University of Waterloo, 2019.

[30] C. Van Loan. Computing integrals involving the matrix exponential. *IEEE Transactions on Automatic Control*, 23(3):395–404, June 1978.

[31] F. Carbonell, J.C. Jímenez, and L.M. Pedroso. Computing multiple integrals involving matrix exponentials. *Journal of Computational and Applied Mathematics*, 213(1):300 – 305, 2008.

[32] D. L. Goodwin and Ilya Kuprov. Auxiliary matrix formalism for interaction representation transformations, optimal control, and spin relaxation theories. *The Journal of Chemical Physics*, 143(8):084113, 2015.

[33] David L. Goodwin. *Advanced optimal control methods for spin systems*. PhD dissertation, University of Southampton, October 2017.

[34] Shai Machnes, Elie Assémat, David Tannor, and Frank K. Wilhelm. Tunable, flexible, and efficient optimization of control pulses for practical qubits. *Phys. Rev. Lett.*, 120:150401, Apr 2018.

[35] Joseph E. Avron and Alexander Elgart. Adiabatic theorem without a gap condition. *Communications in Mathematical Physics*, 203(2):445–463, Jun 1999.

[36] Gustavo Rigolin and Gerardo Ortiz. Degenerate adiabatic perturbation theory: Foundations and applications. *Phys. Rev. A*, 90:022104, Aug 2014.

[37] Gustavo Rigolin and Gerardo Ortiz. Adiabatic theorem for quantum systems with spectral degeneracy. *Phys. Rev. A*, 85:062111, Jun 2012.

[38] M. Maamache and Y. Saadi. Adiabatic theorem and generalized geometrical phase in the case of continuous spectra. *Phys. Rev. Lett.*, 101:150407, Oct 2008.

[39] J W Zwanziger, M Koenig, and A Pines. Berry's phase. *Annual Review of Physical Chemistry*, 41(1):601–646, 1990.

[40] Raffaele Resta. Manifestations of berry's phase in molecules and condensed matter. *Journal of Physics: Condensed Matter*, 12(9):R107–R143, feb 2000.

[41] Di Xiao, Ming-Che Chang, and Qian Niu. Berry phase effects on electronic properties. *Rev. Mod. Phys.*, 82:1959–2007, Jul 2010.

[42] Andrew M. Childs, Edward Farhi, and John Preskill. Robustness of adiabatic quantum computation. *Phys. Rev. A*, 65:012322, Dec 2001.

[43] S. Ashhab, J. R. Johansson, and Franco Nori. Decoherence in a scalable adiabatic quantum computer. *Phys. Rev. A*, 74:052330, Nov 2006.

[44] Tameem Albash and Daniel A. Lidar. Decoherence in adiabatic quantum computation. *Phys. Rev. A*, 91:062320, Jun 2015.

[45] Michael Garwood and Lance DelaBarre. The return of the frequency sweep: Designing adiabatic pulses for contemporary nmr. *Journal of Magnetic Resonance*, 153(2):155 – 177, 2001.

[46] M. Mehring. *High resolution NMR spectroscopy in solids*. NMR (Series). Springer-Verlag, 1976.

[47] Kazuyuki Fujii. Introduction to the rotating wave approximation (rwa) : Two coherent oscillations. *Journal of Modern Physics*, 08, 01 2013.

[48] Robin A. De Graaf and Klaas Nicolay. Adiabatic rf pulses: Applications to in vivo nmr. *Concepts in Magnetic Resonance*, 9(4):247–268, 1997.

[49] J. Baum, R. Tycko, and A. Pines. Broadband and adiabatic inversion of a two-level system by phase-modulated pulses. *Phys. Rev. A*, 32:3435–3447, Dec 1985.

[50] M.S Silver, R.I Joseph, and D.I Hoult. Highly selective $\pi 2$ and π pulse generation. *Journal of Magnetic Resonance (1969)*, 59(2):347 – 351, 1984.

[51] Gregory Quiroz. Robust quantum control for adiabatic quantum computation. *Phys. Rev. A*, 99:062306, Jun 2019.

[52] J. Nehrkorn, S. Montangero, A. Ekert, A. Smerzi, R. Fazio, and T. Calarco. Staying adiabatic with unknown energy gap, 2011.

[53] A. T. Rezakhani, W.-J. Kuo, A. Hamma, D. A. Lidar, and P. Zanardi. Quantum adiabatic brachistochrone. *Phys. Rev. Lett.*, 103:080502, Aug 2009.

[54] Jonathan Vandermause and Chandrasekhar Ramanathan. Superadiabatic control of quantum operations. *Phys. Rev. A*, 93:052329, May 2016.

[55] Michaël Deschamps, Gwendal Kervern, Dominique Massiot, Guido Pintacuda, Lyndon Emsley, and Philip J. Grandinetti. Superadiabaticity in magnetic resonance. *The Journal of Chemical Physics*, 129(20):204110, 2008.

[56] Constantin Brif, Matthew D Grace, Mohan Sarovar, and Kevin C Young. Exploring adiabatic quantum trajectories via optimal control. *New Journal of Physics*, 16(6):065013, jun 2014.

[57] J.C. Butcher. A history of Runge-Kutta methods. *Applied Numerical Mathematics*, 20(3):247 – 260, 1996.

[58] S. Hassani. *Mathematical Physics: A Modern Introduction to Its Foundations*. Springer International Publishing, 2013.

[59] Tak-San Ho, Jason Dominy, and Herschel Rabitz. Landscape of unitary transformations in controlled quantum dynamics. *Phys. Rev. A*, 79:013422, Jan 2009.

[60] Tak-San Ho and Herschel Rabitz. Why do effective quantum controls appear easy to find? *Journal of Photochemistry and Photobiology A: Chemistry*, 180(3):226 – 240, 2006. Coherent Control of Photochemical and Photobiological Processes.

[61] Wolfram Research, Inc. Mathematica, Version 12.0. Champaign, IL, 2019.

[62] Athanasios Papoulis and S. Unnikrishna Pillai. *Probability, Random Variables, and Stochastic Processes*. McGraw Hill, Boston, fourth edition, 2002.

[63] F. Bloch. Nuclear induction. *Phys. Rev.*, 70:460–474, Oct 1946.

[64] F. Bloch, W. W. Hansen, and M. Packard. The nuclear induction experiment. *Phys. Rev.*, 70:474–485, Oct 1946.

[65] Jérémie Roland and Nicolas J. Cerf. Quantum search by local adiabatic evolution. *Phys. Rev. A*, 65:042308, Mar 2002.

[66] Satoshi Morita and Hidetoshi Nishimori. Mathematical foundation of quantum annealing. *Journal of Mathematical Physics*, 49(12):125210, 2008.

[67] Kazuya Kaneko and Hidetoshi Nishimori. Adiabatic approximation for the imaginary-time schrödinger equation and its application to simulated annealing. *Journal of the Physical Society of Japan*, 84(9):094001, 2015.

[68] J. Schwinger. *On Angular Momentum*. Dover Books on Physics. Dover Publications, 2015.

[69] Michael A. Nielsen and Isaac L. Chuang. *Quantum Computation and Quantum Information: 10th Anniversary Edition*. Cambridge University Press, New York, NY, USA, 10th edition, 2011.

[70] A. T. Rezakhani, A. K. Pimachev, and D. A. Lidar. Accuracy versus run time in an adiabatic quantum search. *Phys. Rev. A*, 82:052305, Nov 2010.

APPENDICES

Appendix A

Proof of the Van Loan Relations

In this appendix, we prove the Van Loan relation

$$\mathrm{Texp}\left(\int_0^t dt' \begin{bmatrix} G(t') & A_1(t') & 0 & \dots & 0 & 0 \\ 0 & G(t') & A_2(t') & \dots & 0 & 0 \\ 0 & 0 & G(t') & \dots & 0 & 0 \\ \vdots & \vdots & \vdots & \ddots & \vdots & \vdots \\ 0 & 0 & 0 & \dots & G(t') & A_n(t') \\ 0 & 0 & 0 & \dots & 0 & G(t') \end{bmatrix}\right) =$$

$$\begin{bmatrix} U_t[G] & \mathcal{D}_U(A_1;t) & \mathcal{D}_U(A_1,A_2;t) & \dots & \mathcal{D}_U(A_1,...,A_{n-1};t) & \mathcal{D}_U(A_1,...,A_n;t) \\ 0 & U_t[G] & \mathcal{D}_U(A_2;t) & \dots & \mathcal{D}_U(A_2,...,A_{n-1};t) & \mathcal{D}_U(A_2,...,A_n;t) \\ 0 & 0 & U_t[G] & \dots & \mathcal{D}_U(A_3,...,A_{n-1};t) & \mathcal{D}_U(A_3,...,A_n;t) \\ \vdots & \vdots & \vdots & \ddots & \vdots & \vdots \\ 0 & 0 & 0 & \dots & U_t[G] & \mathcal{D}_U(A_n;t) \\ 0 & 0 & 0 & \dots & 0 & U_t[G] \end{bmatrix}, \quad \text{(A.1)}$$

for any set of square-matrix valued functions $G, A_1, ..., A_n$, and the propagator associated with the generator G,

$$U_t[G] \equiv \mathrm{Texp}\Big[\int_0^t dt' G(t')\Big]. \quad \text{(A.2)}$$

To derive Eq.(A.1), we call the matrix inside the left-hand side integral $L(t)$, and we

use the ansatz

$$\mathrm{Texp}\Big[\int_0^t dt'\ L(t)\Big] \equiv V(t) \equiv \begin{bmatrix} B_{11}(t) & B_{12}(t) & \dots & B_{1,n-1}(t) & B_{1n}(t) \\ 0 & B_{22}(t) & \dots & B_{2,n-1}(t) & B_{2n}(t) \\ 0 & 0 & \dots & B_{3,n-1}(t) & B_{3n}(t) \\ \vdots & \vdots & \ddots & \vdots & \vdots \\ 0 & 0 & \dots & 0 & B_{nn}(t) \end{bmatrix}. \tag{A.3}$$

Substituting this in the defining IVP of the time-ordered exponential $\frac{d}{dt}V(t) = L(t)V(t)$, with $V(0) = \mathbb{1}$, and equating the two sides gives

$$\frac{d}{dt}B_{ij}(t) = \begin{cases} G(t)B_{ii}(t) & i = j \\ G(t)B_{ij}(t) + A_i(t)B_{i+1,j}(t) & j > i \end{cases}, \tag{A.4}$$

for which using the change of variables $\tilde{B}_{ij}(t) \equiv U_t^{-1}[G]B_{ij}(t)$, along with Eq.(1.4), results in

$$\frac{d}{dt}\tilde{B}_{ij}(t) = \begin{cases} 0 & i = j \\ \big(U_t^{-1}[G]A_i(t)U_t[G]\big)\tilde{B}_{i+1,j}(t) & j > i \end{cases}, \tag{A.5}$$

or,

$$\begin{cases} \dfrac{d}{dt}\tilde{B}_{ii}(t) = 0 \\ \dfrac{d}{dt}\tilde{B}_{i-1,i}(t) = \big(U_t^{-1}[G]A_{i-1}(t)U_t[G]\big)\tilde{B}_{ii}(t) \\ \dfrac{d}{dt}\tilde{B}_{i-2,i}(t) = \big(U_t^{-1}[G]A_{i-2}(t)U_t[G]\big)\tilde{B}_{i-1,i}(t) \\ \qquad \vdots \\ \dfrac{d}{dt}\tilde{B}_{1,i}(t) = \big(U_t^{-1}[G]A_1(t)U_t[G]\big)\tilde{B}_{2,i}(t) \end{cases}. \tag{A.6}$$

The solution to Eq.(A.6) is found by solving the top equation, using its solution in the subsequent one, and continuing this process until all $\tilde{B}_{ij}(t)$ have been found. Switching back to the original variables $B_{ij}(t)$ gives

$$B_{ij}(t) = \begin{cases} U_t[G] & j = i \\ U_t[G]\displaystyle\int_0^t dt_0 \dots \int_0^{t_{j-i-1}} dt_{j-i} \prod_{m=0}^{j-i} U_{t_m}^{-1}[G]\ A_{i+m}(t_m)\ U_{t_m}[G] & j > i \end{cases}, \tag{A.7}$$

which in conjuction with Eq.(A.3, 1.18) results in Eq.(A.1), as desired.

Appendix B

Review of the Adiabatic Theorem

This appendix is a review of the adiabatic theorem and its derivation.

There are various versions of the adiabatic theorem in the literature, in varying degrees of rigor (see [12] for a comprehensive list). Here we follow the approach suggested in [24], and also parts of [66, 67].

To study the system in the limit of a slowly-varying excitation, we write the Hamiltonian as a function of the scaled time t/T, i.e. $H(t/T)$. This allows for a controlled way to make the Hamiltonian vary more slowly by increasing T. With this in mind, the IVP of Eq.(1.2) for the propagator is

$$\begin{cases} \dfrac{d}{dt}U(t) = -iH\Big(\dfrac{t}{T}\Big)\ U(t) \\ U(0) = \mathbb{1} \end{cases} \qquad t \in [0, T]. \tag{B.1}$$

Changing variables to the normalized time $s \equiv t/T$ gives

$$\begin{cases} \dfrac{d}{ds}\mathcal{U}(s) = -i\ TH(s)\ \mathcal{U}(s) \\ \mathcal{U}(0) = \mathbb{1} \end{cases} \qquad s \in [0, 1], \tag{B.2}$$

with $\mathcal{U}(s) \equiv U(Ts)$. Denoting the eigenbasis of $H(s)$ by $\{|\mathcal{E}_n(s)\rangle\}_{n=1}^{d}$,[1] we now transform into a reference frame in which these eigenvectors are stationary, i.e. a reference frame defined by

$$W(s) \equiv \sum_{n=1}^{d} |\mathcal{E}_n(0)\rangle\langle\mathcal{E}_n(s)|, \tag{B.3}$$

[1] Clearly $|\mathcal{E}_n(s)\rangle = |E_n(Ts)\rangle = |E_n(t)\rangle$.

with pure states being transformed as $|\tilde{\psi}(s)\rangle = W(s)|\psi(s)\rangle = W(s)\,\mathcal{U}(s)|\psi(0)\rangle$, meaning that the propagator in the new frame is $\tilde{\mathcal{U}}(s) \equiv W(s)\,\mathcal{U}(s)$. Calculating the time derivative of $\tilde{\mathcal{U}}(s)$ and using Eq.(B.2) gives the equivalent IVP for the propagator in the new reference frame:

$$\begin{aligned}\frac{d}{ds}\tilde{\mathcal{U}}(s) &= \frac{d}{ds}\big[W(s)\,\mathcal{U}(s)\big] \\ &= \frac{dW(s)}{ds}\mathcal{U}(s) - iT\,W(s)H(s)\,\mathcal{U}(s) \\ &= -i\Big(i\frac{dW(s)}{ds}W^{\dagger}(s) + T\,W(s)H(s)W^{\dagger}(s)\Big)\tilde{\mathcal{U}}(s),\end{aligned} \tag{B.4}$$

or equivalently

$$\begin{cases}\dfrac{d}{ds}\tilde{\mathcal{U}}(s) = -i\tilde{H}(s)\tilde{\mathcal{U}}(s) \\ \tilde{\mathcal{U}}(0) = \mathbb{1}\end{cases} \qquad s \in [0,1], \tag{B.5}$$

with

$$\tilde{H}(s) \equiv \underbrace{T\,W(s)H(s)W^{\dagger}(s)}_{\tilde{H}_0(s)} + \underbrace{i\frac{dW(s)}{ds}W^{\dagger}(s)}_{\delta\tilde{H}(s)}, \tag{B.6}$$

being the new Hamiltonian. The advantage of the new reference frame can already be seen from Eq.(B.5); the problem of a slowly varying Hamiltonian has now been mapped onto a problem in perturbation theory, since $\|\tilde{H}_0(s)\| \gg \|\delta\tilde{H}(s)\|$ for sufficiently large T. This will also give us a more precise measure of how slow the Hamiltonian needs to be for it to undergo adiabatic evolution.

We now calculate the two terms in the new Hamiltonian Eq.(B.6), using Eq.(B.3):

$$\begin{aligned}\tilde{H}_0(s) &= T\,W(s)H(s)W^{\dagger}(s) \\ &= T\,W(s)\Big(\sum_{n=1}^{d}\mathcal{E}_n(s)|\mathcal{E}_n(s)\rangle\langle\mathcal{E}_n(s)|\Big)W^{\dagger}(s) \\ &= T\sum_{n=1}^{d}\mathcal{E}_n(s)W(s)|\mathcal{E}_n(s)\rangle\langle\mathcal{E}_n(s)|W^{\dagger}(s) \\ &= T\sum_{n=1}^{d}\mathcal{E}_n(s)|\mathcal{E}_n(0)\rangle\langle\mathcal{E}_n(0)|,\end{aligned} \tag{B.7}$$

and

$$\begin{aligned}\delta\tilde{H}(s) &= i\frac{dW(s)}{ds}W^{\dagger}(s)\\ &= i\sum_{n=1}^{d}|\mathcal{E}_n(0)\rangle\frac{d}{ds}\langle\mathcal{E}_n(s)|\ \sum_{m=1}^{d}|\mathcal{E}_m(s)\rangle\langle\mathcal{E}_m(0)|\\ &= i\sum_{n=1}^{d}\sum_{m=1}^{d}\langle\mathcal{E}_m(s)|\frac{d}{ds}|\mathcal{E}_n(s)\rangle^*\ |\mathcal{E}_n(0)\rangle\langle\mathcal{E}_m(0)|. \end{aligned} \tag{B.8}$$

With this in mind, we can use perturbation theory to derive an expansion for the propagator $\tilde{\mathcal{U}}$ in powers of $1/T$. First note that since $\tilde{H}_0(s)$ commutes with itself at all times, the propagator for the unperturbed Hamiltonian is

$$\tilde{\mathcal{U}_0}(s) = \sum_{n=1}^{d} e^{-iT\int_0^s ds'\mathcal{E}_n(s')}|\mathcal{E}_n(0)\rangle\langle\mathcal{E}_n(0)|. \tag{B.9}$$

We can now use the Magnus expansion Eq.(1.15,1.16) on the interaction picture generator $-i\ \tilde{\mathcal{U}}_0^{\dagger}(s)\delta\tilde{H}(s)\tilde{\mathcal{U}}_0(s)$ to compute the perturbed propagator. The interaction picture generator is

$$\begin{aligned}&-i\ \tilde{\mathcal{U}}_0^{\dagger}(s)\delta\tilde{H}(s)\tilde{\mathcal{U}}_0(s) =\\ &\qquad\sum_{n=1}^{d}\sum_{m=1}^{d} e^{-iT\int_0^s ds'(\mathcal{E}_m(s')-\mathcal{E}_n(s'))}\langle\mathcal{E}_m(s)|\frac{d}{ds}|\mathcal{E}_n(s)\rangle^*\ |\mathcal{E}_n(0)\rangle\langle\mathcal{E}_m(0)|. \end{aligned} \tag{B.10}$$

This can be rewritten by realizing that since the instantaneous eigenvectors are normalized, $\frac{d}{ds}\langle\mathcal{E}_n(s)|\mathcal{E}_n(s)\rangle = \frac{d}{ds}\mathbb{1} = 0$. This gives $\langle\mathcal{E}_n(s)|\frac{d}{ds}|\mathcal{E}_n(s)\rangle^* = -\langle\mathcal{E}_n(s)|\frac{d}{ds}|\mathcal{E}_n(s)\rangle$. In other words, the quantity $-i\langle\mathcal{E}_n(s)|\frac{d}{ds}|\mathcal{E}_n(s)\rangle$ is real for all $s\in[0,1]$. Also, since $|\mathcal{E}_n(s)\rangle$ is an eigenvector, $H(s)|\mathcal{E}_n(s)\rangle = \mathcal{E}_n(s)|\mathcal{E}_n(s)\rangle$. Taking a derivative from both sides and multiplying by $\langle\mathcal{E}_m(s)|$ from the left results in

$$\langle\mathcal{E}_m(s)|\frac{d}{ds}|\mathcal{E}_n(s)\rangle = \frac{\langle\mathcal{E}_m(s)|\frac{d}{ds}H(s)|\mathcal{E}_n(s)\rangle}{\mathcal{E}_n(s)-\mathcal{E}_m(s)} \qquad m\neq n. \tag{B.11}$$

For future convenience, we define the following notations:

$$\begin{cases} A_{nm}(s) \equiv \dfrac{\langle\mathcal{E}_m(s)|\frac{d}{ds}H(s)|\mathcal{E}_n(s)\rangle}{\left(\mathcal{E}_n(s)-\mathcal{E}_m(s)\right)^2}\\ \theta_m(s) \equiv \displaystyle\int_0^s ds'\mathcal{E}_m(s') \\ \gamma_m(s) \equiv -i\displaystyle\int_0^s ds'\langle\mathcal{E}_m(s)|\frac{d}{ds}|\mathcal{E}_m(s)\rangle \end{cases}. \tag{B.12}$$

Rewriting Eq.(B.10) using Eq.(B.11, B.12) results in

$$
\begin{aligned}
-i\,\tilde{\mathcal{U}}_0^\dagger(s)\delta\tilde{H}(s)\tilde{\mathcal{U}}_0(s) = \\
&- i\sum_{n=1}^{d}\frac{d\gamma_n(s)}{ds}\;|\mathcal{E}_n(0)\rangle\langle\mathcal{E}_n(0)| \\
&+ \sum_{n\neq m} e^{iT(\theta_n(s)-\theta_m(s))}\big(\mathcal{E}_n(s)-\mathcal{E}_m(s)\big)A_{nm}(s)\;|\mathcal{E}_n(0)\rangle\langle\mathcal{E}_m(0)|, \qquad \text{(B.13)}
\end{aligned}
$$

where we separated the T-dependent and T-independent parts of the operator. The first order Magnus term is

$$
\begin{aligned}
\delta\tilde{\mathcal{G}}_1(s) &= -i\int_0^s ds'\;\tilde{\mathcal{U}}_0^\dagger(s')\delta\tilde{H}(s')\tilde{\mathcal{U}}_0(s') \\
&= -i\sum_{n=1}^{d}\gamma_n(s)\;|\mathcal{E}_n(0)\rangle\langle\mathcal{E}_n(0)| \\
&\quad + \sum_{n\neq m}\int_0^s ds'\;e^{iT(\theta_n(s')-\theta_m(s'))}\big(\mathcal{E}_n(s')-\mathcal{E}_m(s')\big)A_{nm}(s') \\
&\qquad\qquad \times|\mathcal{E}_n(0)\rangle\langle\mathcal{E}_m(0)|. \qquad \text{(B.14)}
\end{aligned}
$$

We can expand the T-dependent integral in Eq.(B.14) in powers of $1/T$ by successive integration by parts. In this case, we will only need terms up to order T^{-1}.

$$
\begin{aligned}
&\int_0^s ds'\;e^{iT(\theta_n(s')-\theta_m(s'))}\big(\mathcal{E}_n(s')-\mathcal{E}_m(s')\big)A_{nm}(s') = \\
&\quad\frac{1}{iT}A_{nm}(s')e^{iT(\theta_n(s')-\theta_m(s'))}\Big|_0^s - \frac{1}{iT}\int_0^s ds' e^{iT(\theta_n(s')-\theta_m(s'))}\frac{d}{ds'}A_{nm}(s') \\
&\qquad = \frac{i}{T}\Big(A_{nm}(0) - A_{nm}(s)e^{iT(\theta_n(s)-\theta_m(s))}\Big) + \mathrm{O}(T^{-2}), \qquad \text{(B.15)}
\end{aligned}
$$

where we used the fact that $\mathcal{E}_n(s) = \frac{d}{ds}\theta_n(s)$, because of Eq.(B.12). All higher Magnus expansion terms are of order T^{-2} and above.

Putting Eq.(B.15, B.14) together, the propagator in our $W(s)$ frame, $\tilde{\mathcal{U}}(s)$, is

$$\tilde{\mathcal{U}}(s) = \tilde{\mathcal{U}}_0(s) \exp\Big[-i \sum_{n=1}^{d} \gamma_n(s) |\mathcal{E}_n(0)\rangle\langle\mathcal{E}_n(0)| + \frac{i}{T} \sum_{n\neq m} \Big(A_{nm}(0) - A_{nm}(s) e^{iT(\theta_n(s)-\theta_m(s))} \Big) |\mathcal{E}_n(0)\rangle\langle\mathcal{E}_m(0)| + \mathrm{O}(T^{-2}) \Big]. \quad \text{(B.16)}$$

Now consider the case in which the T^{-1} term is much smaller than the T^0 term. One way of achieving this is by having $|A_{nm}(s)|/T \ll 1$ for all $s \in [0,1]$. In other words, by the evolution duration having a lower bound,

$$T \gg \max_{\substack{n,m\in\{1,..,d\} \\ s\in[0,1]}} \frac{|\langle\mathcal{E}_m(s)|\frac{d}{ds}H(s)|\mathcal{E}_n(s)\rangle|}{|\mathcal{E}_n(s) - \mathcal{E}_m(s)|^2}, \quad \text{(B.17)}$$

which is the adiabatic condition. Under this assumption, we can use Eq.(B.16, B.9) to get,

$$\begin{aligned} \tilde{\mathcal{U}}(s) &\simeq \sum_{n=1}^{d} e^{-iT\theta_n(s)} |\mathcal{E}_n(0)\rangle\langle\mathcal{E}_n(0)| \ \exp\Big[-i \sum_{m=1}^{d} \gamma_m(s) |\mathcal{E}_m(0)\rangle\langle\mathcal{E}_m(0)| \Big] \\ &= \sum_{n=1}^{d} e^{-iT\theta_n(s)} e^{-i\gamma_n(s)} |\mathcal{E}_n(0)\rangle\langle\mathcal{E}_n(0)|. \end{aligned} \quad \text{(B.18)}$$

Reverting back from the $W(s)$ frame using $\mathcal{U}(s) = W^\dagger(s)\tilde{\mathcal{U}}(s)$, and using the original time variable $t = Ts$, the propagator under the adiabatic condition reduces to

$$U(t) \simeq \sum_{n=1}^{d} e^{-i\int_0^t dt' E_n(t')} e^{i\int_0^t dt' i\langle E_n(t')|\frac{d}{dt'}|E_n(t')\rangle} |E_n(t)\rangle\langle E_n(0)|. \quad \text{(B.19)}$$

Acting this propagator on an initial eigenstate $|E_k(0)\rangle$ results in our original statement of the adiabatic approximation $U(t)|E_k(0)\rangle \simeq \exp(i\phi_k(t))|E_k(t)\rangle$, with the phase $\phi_k(t)$ satisfying Eq.(1.22).

Therefore, an energy eigenstate stays an eigenstate throughout the evolution if the adiabatic condition of Eq.(B.17) is satisfied; we have reached the adiabatic theorem. The adiabatic condition Eq.(B.17) can also be written in terms of the original time variable $t = Ts$, which leads to the adiabatic condition Eq.(1.20) given in the main text.

Appendix C

Wigner d-Matrix Elements

An explicit formula for Wigner d-matrix elements was derived by Schwinger [68] through connecting the angular momentum algebra with the algebra of two independent harmonic oscillators. The general expression is [18, 68]

$$d^{(I)}_{m'm}(\vartheta) = \sum_{k=k_1}^{k_2} (-1)^{k-m+m'} \frac{\sqrt{(I+m)!(I-m)!(I+m')!(I-m')!}}{(I+m-k)!(I-k-m')!(k-m+m')!k!} \times \left(\cos\frac{\vartheta}{2}\right)^{2I-2k+m-m'} \left(\sin\frac{\vartheta}{2}\right)^{2k-m+m'}, \quad \text{(C.1)}$$

with the sum going through all integer values of k that result in a non-negative argument in the factorial terms, in other words

$$k_1 = \mathrm{Min}\{0, m-m'\}, \qquad k_2 = \mathrm{Max}\{0, I+m, I-m'\}. \quad \text{(C.2)}$$

The Wigner d-matrix elements for the first few spin numbers are listed below for convenience.

- $I = 1/2$:

$$d^{\frac{1}{2}}_{\frac{1}{2},\frac{1}{2}}(\vartheta) = \cos\frac{\vartheta}{2} \qquad d^{\frac{1}{2}}_{\frac{1}{2},-\frac{1}{2}}(\vartheta) = -\sin\frac{\vartheta}{2} \quad \text{(C.3)}$$

- $I = 1$:

$$d^1_{1,1}(\vartheta) = \frac{1}{2}(1+\cos\vartheta) \qquad d^1_{1,0}(\vartheta) = -\frac{1}{\sqrt{2}}\sin\vartheta$$
$$d^1_{1,-1}(\vartheta) = \frac{1}{2}(1-\cos\vartheta) \qquad d^1_{0,0}(\vartheta) = \cos\vartheta \quad \text{(C.4)}$$

- $I = 3/2$:

$$
\begin{aligned}
d^{\frac{3}{2}}_{\frac{3}{2},\frac{3}{2}}(\vartheta) &= \frac{1}{2}(1+\cos\vartheta)\cos\frac{\vartheta}{2} \qquad & d^{\frac{3}{2}}_{\frac{3}{2},\frac{1}{2}}(\vartheta) &= -\frac{\sqrt{3}}{2}(1+\cos\vartheta)\sin\frac{\vartheta}{2} \\
d^{\frac{3}{2}}_{\frac{3}{2},-\frac{1}{2}}(\vartheta) &= \frac{\sqrt{3}}{2}(1-\cos\vartheta)\cos\frac{\vartheta}{2} \qquad & d^{\frac{3}{2}}_{\frac{3}{2},-\frac{3}{2}}(\vartheta) &= -\frac{1}{2}(1-\cos\vartheta)\sin\frac{\vartheta}{2} \\
d^{\frac{3}{2}}_{\frac{1}{2},\frac{1}{2}}(\vartheta) &= \frac{1}{2}(3\cos\vartheta-1)\cos\frac{\vartheta}{2} \qquad & d^{\frac{3}{2}}_{\frac{1}{2},-\frac{1}{2}}(\vartheta) &= -\frac{1}{2}(3\cos\vartheta+1)\sin\frac{\vartheta}{2}
\end{aligned}
\tag{C.5}
$$

The matrix elements not listed here can be calculated by using the fact that $d^{(I)}_{m'm}(\vartheta) = (-1)^{m-m'} d^{(I)}_{mm'}(\vartheta)$ [18].

Appendix D

The Adiabatic Condition for the FM Frame Hamiltonian

Here we examine the adiabatic condition for the FM frame magnetic resonance Hamiltonian $H(t) = -\mathbf{b}(t) \cdot \mathbf{I}$. This requires the evaluation of the left-hand side of Eq.(1.20), which is

$$|A_{nm}(t)| = \frac{|\langle E_m(t)|\frac{d}{dt}H(t)|E_n(t)\rangle|}{|E_n(t) - E_m(t)|^2} \qquad m \neq n. \tag{D.1}$$

In order to calculate the numerator $|\langle E_m(t)|\frac{d}{dt}H(t)|E_n(t)\rangle| = |\langle E_m(t)|\dot{\mathbf{b}}(t) \cdot \mathbf{I}|E_n(t)\rangle|$, note that for any vector $\mathbf{v}$, the expression $|\langle m|\mathbf{v} \cdot \mathbf{I}|n\rangle|$ can only be non-zero if $m = n \pm 1$ or $m = n$, because $\mathbf{v} \cdot \mathbf{I}$ is a linear combination of the ladder operators I_+, I_- and I_z. Since Eq.(D.1) requires the $m \neq n$ case, the relevant terms are simply $|\langle m \pm 1|\mathbf{v} \cdot \mathbf{I}|m\rangle|$. These can be explicitly calculated using ladder operators, resulting in

$$\begin{aligned} |\langle m \pm 1|\mathbf{v} \cdot \mathbf{I}|m\rangle| &= \frac{1}{2}\sqrt{I(I+1) - m(m \pm 1)}\sqrt{v_x^2 + v_y^2} \\ &= \frac{1}{2}\sqrt{I(I+1) - m(m \pm 1)}\ \big|(\mathbf{v} \cdot \hat{\mathbf{z}})\hat{\mathbf{z}} - \mathbf{v}\big|, \end{aligned} \tag{D.2}$$

i.e. $|\langle m \pm 1|\mathbf{v} \cdot \mathbf{I}|m\rangle|$ is proportional to the component of $\mathbf{v}$ that is transverse to the quantization axis. This can be used to evaluate the numerator of Eq.(D.1) by picking the quantization axis to be along the effective field, and writing

$$|\langle E_{m\pm1}(t)|\dot{\mathbf{b}}(t)|E_m(t)\rangle| = \frac{1}{2}\sqrt{I(I+1) - m(m \pm 1)}\ \Big|\big(\dot{\mathbf{b}}(t) \cdot \hat{\mathbf{b}}(t)\big)\hat{\mathbf{b}}(t) - \dot{\mathbf{b}}(t)\Big|, \tag{D.3}$$

with $\hat{\mathbf{b}}(t) \equiv \mathbf{b}(t)/|\mathbf{b}(t)|$ being the unit vector along the quantization axis, and $\big(\dot{\mathbf{b}}(t) \cdot \hat{\mathbf{b}}(t)\big)\hat{\mathbf{b}}(t) - \dot{\mathbf{b}}(t)$ being the component of $\dot{\mathbf{b}}(t)$ transverse to it. Eq.(D.3) can be further simplified by observing that

$$\begin{aligned}\frac{d}{dt}\hat{\mathbf{b}}(t) &= \frac{d}{dt}\big(\frac{\mathbf{b}(t)}{|\mathbf{b}(t)|}\big) \\ &= \frac{1}{|\mathbf{b}(t)|^2}\Big[|\mathbf{b}(t)|\dot{\mathbf{b}}(t) - \mathbf{b}(t)\frac{d}{dt}|\mathbf{b}(t)|\Big],\end{aligned} \tag{D.4}$$

which together with $\frac{d}{dt}|\mathbf{b}(t)| = \frac{d}{dt}\sqrt{\mathbf{b}(t)\cdot\mathbf{b}(t)} = \dot{\mathbf{b}}(t)\cdot\hat{\mathbf{b}}(t)$ gives

$$\dot{\mathbf{b}}(t) - \big(\dot{\mathbf{b}}(t)\cdot\hat{\mathbf{b}}(t)\big)\hat{\mathbf{b}}(t) = |\mathbf{b}(t)|\frac{d}{dt}\hat{\mathbf{b}}(t). \tag{D.5}$$

Furthermore, the quantity $\frac{d}{dt}\hat{\mathbf{b}}(t)$ can be related to the instantaneous angular velocity associated with the motion of the effective field. By comparing the effective field at two instances $t,\ t+\delta t$. For sufficiently small δt, the difference between $\hat{\mathbf{b}}(t+\delta t)$ and $\hat{\mathbf{b}}(t)$ can be calculated from Fig.(D.1),

$$|\frac{d}{dt}\hat{\mathbf{b}}(t)|\delta t = |\hat{\mathbf{b}}(t+\delta t) - \hat{\mathbf{b}}(t)| = \delta\beta(t), \tag{D.6}$$

where $\delta\beta(t)$ is the angle between $\hat{\mathbf{b}}(t+\delta t)$ and $\hat{\mathbf{b}}(t)$. Therefore, the angular velocity $\Omega(t) = \frac{d}{dt}\beta(t)$ is

$$\Omega(t) = |\frac{d}{dt}\hat{\mathbf{b}}(t)|. \tag{D.7}$$

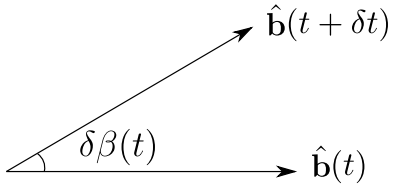

Figure D.1: Calculating the angular velocity of the effective field.

Combining Eq.(D.1, D.3, D.5, D.1) with the fact that $|E_{m\pm1}(t) - E_m(t)| = |\mathbf{b}(t)|$ gives

$$|A_{m,m\pm1}(t)| = \frac{1}{2}\sqrt{I(I+1) - m(m\pm1)}\frac{\Omega(t)}{|\mathbf{b}(t)|}, \tag{D.8}$$

with the adiabatic condition $\mathrm{Max}_{t,m,n}|A_{nm}(t)| \ll 1$ simplifying to

$$\frac{1}{2}\underset{m\in\{-I,\ldots I\}}{\mathrm{Max}}\sqrt{I(I+1)-m(m\pm 1)}\ \underset{t\in[0,T]}{\mathrm{Max}}\frac{\Omega(t)}{|\mathbf{b}(t)|}\ll 1, \tag{D.9}$$

and since the maximum of $\sqrt{I(I+1)-m(m\pm 1)}$ occurs for $m=\mp 1/2$, with the value $\sqrt{I(I+1)+1/4}=I+1/2$, the final adiabatic condition for the FM Hamiltonian is

$$\frac{2I+1}{4}\ \underset{t\in[0,T]}{\mathrm{Max}}\ \frac{\Omega(t)}{|\mathbf{b}(t)|}\ll 1, \tag{D.10}$$

as desired.

Appendix E

Eigenprojection operators for two-level systems

In this appendix, we derive Eq.(2.10) for the projection operators $P_\pm$ onto the eigenspaces of a general Hamiltonian $H = -\big(b_0\mathbb{1} + \mathbf{b}\cdot\boldsymbol{\sigma}\big)/2$ acting on a two-dimensional Hilbert space. This is done by using Eq.(2.5) for the eigenvectors $|E_\pm\rangle$ in terms of the spherical coordinate representation of $\mathbf{b}$,

$$\mathbf{b} = (\cos\psi\sin\vartheta, \sin\psi\sin\vartheta, \cos\vartheta), \tag{E.1}$$

and calculating $P_\pm = |E_\pm\rangle\langle E_\pm|$. For example, P_+ is

$$\begin{aligned} P_+ &= \big(\cos\frac{\vartheta}{2}\,|\uparrow\rangle + e^{i\psi}\sin\frac{\vartheta}{2}\,|\downarrow\rangle\,\big)\big(\cos\frac{\vartheta}{2}\,\langle\uparrow| + e^{-i\psi}\sin\frac{\vartheta}{2}\,\langle\downarrow|\,\big) \\ &= \frac{1+\cos\vartheta}{2}\,|\uparrow\rangle\langle\uparrow| + \frac{1-\cos\vartheta}{2}\,|\downarrow\rangle\langle\downarrow| + \frac{\sin\vartheta}{2}\big(e^{i\psi}\,|\downarrow\rangle\langle\uparrow| + e^{i\psi}\,|\uparrow\rangle\langle\downarrow|\,\big) \\ &= \frac{1}{2}\Big(\mathbb{1} + \sin\vartheta\cos\psi\ \sigma_x + \sin\vartheta\sin\psi\ \sigma_y + \cos\vartheta\ \sigma_z\Big), \end{aligned} \tag{E.2}$$

where we used the double angle formulas, and the fact that $\sigma_z = |\uparrow\rangle\langle\uparrow| - |\downarrow\rangle\langle\downarrow|$, $\sigma_x = |\uparrow\rangle\langle\downarrow| + |\downarrow\rangle\langle\uparrow|$ and $\sigma_y = i\,|\uparrow\rangle\langle\downarrow| - i\,|\downarrow\rangle\langle\uparrow|$.

Using Eq.(E.1) and repeating this calculation for the other eigenstate gives

$$P_\pm = \frac{1}{2}\big(\mathbb{1} \pm \frac{\mathbf{b}}{|\mathbf{b}|}\cdot\boldsymbol{\sigma}\big). \tag{E.3}$$

as desired.

Appendix F

Geometric Interpretation of the Adiabaticity Metric

This appendix derives a formula for the adiabaticity metric of Eq.(2.7), in terms of the angle between the effective field and the Bloch sphere representation of the instantaneous state, or in other words, the magnetization.

First we derive a convenient interpretation for the inner product of states in a two-dimensional Hilbert space in terms of the angle between their representations on the Bloch sphere. This is then used on the adiabaticity metric to show the desired result.

F.1 Geometry of Inner Products on the Bloch Sphere

Here we show that for any two states $|\psi\rangle, |\psi'\rangle$ in a two-dimensional Hilbert space $\mathcal{H}$, the (squared) magnitude of the inner product $|\langle\psi|\psi'\rangle|^2$ is equal to

$$|\langle\psi|\psi'\rangle|^2 = \frac{1}{2}(1+\cos\alpha), \tag{F.1}$$

with α being the angle between the Bloch sphere representation of the two states, as depicted in Fig.(F.1). To show this, we utilize the Bloch sphere representation [69]

$$\begin{cases} |\psi\rangle = \cos\dfrac{\theta}{2}|\uparrow\rangle + e^{i\varphi}\sin\dfrac{\theta}{2}|\downarrow\rangle \\ |\psi'\rangle = \cos\dfrac{\theta'}{2}|\uparrow\rangle + e^{i\varphi'}\sin\dfrac{\theta'}{2}|\downarrow\rangle \end{cases}, \tag{F.2}$$

with (θ, φ) and (θ', φ') being the polar and azimuthal angles of the two states. Direct calculation of the inner product using Eq.(F.2) gives

$$\begin{aligned}
|\langle\psi|\psi'\rangle|^2 &= \Big| \cos\frac{\theta}{2}\cos\frac{\theta'}{2} + e^{i(\varphi-\varphi')}\sin\frac{\theta}{2}\sin\frac{\theta'}{2}\Big|^2 \\
&= \cos^2\frac{\theta}{2}\cos^2\frac{\theta'}{2} + \sin^2\frac{\theta}{2}\sin^2\frac{\theta'}{2} + 2\sin\frac{\theta}{2}\sin\frac{\theta'}{2}\cos\frac{\theta}{2}\cos\frac{\theta'}{2}\cos(\varphi-\varphi') \\
&= \frac{1+\cos\theta}{2}\frac{1+\cos\theta'}{2} + \frac{1-\cos\theta}{2}\frac{1-\cos\theta}{2} + \frac{1}{2}\sin\theta\sin\theta'\cos(\varphi-\varphi') \\
&= \frac{1}{2}\big(1 + \cos\theta\cos\theta' + \sin\theta\sin\theta'\cos(\varphi-\varphi')\big). \qquad \text{(F.3)}
\end{aligned}$$

On the other hand, $\cos\alpha = \cos\theta\cos\theta' + \sin\theta\sin\theta'\cos(\varphi-\varphi')$ because

$$\begin{aligned}
\cos\alpha &= (\cos\varphi\sin\theta, \sin\varphi\sin\theta, \cos\theta)\cdot(\cos\varphi'\sin\theta', \sin\varphi'\sin\theta', \cos\theta') \\
&= \sin\theta\sin\theta'\big(\cos\varphi\cos\varphi' + \sin\varphi\sin\varphi'\big) + \cos\theta\cos\theta' \\
&= \cos\theta\cos\theta' + \sin\theta\sin\theta'\cos(\varphi-\varphi'). \qquad \text{(F.4)}
\end{aligned}$$

Combining Eq.(F.3, F.4) results in Eq.(F.1), as desired.

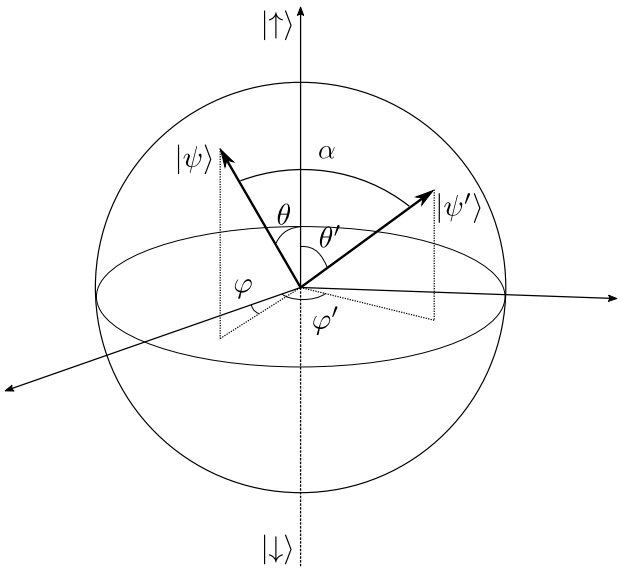

Figure F.1: Geometric interpretation of the Hilbert-space inner product on the Bloch sphere

F.2 Interpretation of the Adiabaticity Metric

Utilizing the above lemma, the inner product $|\langle E_\pm(\mathbf{x},t)|U(\mathbf{x},t)|\psi_0\rangle|^2$ used in the adiabaticity metric of Eq.(2.7) is

$$\begin{aligned}|\langle E_\pm(\mathbf{x},t)|U(\mathbf{x},t)|\psi_0\rangle|^2 &= |\langle E_\pm(\mathbf{x},t)|\psi(\mathbf{x},t)\rangle\rangle|^2 \\ &= \frac{1}{2}\big(1+\cos\alpha(\mathbf{x},t)\big),\end{aligned} \tag{F.5}$$

with $\alpha(\mathbf{x},t)$ being the angle between the effective field and $|\psi(\mathbf{x},t)\rangle$ on the Bloch sphere. Combining Eq.(F.5,2.7) results in

$$\Phi_{\text{ad}}(\mathbf{x}) = \frac{1}{2T}\int_0^T dt\big(1+\cos\alpha(\mathbf{x},t)\big). \tag{F.6}$$

In other words, the adiabaticity metric is related to the normalized time-average of the cosine of the instantaneous angle between the effective field and the magnetization.

Appendix G

Inverse of Block Triangular Matrices

Analytical expressions for the inverse of block triangular matrices such as Eq.(2.22) are crucial for the computational efficiency of the target function gradient calculations. For this reason, we look for the inverse of the general block-triangular matrix

$$\mathcal{A} = \begin{bmatrix} A_{11} & A_{12} & \dots & A_{1,n-1} & A_{1n} \\ 0 & A_{22} & \dots & A_{2,n-1} & A_{2n} \\ 0 & 0 & \dots & A_{3,n-1} & A_{3n} \\ \vdots & \vdots & \ddots & \vdots & \vdots \\ 0 & 0 & \dots & 0 & A_{nn} \end{bmatrix}, \tag{G.1}$$

with the individual blocks A_{ij} all being invertible square matrices of the same dimension. To calculate the inverse, we use the ansatz

$$\mathcal{A}^{-1} = \begin{bmatrix} B_{11} & B_{12} & \dots & B_{1,n-1} & B_{1n} \\ 0 & B_{22} & \dots & B_{2,n-1} & B_{2n} \\ 0 & 0 & \dots & B_{3,n-1} & B_{3n} \\ \vdots & \vdots & \ddots & \vdots & \vdots \\ 0 & 0 & \dots & 0 & B_{nn} \end{bmatrix}. \tag{G.2}$$

Setting $\mathcal{A}^{-1}\mathcal{A} = \mathbb{1}$, explicit multiplication of the two matrices results in

$$\sum_{k=0}^{j-i} B_{i,i+k} A_{i+k,j} = \delta_{ij} \mathbb{1}. \tag{G.3}$$

The above equation can be used to find analytical expressions for the various blocks B_{ij} recursively, starting from $j = i$, which gives $B_{ii}A_{ii} = \mathbb{1}$, meaning that

$$B_{ii} = A_{ii}^{-1}. \tag{G.4}$$

With this in mind, for $j = i + 1$, we have $B_{ii}A_{i,i+1} + B_{i,i+1}A_{i+1,i+1} = 0$, which together with Eq.(G.3), gives

$$B_{i,i+1} = -A_{ii}^{-1}\ A_{i,i+1}\ A_{i+1,i+1}^{-1}. \tag{G.5}$$

This procedure can be continued until all blocks of $\mathcal{A}^{-1}$ are found. In most cases in this work, such as Eq.(2.22), the individual blocks are unitary matrices, facilitating the calculation of the inverse since $A_{ij}^{-1} = A_{ij}^{\dagger}$.

In cases where matrices were combined with direct sums, such as Eq.(2.41), inverses can be calculated by realizing that $(A \oplus B)^{-1} = A^{-1} \oplus B^{-1}$, this is simply because

$$\begin{aligned}(A \oplus B)(A^{-1} \oplus B^{-1}) &= \begin{bmatrix} A & 0 \\ 0 & B \end{bmatrix} \begin{bmatrix} A^{-1} & 0 \\ 0 & B^{-1} \end{bmatrix} \\ &= \begin{bmatrix} AA^{-1} & 0 \\ 0 & BB^{-1} \end{bmatrix} \\ &= \mathbb{1}, \end{aligned} \tag{G.6}$$

i.e. the inverse of a direct sum is the direct sum of the inverses.

Appendix H

Normalization of the Perturbation Metric

In this appendix, we derive Eq.(2.30), used for the normalization of the perturbation metric in Section 2.6.2. To this end, we need to calculate an upper bound for the general expression

$$\left\|\mathcal{D}_U(A;T)|\psi\rangle\right\|^2, \tag{H.1}$$

for an anti-Hermitian operator-valued function $A : [0,T] \to \mathcal{L}(\mathcal{H})$. This is done by expanding it using the definition of the Dyson term, Eq.(1.10), which gives

$$\begin{aligned}
\left\|\mathcal{D}_U(A;T)|\psi\rangle\right\|^2 &= \int_0^T dt_1 \int_0^T dt_2 \langle\psi|\ U^\dagger(t_1)A^\dagger(t_1)U(t_1)\ U^\dagger(t_2)A(t_2)U(t_2)\ |\psi\rangle \\
&= \Big| \int_0^T dt_1 \int_0^T dt_2 \Big\langle U^\dagger(t_1)A(t_1)U(t_1)|\psi\rangle\ ,\ U^\dagger(t_2)A(t_2)U(t_2)|\psi\rangle \Big\rangle \Big| \\
&\leq \int_0^T dt_1 \int_0^T dt_2 \Big| \Big\langle U^\dagger(t_1)A(t_1)U(t_1)|\psi\rangle\ ,\ U^\dagger(t_2)A(t_2)U(t_2)|\psi\rangle \Big\rangle \Big| \qquad \text{(H.2)} \\
&\leq \int_0^T dt_1 \int_0^T dt_2 \Big\| U^\dagger(t_1)A(t_1)U(t_1)|\psi\rangle \Big\| \times \Big\| U^\dagger(t_2)A(t_2)U(t_2)|\psi\rangle \Big\| \qquad \text{(H.3)} \\
&= \left(\int_0^T dt \Big\| U^\dagger(t)A(t)U(t)|\psi\rangle \Big\| \right)^2, \qquad \text{(H.4)}
\end{aligned}$$

where we used the triangle and Cauchy-Schwarz inequalities in Eq.(H.2, H.3), respectively. On the other hand, the norm inside the integral satisfies

$$\begin{aligned}\big\|U^\dagger(t)A(t)U(t)|\psi\rangle\big\| &\leq \big\|U^\dagger(t)A(t)U(t)\big\|_{\text{op}} \times \underbrace{\|\psi\|}_{1} \\ &= \big\|A(t)\big\|_{\text{op}},\end{aligned} \tag{H.5}$$

where

$$\|A(t)\|_{\text{op}} \equiv \underset{|v\rangle\in\mathcal{H}}{\text{Max}} \frac{\big\|A(t)|v\rangle\big\|}{\|v\|}, \tag{H.6}$$

is the operator norm, which is equal to the largest singular value of $A(t)$ [58]. Since $A(t)$ is anti-Hermitian, and hence normal, the largest singular value is simply the largest magnitude between its eigenvalues $|\lambda_{\text{max}}\big(A(t)\big)|$. With that in mind, combining Eq.(H.5 ,H.4) results in our final upper bound

$$\big\|\mathcal{D}_U(A;T)|\psi\rangle\big\|^2 \leq \Big(\int_0^T dt\ \big|\lambda_{\text{max}}\big(A(t)\big)\big|\Big)^2, \tag{H.7}$$

as desired.

Appendix I

Simulating White Gaussian Noise with Discrete Samples

Here we show that a discrete IID zero-mean random process $\{X_n\}_{n=1}^{\lfloor T/\Delta t \rfloor}$ with variance $\sigma^2 = A^2/\Delta t$ approaches a continuous-time process with constant spectral density A^2 in the continuum limit $\Delta t \to 0$. To this end, we define the continuous-time process

$$\tilde{X}(t;\Delta t) \equiv \sum_{n=1}^{\lfloor T/\Delta t \rfloor} X_n \; p\Big(\frac{t-(n-1)\Delta t}{\Delta t}\Big), \tag{I.1}$$

where

$$p(x) = \begin{cases} 1 & x \in [0,1] \\ 0 & x \in \mathbb{R} \setminus [0,1] \end{cases}, \tag{I.2}$$

is a function that interpolates the samples X_n with a piecewise constant waveform. To determine the spectral density of the continuum limit $X(t) \equiv \lim_{\Delta t \to 0} \tilde{X}(t;\Delta t)$, we use the fact that the power spectral density of a process of the form $\sum_n X_n g(t - n\Delta t)$ is equal to $\sigma^2 |G(f)|^2/\Delta t$, with $G(f) \equiv \int_{-\infty}^{\infty} dt \; g(t) e^{-i2\pi f t}$ being the Fourier transform of g [62]. This lemma, combined with Eq.(I.1) and the scaling property of the Fourier transform, results in the spectral density

$$\begin{aligned} S_{\tilde{X}}(f;\Delta t) &= \frac{\sigma^2}{\Delta t} \times \Delta t^2 |P(f\Delta t)|^2 \\ &= \sigma^2 \Delta t |P(f\Delta t)|^2. \end{aligned} \tag{I.3}$$

Substituting $\sigma^2 = A^2/\Delta t$, taking the $\Delta t \to 0$ limit, and realizing that by Eq.(I.2), $P(0) = \int_{-\infty}^{\infty} dx\ p(x) = 1$, gives the final result

$$S_X(f) \equiv \lim_{\Delta t \to 0} S_{\tilde{X}}(f; \Delta t) = A^2, \tag{I.4}$$

as desired.